

ELECTROLUMINESCENT AND PHOTOPHYSICAL PROPERTIES OF NEAR-
INFRARED LUMINESCENT LANTHANIDE (III) MONOPORPHYRINATE
COMPLEXES AND PENDANT POLYMERS

By

GARRY BRIAN CUNNINGHAM

A DISSERTATION PRESENTED TO THE GRADUATE SCHOOL
OF THE UNIVERSITY OF FLORIDA IN PARTIAL FULFILLMENT
OF THE REQUIREMENTS FOR THE DEGREE OF
DOCTOR OF PHILOSOPHY

UNIVERSITY OF FLORIDA

2005

Copyright 2005

by

Garry Brian Cunningham

I dedicate this to my father.

ACKNOWLEDGMENTS

There are so many people that I would like to acknowledge. First and foremost is my advisor, Professor Kirk Schanze. He has been a great mentor. I would also like to acknowledge all of the people that have helped me on my projects along the way including Professor John Reynolds, Professor Paul Holloway, Dr. Tim Foley, Dr. Mauricio Pinto, Dr. Alison Knefely, Dr. Avni Argun, Dr. T.S. Kang, Dr. Benjamin Harrison, Nisha Ananthakrishnan, Dr. Fengqi Guo, Dr. Jeremiah Mwuara, and Dr. James Boncella. I would like to thank former and current members of the Schanze group. I would like to thank my friends who made living in Gainesville bearable. Lastly, I would like to thank my committee.

TABLE OF CONTENTS

	<u>page</u>
ACKNOWLEDGMENTS	iv
LIST OF TABLES	vii
LIST OF FIGURES	viii
ABSTRACT	xiii
CHAPTER	
1 INTRODUCTION	1
Electrodynamics	1
Absorption of Light	1
Emission of Light	3
Nonradiative Decay	8
Energy Transfer	9
Lanthanides	12
Porphyrins	17
Photophysics	17
Redox Properties	20
Synthesis	22
Light Emitting Diodes	25
OLED and PLED Structure	29
Carrier Transport	30
Device Efficiency	33
Device Failure Mechanisms	34
Literature Review	35
Organic Systems	36
Inorganic Nanoparticles	37
Organo-Lanthanide and Organo-Transition Metal Complexes	39
2 SUBSTITUTED PORPHYRIN COMPLEXES	42
Solution Photophysics	44
Absorption	44
Emission	45
Light Emitting Devices	54

Electrochemistry	64
Conclusions.....	69
Experimental.....	70
Photophysical Measurements	70
Device Fabrication.....	71
ITO Etching.....	71
Cleaning ITO.....	72
Spin Coating.....	72
Metal Electrode Deposition.....	73
Electroluminescent Device Measurements.....	73
Electrochemistry.....	74
3 PORPHYRIN PENDANT POLYACETYLENES.....	75
Introduction.....	75
Monomer Synthesis and Polymerization.....	76
Photophysics	84
Absorption	84
Emission	88
Thermally Induced Isomerization.....	90
Light Emitting Devices.....	92
Discussion.....	99
Conclusions.....	100
Experimental.....	101
Monomer Synthesis.....	101
Polymerization.....	104
Thermogravimetric Analysis	105
Photophysical Measurements.....	105
Device Fabrication and Measurement.....	106
4 FUTURE DIRECTIONS.....	107
Non-Radiative Decay.....	107
Carrier Transport	109
Porphyrin Containing Polymers	110
Conclusions.....	112
APPENDIX ELECTRONIC PROPERTIES	115
The Free-Ion Problem.....	115
The Crystal Field Problem.....	119
Coupling of the Electronic and Lattice States	124
Einstein Model.....	128
LIST OF REFERENCES.....	132
BIOGRAPHICAL SKETCH	148

LIST OF TABLES

<u>Table</u>	<u>page</u>
2-1 Photophysical properties of Yb porphyrin complexes measured in CH ₂ Cl ₂	45
2-2 Solvent effects on the near-infrared quantum yields of Yb porphyrin complexes...	52
2-3 Electrochemical windows of solvents.....	65
2-4 Electrochemical properties of substituted porphyrins.....	70
3-1 Polymerization details.....	83
3.2 Photophysical data.....	86
3-3 Electroluminescence data.....	97
4-1 Vibrational frequencies of common bonds in organic molecules.....	109
A-1 Real orbitals created from linear combinations of orbitals labeled by their magnetic quantum number.....	123
A-2 Position and symmetry of <i>f</i> -orbitals in an octahedral crystal field.....	123

LIST OF FIGURES

<u>Figure</u>	<u>page</u>
1-1 Schematic of absorption shown as a function of thickness, concentration, and molar absorptivity.	2
1-2 Configuration coordinate model.....	3
1-3 Jablonski diagram showing the fundamental processes of absorption, internal conversion, fluorescence, intersystem crossing, and phosphorescence.	4
1-4 Configuration coordinate diagram showing the zero-phonon line and illustrating the process known as the Stoke's shift.....	5
1-5 Configuration coordinate model showing the process of phosphorescence.....	6
1-6 Interaction of atom nuclear charge induced angular momentum interacting with electron's spin angular momentum, resulting in spin-orbit coupling.....	7
1-7 Typical nonradiative processes through (a) crossover with a ground state, (b) multiphonon emission, and (c) crossover with an excited state.	9
1-8 Schematic showing the overlap of donor fluorescence with the acceptor absorption, fundamental for Forster energy transfer.	11
1.9 Graphical description of <i>f</i> orbitals.	14
1-10 Energy level diagrams for selected rare earth ions in LnCl ₃	15
1-11 Absorption spectra of selected lanthanide ions, showing sharp absorption with low molar absorptivity.	16
1-12 Jablonski energy diagram showing energy transfer from organic ligand to lanthanide metal, in this case Yb ³⁺	16
1-13 Structure of porphyrin macrocycle, showing possible areas of substitution.	17
1-14 Molecular orbitals for the porphyrin macrocycle for the highest occupied molecular orbital and lowest unoccupied molecular orbital calculated using the Gouterman method.	20
1-15 Absorption spectrum of tetraphenylporphyrin.	21

1-16	Fluorescence spectrum of tetraphenylporphyrin.	22
1-17	Schematic of Rothmund synthesis.	22
1-18	Schematic of Lindsey synthesis of porphyrins.	23
1-19	Schematic of 2 + 2 condensation method for synthesis A ₂ B ₂ type porphyrins.	24
1-20	Schematic of lanthanide metallation of porphyrins using the Foley method.	24
1-21	Axial substitution of lanthanide metalloporphyrins using salt metathesis.	25
1-22	Structure of aluminum <i>tris</i> -quinolate.	26
1-23	Photoluminescence and electroluminescence spectra of Alq ₃	26
1-24	Structure of Ir(ppy) ₃	29
1-25	Schematic of light emitting diode, showing each individual layer.	29
1-26	Structures of typical hole transport materials.	30
1-27	Structure of Lanthanide <i>tris</i> -quinolate.	40
1-28	Structure of Lanthanide tris-DBM bathophenthroline complex.	41
2-1	Yb porphyrin complexes used in study.	43
2-2	X-ray crystal structure of Yb(TPP)Q showing coordination of a molecule of THF.	44
2-3	Absorption spectra for a)Yb(TPP)Q, b) Yb(TMPP)TP, c) Yb(TPyP)L(OEt) ₃ , d) Yb(TPP_OEH)TP in CH ₂ Cl ₂ as a function of molar absorptivity.	48
2-4	Visible emission spectra for substituted Yb ³⁺ complexes in CH ₂ Cl ₂ at room temperature.	49
2-5	Excitation spectra of (a) Yb(TPP)Q, (b) Yb(TMPP)TP, and (c) Yb(TPyP)L(OEt) ₃	50
2-6	Near-infrared emission spectra for substituted Yb ³⁺ porphyrin complexes in CH ₂ Cl ₂ at room temperature	51
2-7	Near-infrared emission spectra for substituted porphyrin complexes in 2Me-THF	52
2-8	Visible electroluminescence of Yb(TPP)Q, Yb(TMPP)TP, Yb(TPyP)L(OEt) ₃ , and Yb(TPP_OEH)TP as a function of increasing voltage, starting at 6V.	56

2-9	NIR Electroluminescence of Yb(TPP)Q, Yb(TMPP)TP, Yb(TPyP)L(OEt) ₃ , and Yb(TPP_OEH)TP as a function of increasing voltage, starting at 6V.....	57
2-10	Current density – Voltage (j-V) plot of Yb porphyrin devices as a function of loading wt% in PS.....	58
2-11	Near-Infrared external electroluminescent quantum efficiency for Yb(TPP)Q, Yb(TMPP)TP, Yb(TPyP)L(OEt) ₃ , and Yb(TPP_OEH)TP as a function of loading in PS.....	60
2-12	Charge hopping model showing transport of charges on porphyrin molecules.....	61
2-13	Current density-Voltage and NIR irradiance-voltage plots of Yb(TPP)TP as a function of Alq ₃ loading: (●) 0 wt %, (■) 33 wt%, and (▲) 66 wt %.....	62
2-14	NIR External quantum efficiency of Yb(TPP)TP as a function of Alq ₃ loading: (●) 0 wt %, (■) 33 wt%, and (▲) 66 wt %.....	63
2-15	Current density-voltage and NIR irradiance-voltage plots of Yb(TMPP)TP as a function of Alq ₃ loading: (●) 0 wt %, (■) 33 wt%, and (▲) 66 wt %.....	63
2-16	NIR external quantum efficiency of Yb(TMPP)TP as a function of Alq ₃ loading: (●) 0 wt %, (■) 33 wt%, and (▲) 66 wt %.....	64
2-17	Redox properties of free-base tetraphenylporphyrin with respect to the saturated calomel electrode.....	65
2-18	Reduction and oxidation waves for free-base tetraphenylporphyrin.....	66
2-19	Reduction and oxidation waves for Yb(TPP)TP.....	67
2-20	Reduction and oxidation potentials for Yb(TPP)Q.....	67
2-21	Reduction and oxidation waves for Yb(TMPP)TP.....	68
2-22	Reduction and oxidation waves for Yb(TPP)L(OEt) ₃	68
2-23	Reduction and oxidation waves for Yb(TPyP)L(OEt) ₃	69
2-24	Cartoon showing ITO substrate placed at top of beaker containing solution of aqua regia allowing vapors to etch surface.....	72
3-1	Synthesis of Zn(II)-5-(4-Ethynylphenyl)-10,15,20-triphenylporphyrin.....	77
3-2	Synthesis of 2-(4-methylphenyl)-5-(4-ethynylphenyl)-1,3,4-oxadiazole.....	78
3-3	Structure of (Bicyclo[2.2.1]hepta-2,5-diene)chlororhodium(I) dimer.....	79
3-4	Representative scheme of insertion polymerization mechanism.....	81

3-5	Polyacetylene isomer structures	81
3-6	Structure of ZnETPP homopolymer and copolymers.	82
3-7	NMR spectra of poly(ZnETPP) _{0.5} -co-(PE) _{0.5}	83
3-8	TGA traces of polymers of ETPP measured in air.	84
3-9	Absorption spectrum of (a) poly(ZnETPP) (—), (b) poly(ZnETPP) _{0.14} -co-(PE) _{0.86} (----), poly(ZnETPP) _{0.5} -co-(PE) _{0.5} (---), (c) poly(ZnETPP) _{0.5} -co-(PEOXAD) _{0.5} (—•—), and (d) poly(ZnETPP) _{0.5} -co-(3,5CF ₃ PE) _{0.5} (—••—)	87
3-10	Absorption and fluorescence spectrum of PEOXAD monomer.	88
3-11	a)Emission ($\lambda_{ex} = 420$ nm) of poly(ZnETPP) in solution (—), film (•••), (b) poly(ZnETPP) _{0.14} -co-(PE) _{0.86} in solution (—), film (•••) (----), poly(ZnETPP) _{0.5} -co-(PE) _{0.5} in solution (---), film (—) , (c) poly(ZnETPP) _{0.5} -co-(PEOXAD) _{0.5} in solution (—), and (d) poly(ZnETPP) _{0.5} -co-(3,5CF ₃ PE) _{0.5} in solution (—).	91
3-12	Emission of poly(ZnETPP) in film as a function of annealing time at 150° C in vacuum.	92
3-13	Current density vs. voltage and irradiance vs. voltage for a) poly(ZnETPP) b) poly(ZnETPP) _{0.5} -co-(PE) _{0.5} , c) poly(ZnETPP) _{0.5} -co-(PEOXAD) _{0.5} d) poly(ZnETPP) _{0.5} -co-(3,5CF ₃ PE) _{0.5} as a function of wt% of polystyrene.....	96
3-14	Electroluminescence emission of spectrum of poly(ZnETPP) (—), (b) poly(ZnETPP) _{0.14} -co-(PE) _{0.86} (---), poly(ZnETPP) _{0.5} -co-(PE) _{0.5} (---), (c) poly(ZnETPP) _{0.5} -co-(PEOXAD) _{0.5} (•••), and (d) poly(ZnETPP) _{0.5} -co-(3,5CF ₃ PE) _{0.5} (—••—)	97
3-15	TEM image of poly(ZnETPP) showing presence of Rh nanoparticles.....	98
3-16	External quantum efficiency vs. current density for a) poly(ZnETPP) b) poly(ZnETPP) _{0.5} -co-(PE) _{0.5} , c) poly(ZnETPP) _{0.5} -co-(PEOXAD) _{0.5} d) poly(ZnETPP) _{0.5} -co-(3,5CF ₃ PE) _{0.5} as a function of wt% of polystyrene (● = 0 wt%), (■ = 25 wt%), (▲ = 40 wt%) and (◆ = 50 wt%)	99
4-1	Molecule proposed to increase emission quantum yield.....	108
4-2	Conjugated polymer, PPE, containing substituted porphyrin and oxadiazole in main chain.	110
4-3	Scheme of a free radical chain growth mechanism.	111
4-4	Structures of monomers.	112

4-5	Structure of TP polymer.....	113
4-6	Synthesis of YbTPP-TP polymer.....	113
4-7	Absorption spectrum of YbTPP-TP polymer.....	114
4-8	NIR emission spectrum of YbTPP-TP polymer.....	114

Abstract of Dissertation Presented to the Graduate School
of the University of Florida in Partial Fulfillment of the
Requirements for the Degree of Doctor of Philosophy

ELECTROLUMINESCENCE AND PHOTOPHYSICAL PROPERTIES OF NEAR-
INFRARED LUMINESCENT LANTHANIDE (III) MONOPORPHYRINATE
COMPLEXES AND PENDANT POLYMERS

By

Garry Brian Cunningham

December 2005

Chair: Kirk S. Schanze
Major Department: Chemistry

The photoluminescent and electroluminescent properties of substituted lanthanide monoporphyrinate complexes were investigated. The lanthanide complexes consisted of a lanthanide (Yb^{3+}) coordinated to a substituted porphyrin, 5,10,15,20-tetraphenylporphyrin (TPP), 5,10,15,20-tetrakis(3,4,5-trimethoxyphenyl)porphyrin(TMPP), 5,10,15,20-tetra(4-pyridyl)porphyrin (TPyP), or 5,10,15,20-tetra(4(2'-ethylhexyloxy)porphyrin (TPP_OEH) and a capping ligand, L. The capping ligand was either an tris-pyrazoylborate (TP), (cyclopentadienyl)tris(diethoxyphosphito-P)cobaltate ($\text{L}(\text{OEt})_3$) or quinolinato (Q) anion. The complexes were synthesized to influence the electronic properties of the complex. The optical absorption and emission of these complexes resembled previously studied lanthanide porphyrin complexes, with photoluminescent yields ranging from 0.01 to 0.04. Electroluminescence was observed for the porphyrin complexes blended into polystyrene. External quantum efficiencies were typically 10^{-4} , suggesting that changes to the

porphyrin structure have little effect on the electronic nature of the complex. Blending the electron transporting AlQ₃ into the device improved the external quantum efficiencies by an order of magnitude, suggesting that carrier transport is the culprit for poor device performance.

Conjugated polyacetylenes containing a Zinc porphyrin pendant were synthesized by an insertion type polymerization using [Rh(NBD)Cl]₂. The homopolymer (poly(ZnETPP) and copolymers of ethynyl benzene (poly(ZnETPP)-co-(PE)), an oxadiazole containing group (poly(ZnETPP)-co-(PEOXAD), or 1-ethynyl-3,5-trifluoromethylbenzene (poly(ZnETPP)-co-(3,5CF₃PE) were synthesized. The optical properties were studied and it was found that the homopolymer exhibited excitonic coupling due to the overlap of the porphyrin pendants. Substitution of other comonomers reduced this coupling allowing the return of typical ZnTPP optical properties. Neither absorption nor emission from the polyacetylene backbone was identified. A thermally induced cis to trans isomerization was observed for the homopolymer, poly(ZnETPP), with the emergence of polyacetylene backbone emission. Electroluminescent devices were fabricated using the polymers neat or in a blend with polystyrene. The electroluminescent performance of the homopolymer was poor with a maximum external quantum efficiency of 10⁻⁶. Addition of polystyrene increased the efficiency 10-fold. The copolymers with PE also showed similar characteristics. The copolymers with either PEOXAD or 3,5CF₃PE further increased the external efficiency by an order of magnitude. This suggest that adding hole blocking / electron transporting pendants to the polymer further enhances carrier transport, allowing for more efficient devices.

CHAPTER 1 INTRODUCTION

This chapter provides an overview of several topics. The first topic focuses on the fundamental processes that occur when molecules interact with light. The second part will focus on the electronic properties of lanthanides. The third part will focus on the photophysical and redox properties of porphyrins. The fourth part will focus on the basics of electroluminescence and light emitting diodes. The final part presents the up-to-date literature overview of organic and polymer complexes used in light emitting diodes, with an emphasis on near-infrared light emission.

Electrodynamics

Absorption of Light

The perturbation of matter with light gives insight into its electronic structure. When a molecule absorbs a photon of sufficiently high energy, one of its valence (HOMO, highest occupied molecular orbital, for organic systems) electrons is promoted into an excited energetic state (LUMO + n ; $n = 0 \dots \infty$). The frequency of the light provides information about the energy difference between the two orbital energy levels involved in the transition. The fundamental process of the absorption of light at a given frequency is given by the formula:

$$A = -\log \frac{I}{I_0} = \epsilon bc \quad (0.1)$$

which is known as the Beer-Lambert law, where A is the absorption, I is the light intensity at a given frequency measured after interaction with the sample, I_0 is the light

intensity at a given frequency measured before the sample, b is the pathlength of the sample measured in cm., and c is the concentration of the sample given in molarity. The units for the intensity of the absorption band are given by the term, ϵ , and measured in $M^{-1}cm^{-1}$. The absorptivity is proportional to the transition dipole between the ground and final states. If the dipole moment is zero, the absorption coefficient is also zero.

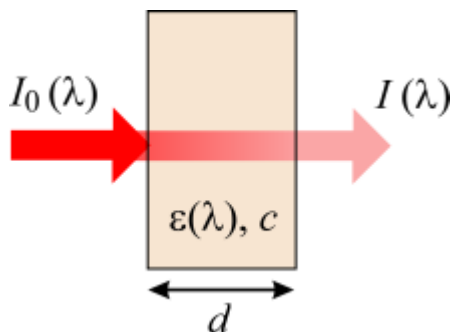


Figure 1-1. Schematic of absorption shown as a function of thickness, concentration, and molar absorptivity.

The absorption spectra of molecules differ greatly than that of free ions, due to coupling of vibrational transitions (phonons) with the electronic transitions. The absorption is broadened and split into bands. This process is known as electron-phonon coupling. According to the Franck-Condon principle, the electronic process of absorption takes place on a faster timescale than the nuclei can respond. The equilibrium distance between the nuclei involved in a given vibrational transition occurs at the potential energy minima. When an electron is promoted to a higher energy level, the charge distribution of the molecule is changed, and the initial position of nuclei is no longer the lowest in energy. The nuclei will attempt to equilibrate, but this process is slow with respect to the time scale of light absorption (10^{-13} s: 10^{-15} s). Therefore, the transition occurs from the lowest ground vibrational state to multiple vibrational levels of the excited state, as shown in Figure 1-2.

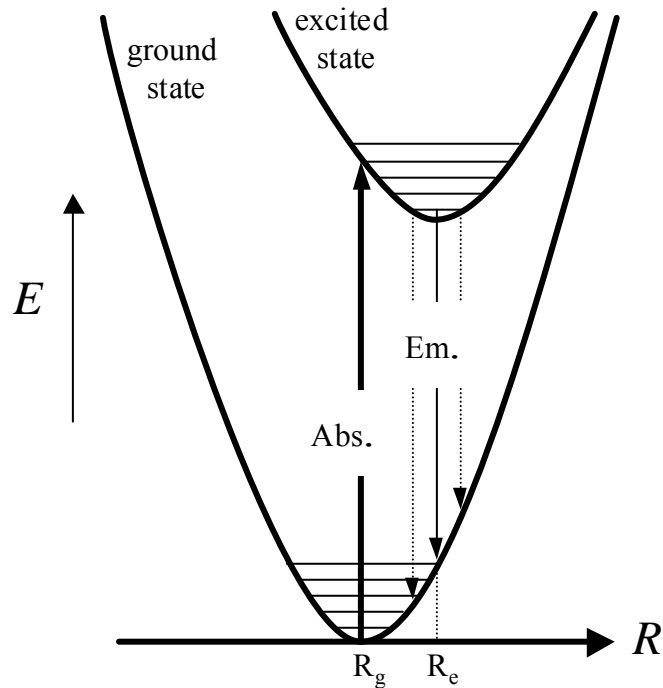


Figure 1-2. Configuration coordinate model.

Emission of Light

The photoluminescence process can best be described using the general configuration coordinate diagram (Figure 1-2). A configuration coordinate diagram is a plot of the energy of electronic ground and excited states as a function of a generalized configuration coordinate R that accounts for the nuclear configuration of nearest neighbors about the excited nuclei. As shown by R_g and R_e , the equilibrium configuration coordinate differs in the ground and excited states. Wavefunctions of excited states are typically more spatially extended than those of the ground state. This leads to the energy minima of the excited state, R_e , to be shifted with respect to the ground state energy minima. Upon absorption of a photon, the center is promoted into an excited vibrational state of an excited electronic state. The terminal state of the absorption transition is at a higher-energy point than the minimum of the excited state.

The lifetime of allowed excited states is $\sim 10^{-8}$ seconds and is much longer than the lattice vibrational period. Therefore, just after absorption, the complex undergoes a phonon assisted relaxation to the energy minima of the excited state. This process is also known as internal conversion (IC) (see Figure 1-3). The molecule loses its excess vibrational energy by interaction with solvent or other solute molecules.

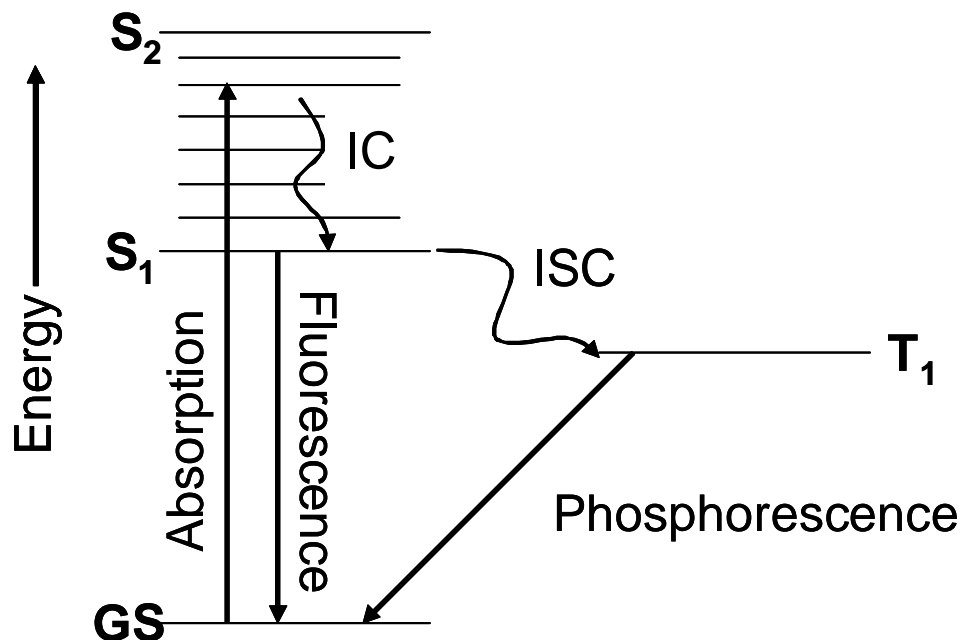


Figure 1-3. Jablonski diagram showing the fundamental processes of absorption, internal conversion, fluorescence, intersystem crossing, and phosphorescence.

The chromophore can radiatively return to a vibrationally excited ground state by the emission of a photon. This process is called fluorescence. Fluorescence is an allowed process because it involves a transition of two states with the same spin. Half of the energy difference between the emission and absorption energies is known as the Stokes shift. The Stokes shift depends on the relative position and curvature of the configuration coordinate parabolas, shown in Figure 1-4.

The excited chromophore can also undergo a process known as inter-system crossing (ISC). This process happens when the excited state electron spin changes to produce the triplet state. This process involves coupling of the singlet and triplet vibrational levels of the same energy to produce a vibrationally excited triplet state. This process is followed by internal conversion to the triplet state in the lowest vibrational level ($v = 0$). Once a molecule has undergone intersystem crossing, it can return to the ground state by emission of a photon. This process is called phosphorescence.

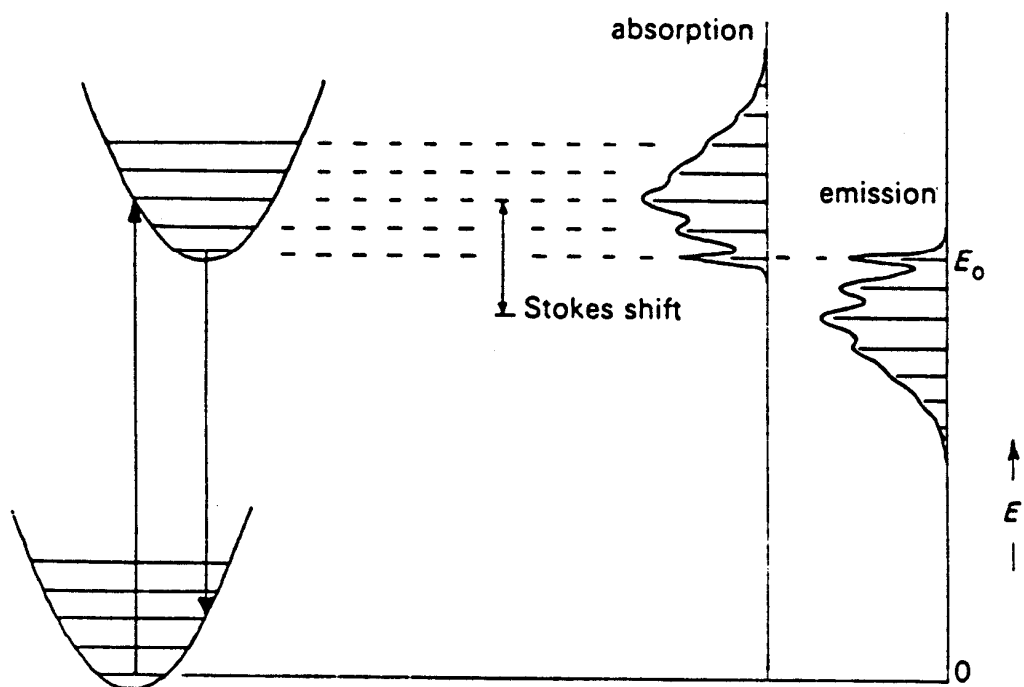


Figure 1-4. Configuration coordinate diagram showing the zero-phonon line and illustrating the process known as the Stoke's shift.^[1]

The ability of a molecule to undergo intersystem crossing, although quantum mechanically forbidden, is facilitated by the presence of strong spin-orbit coupling. The spin and orbital angular momentum are separately coupled and quantized. Therefore, the transitions between the states of opposite spin are forbidden by the conservation of

momentum rule. This is the typical case for molecules with small Z numbers (e.g., organic molecules). This situation is changed by the presence of atoms with large Z numbers. This is called the heavy atom effect. With these heavy atoms, a significant mixing of the spin angular momentum and orbital angular momentum of the same electron occurs. Because of this mixing, the two momenta are not separately conserved, but the total angular momentum is conserved. This is called spin-orbit coupling, and it leads to the increase in inter-system crossing rates. This process is shown in Figure 1-6. Due to the large nuclear charge present, a magnetic field is produced about the electron with a directionality perpendicular to the plane of the orbit. A magnetic field is also being produced by the electron spin motion and is directed along the spin axis. The interaction of these two magnetic fields is called spin-orbit coupling. The magnitude of this effect is controlled by the nuclear charge of the heavy atom as well as by the position of the atom in the molecule.

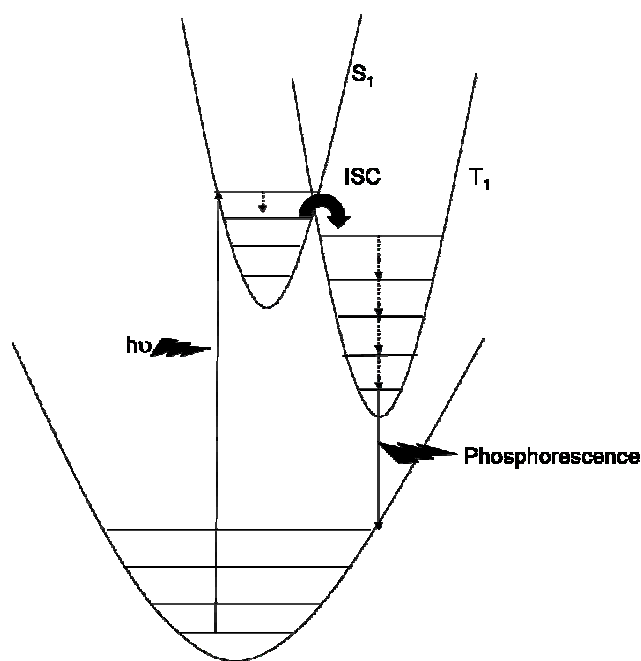


Figure 1-5. Configuration coordinate model showing the process of phosphorescence.

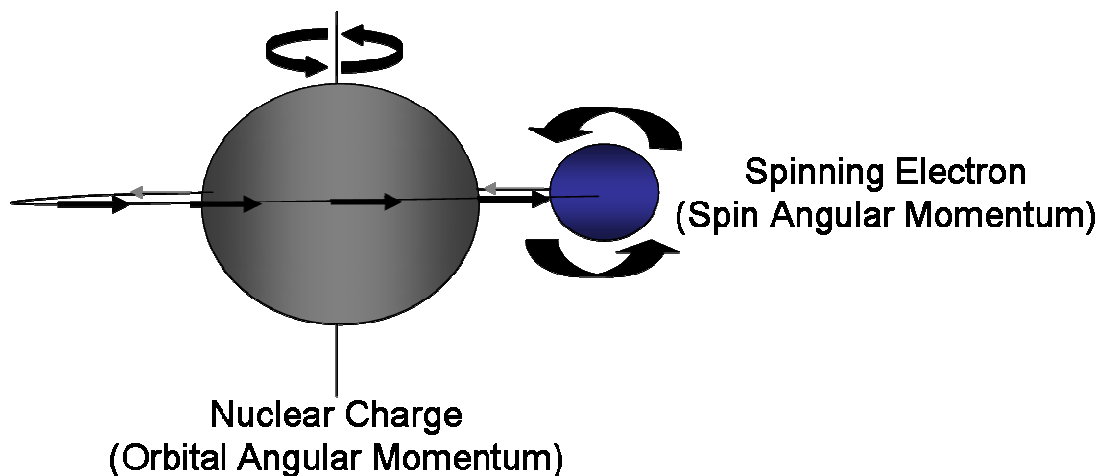


Figure 1-6. Interaction of atom nuclear charge induced angular momentum interacting with electron's spin angular momentum, resulting in spin-orbit coupling.

The lifetime of an excited state and luminescent efficiency depend on the rates of the radiative and nonradiative transitions from (and to) the excited state. Highly allowed transitions have fast rates and contribute to short lifetimes and high efficiencies. A strongly competing non-radiative rate will result in both a shorter lifetime and lower luminescent efficiency. Radiative emission can be considered to be emission of light from an excited state of a complex designated as M^* :

$$M^* = M + \hbar\omega \quad (0.2)$$

This emission is considered a random process, and therefore follows first-order kinetics:^[2]

$$\frac{-d[M^*]}{dt} = k_r[M^*] \quad (0.3)$$

If it is a single process, the decay should be characterized by a single exponential, which can be expressed by a single rate constant k_d . The lifetime can also be expressed in terms of the lifetime (τ_r) of the excited state by the equation:

$$\tau_r = \frac{1}{k_d} \quad (0.4)$$

The rate constant usually has the units of s^{-1} . Therefore the lifetime has the units of s.

The decay of the excited state can occur by many different possible pathways such as the emission of light, intersystem crossing, and internal conversion. The radiative rate constant is therefore the sum of all of the processes which lead to a lower concentration of the excited state. The equation below shows the relationship between the rate of fluorescence (k_f), the rate of intersystem crossing (k_{isc}), the rate of internal conversion (k_{ic}) and the rate of phosphorescence (k_p).

$$k_d = k_f + k_{isc} + k_{ic} + k_p \quad (0.5)$$

Nonradiative Decay

Radiative return from the excited state is not the only possibility of completing the cycle. The alternative is nonradiative decay, which means a return without the emission of radiation.^[1] Nonradiative processes compete with radiative processes. These nonradiative returns affect the emission efficiency of the sample. Emission efficiency is simply derived as the number of photons emitted by the sample divided by the number of photons absorbed by the sample.

There are several different ways that nonradiative decay can occur. These processes are shown in Figure 1-7. In Figure 1-7a absorption and emission processes are possible and Stokes shifted relative to each other. The relaxed-excited state may reach the crossing of the two parabolas if the temperature is high enough. Via the crossing it is possible to return to the ground state in a nonradiative manner. The excitation energy is then given up as heat to the lattice. This accounts for one of the possible thermal quenching mechanisms.

In Figure 1-7b, the parabolas are parallel ($S = 0$) and will never cross, assuming that both states have the same force constant. It is impossible to reach the ground state in the way described above. However, nonradiative return to the ground state is possible if certain conditions are met. The energy difference between the two states, ΔE , must be equal to or less than 4-5 times the higher vibrational frequency of the lattice. In that case, this amount of energy can simultaneously excite a few high-energy phonons, and then is lost for the radiative process. The quantitative description of this process is called the energy gap law.^[3-9] This process is also called multi-phonon emission.

The third process consists of an electronic crossover with another excited state. This excited state could be a higher or lower energy excited state. This is the fundamental process involved in intersystem crossing.

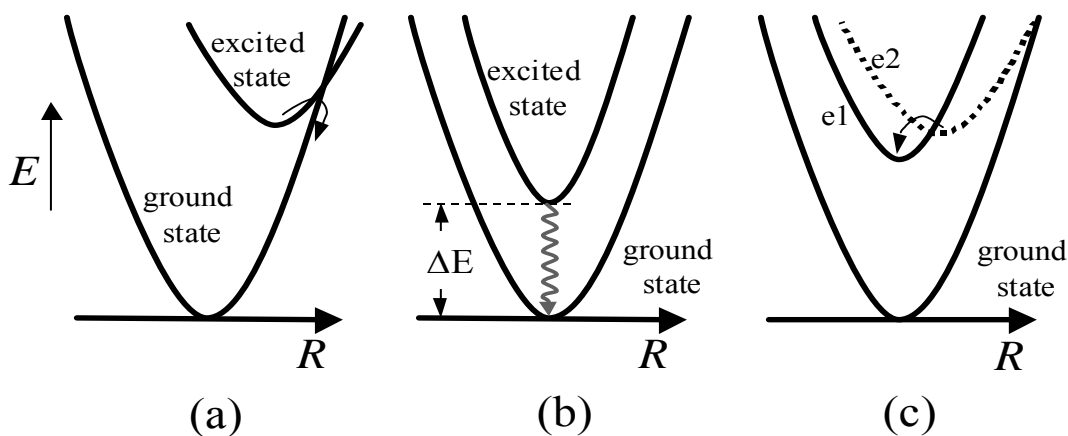
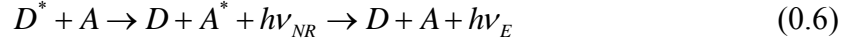


Figure 1-7. Typical nonradiative processes through (a) crossover with a ground state, (b) multiphonon emission, and (c) crossover with an excited state. ^[1]

Energy Transfer

The final process that a molecule can use to relax from the excited state is through energy transfer. The process of energy transfer occurs when an excited donor molecule D^* transfers its energy to an acceptor in the ground state A , which is then promoted to an excited state:



where $h\nu_E$ and $h\nu_{NR}$ are, respectively, the emission and nonradiative decay created in the process. In other words, the energy of one molecule can be transferred to another molecule, which quenches the luminescence of the host and increases that of the guest.

The interaction between D^* and A is described by the perturbation Hamiltonian, H' . The $D^* + A$ state is not considered a stationary state of the total Hamiltonian but is able to evolve into other isoenergetic states, such as $D + A^*$. The use of time-dependent perturbation theory assigns the probability of the evolution from $D^* + A$, given by Ψ_i , to the $D + A^*$ state, described by Ψ_f , as

$$P \propto \rho \langle \Psi_i | H' | \Psi_f \rangle^2 \quad (0.7)$$

where ρ is the density of the coupled isoenergetic donor-acceptor transitions. For typical systems, ρ can be determined by calculating the overlap integral of donor luminescence and acceptor absorption. In general, after the excited state transfers from D^* to A it rapidly relaxes nonradiatively to the lowest vibrational level of A^* .

The perturbation Hamiltonian contains several terms; the most important are the electrostatic (Förster) and electron exchange (Dexter) interactions. Both terms are capable of inducing energy transfer. The electrostatic interaction can be expressed as a series of multipole-multipole terms. The most common interaction, dipole-dipole, was described by Förster who discovered that the rate of energy transfer depended on the distance R between the donor and acceptor molecules:^[10]

$$k_{ET}(R) = \left(\frac{1}{\tau} \right) \left(\frac{R_0}{R} \right)^6 \quad (0.8)$$

where R_0 is called the Förster radius, and τ is the average donor emission lifetime in the absence of energy transfer corresponding to rate $k_D = 1/\tau$. When R is equal to R_0 then $k_{ET} = k_D$. The critical distance R_0 , which is the distance between the donor and acceptor where the efficiency of energy transfer is 50%, is given by the integral over all wavelengths λ :

$$R_0^6 = 1.25 \times 10^{17} \frac{\phi_E}{n^4 c^3} \int F_D(\lambda) \alpha_A(\lambda) \lambda^2 d\lambda \quad (0.9)$$

where ϕ_E is the quantum efficiency of donor emission, n is the refractive index of the host, F_D is the normalized emission spectrum of the donor, and α_A is the molar extinction coefficient of the acceptor. It has been shown that dipole-dipole interactions can be significant even at distances as large as 100\AA .^[11]

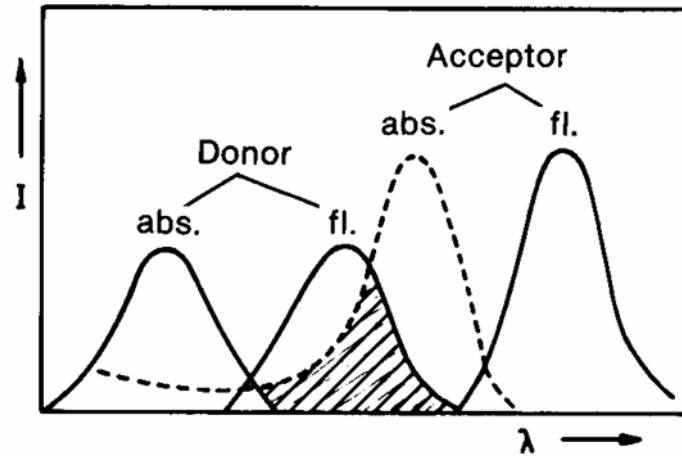


Figure 1-8. Schematic showing the overlap of donor fluorescence with the acceptor absorption, fundamental for Förster energy transfer.^[1]

In Förster energy transfer, the spins of both D and A are conserved. Therefore, the allowed transitions are



where the superscripts indicate the spin of the molecule. The triplet-singlet transition

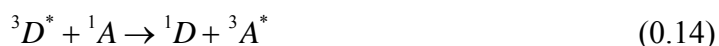


is forbidden, but is occasionally observed since the triplet excited donor has a long lifetime and k_{ET} can be faster than phosphorescence.

The process of energy transfer has also been extensively analyzed by Dexter^[12] to give

$$k_{ET}(R) \propto e^{-2R/L} \int F_D(\lambda) \alpha_A(\lambda) d\lambda \quad (0.13)$$

where R is the distance between D^* and A, and L is a constant. Because this process involves the exchange of electrons, it occurs only over short distances, $\sim 10\text{\AA}$. Under the Dexter transfer process, it is the total spin which is conserved. Therefore, triplet-triplet energy transfer is allowed.



Lanthanides

The previous sections focused on the electronic properties and fundamental processes of any molecule. This section will delve deeper into the unique properties which make up the metals known as the rare earths. The most impressive feature about the spectra of the lanthanide ions is the sharpness of the lines in absorption and emission spectra. The optical properties of the lanthanides were first discovered around 1908 by Becquerel.^[13] The trivalent (Ce^{3+} - Yb^{3+}) rare earths have an electronic configuration of $4f^n 5s^2 5p^6$ ($n=1-13$). The 4f electron shell is located within the 5s5p shell, and therefore the interaction with the ligand field is weak as compared to that of transition metals. This leads to the electronic properties of 4f levels in the complex to be similar to that of the free ion, and changing the overall ligand field has little effect on them.^[14] If the

lanthanides are modeled using the configuration-coordinate model shown in Figure 1-2, the situation corresponds to an excited state displacement of zero. This is stating that the $4f$ wavefunctions are not influenced to any great extent by excitation.

The energy structure of the lanthanides and their many different optical transitions were precisely investigated by Dieke^[15] in lanthanide fluoride hosts, and in LaCl_3 doped solids by Crosswhite.^[16] Figure 1-10 shows the energy level diagrams for several selected trivalent rare earths. These diagrams are quite useful in understanding their luminescence characteristics. Energy levels prescribed by the inner quantum number J are further split into several sublevels in the solid state by the Stark effect of the crystal field. The number of split sublevels is dependant on the symmetry of the crystal field, and is limited to $2J + 1$ for integer values of J and $J + \frac{1}{2}$ for J of half-integer values.

The absorption of lanthanides is plagued by low oscillator strengths. Transitions within the $4f$ manifold take place within states of the same parity, and therefore are electric dipole forbidden. Oscillator strengths of $f \rightarrow f$ transitions that are made electric-dipole allowed by crystal fields are $10^{-5} - 10^{-8}$, dependent on whether the site has inversion symmetry. The uneven components of the crystal field mix a small amount of opposite parity wavefunctions into the $4f$ wavefunctions. This process is sometimes called "intensity stealing."^[17-21] Magnetic dipole interactions within the $4f$ manifold are allowed and are sometimes observed. The oscillator strengths associated with these transitions are in the range of $10^{-7} - 10^{-8}$.

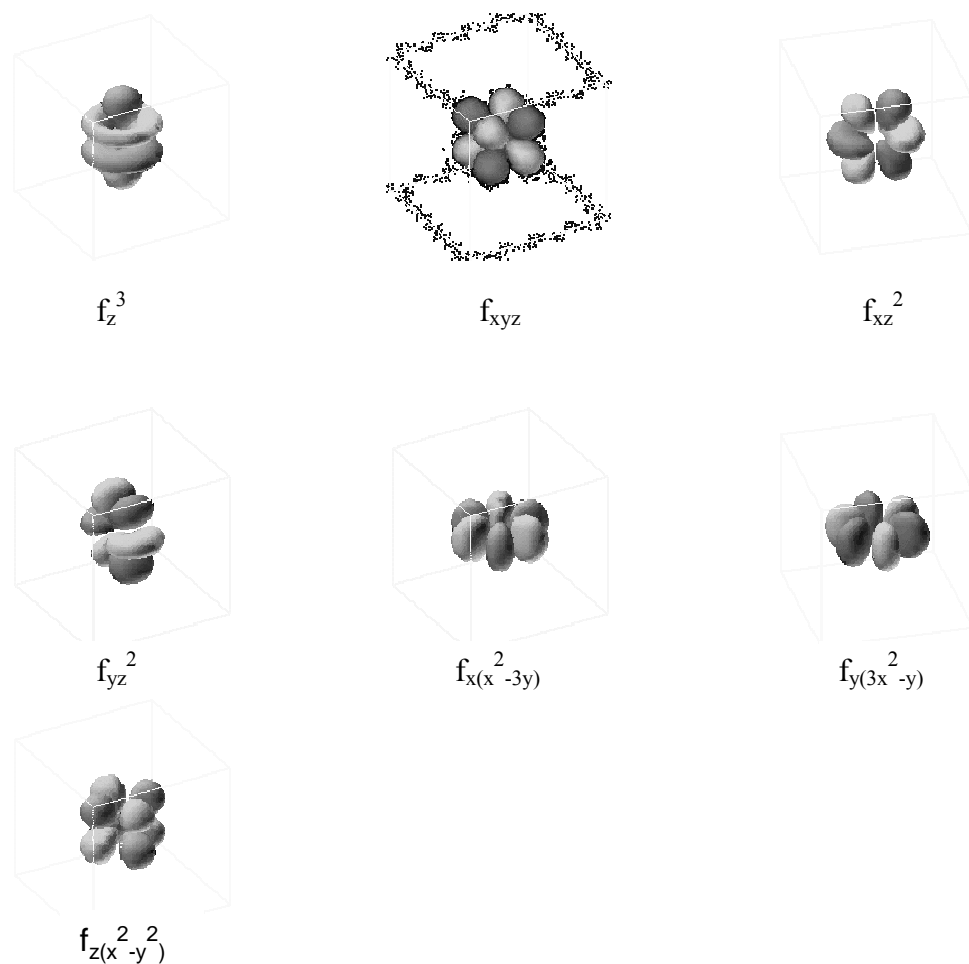


Figure 1.9. Graphical description of f orbitals.^[22]

The ability of a ligand to sensitize the $f \rightarrow f$ emission transition was discovered in 1942 by Weissman.^[23] He found that the $\pi \rightarrow \pi^*$ transitions of beta-diketonates could sensitize Eu^{3+} emission. The mechanism for this transition is that the molecule is excited from the singlet ground state to a singlet excited state ($S_0 \rightarrow S_n$). The S_n state decays into the lowest energy singlet excited state on the ligand ($S_n \rightarrow S_1$). The singlet state undergoes intersystem crossing into the ligand-based triplet state ($S_1 \rightarrow T_1$). The ligand then transfers its energy to the lanthanide, resulting in a lanthanide in the excited state. The lanthanide then can undergo radiative decay to the ground state, releasing a photon.

The importance of this discovery was soon realized, and further efforts were undertaken to attempt to improve the efficiency of lanthanide emission. Most of the work focused on use of β -diketonates as the sensitizing ligands for this process, although many other organic ligands were also used. The bulk of this research will be discussed later in this chapter.

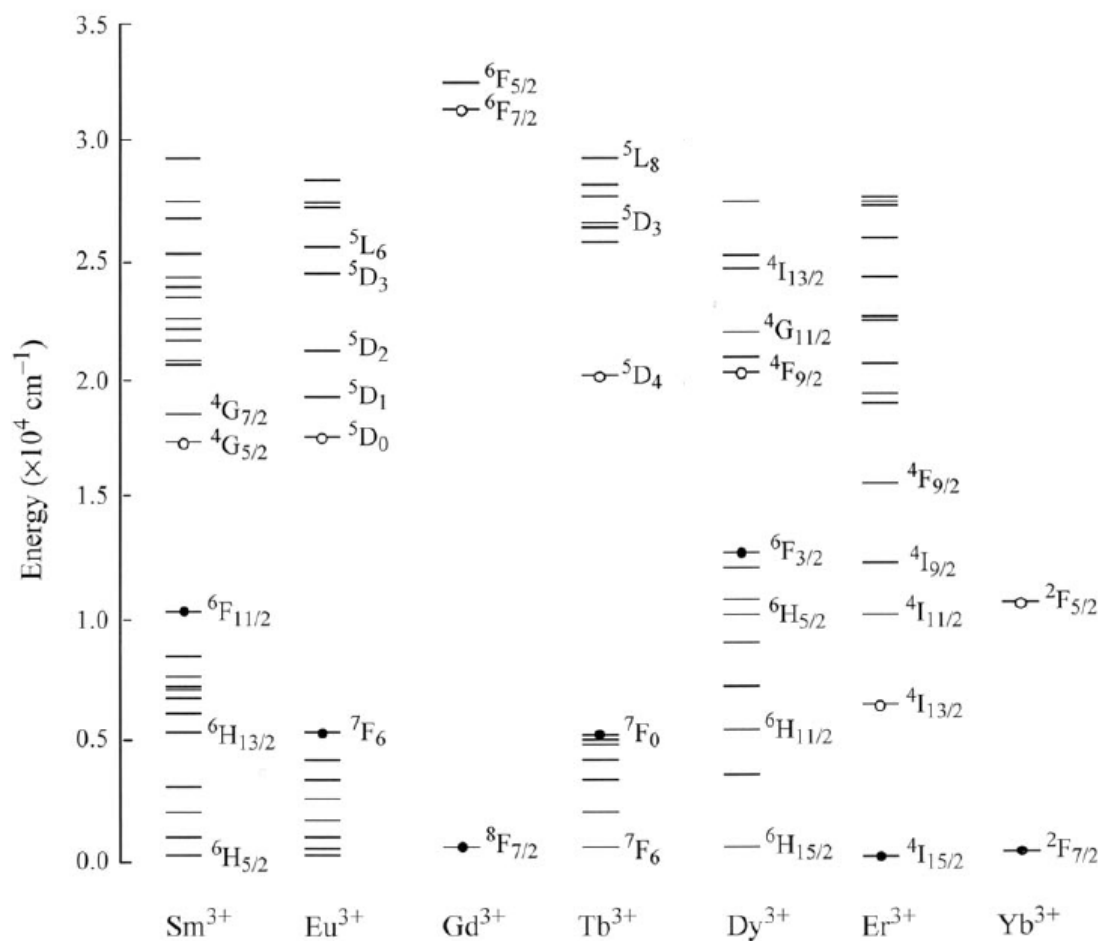


Figure 1-10. Energy level diagrams for selected rare earth ions in LnCl_3 . Unfilled circles indicate emissive states. ($\circ \rightarrow \bullet$)^[24]

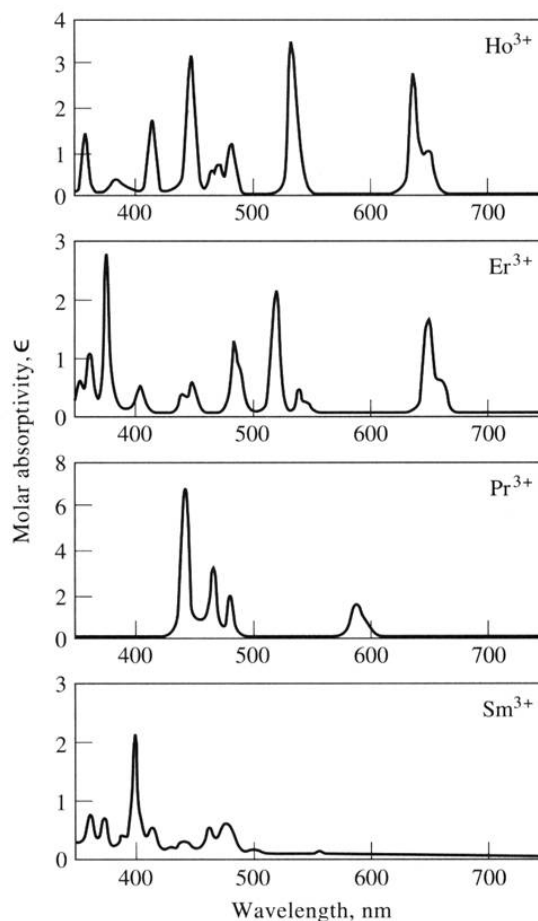


Figure 1-11. Absorption spectra of selected lanthanide ions, showing sharp absorption with low molar absorptivity. ^[17]

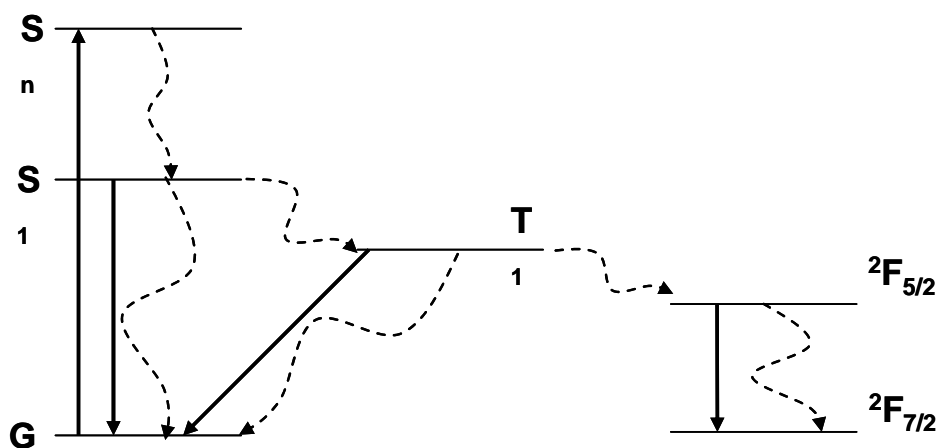


Figure 1-12. Jablonski energy diagram showing energy transfer from organic ligand to lanthanide metal, in this case Yb^{3+} . Dashed lines represent non-radiative decay.

Porphyrins

Porphyrins are among the most important molecules in nature. They are found in nearly every biological tissue.^[25] These compounds range from chlorophyll in plants to iron porphyrin (heme) in blood.^[26-28] Porphyrins are also important molecules in optical materials.^[29-32]

Porphyrins consist of a large macrocycle core consisting of 26π electrons. This core (see Figure 1-13) can be substituted upon by the addition of a metal and substitution along the periphery can be accomplished at either the meso or pyrrole position. The molecule can also be substituted upon by the introduction of an axial ligand.

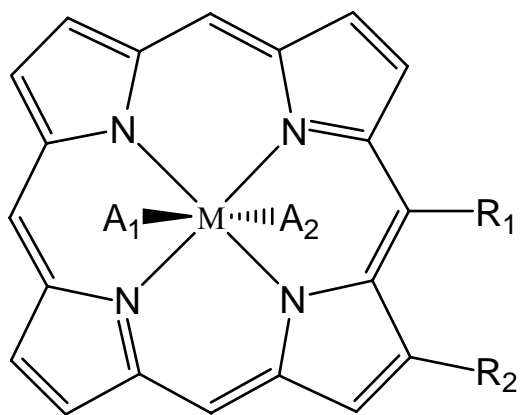


Figure 1-13. Structure of porphyrin macrocycle, showing possible areas of substitution.

Photophysics

The electronic structure giving rise to the absorption spectra of porphyrins and metalloporphyrins has been derived by a four orbital model.^[33-37] Given the D_{4h} symmetry of the porphyrin ring, four different molecular orbitals have been described, shown in Figure 1-14. The absorption bands in the visible region are described by transitions among the two highest occupied π orbitals of a_{1u} and a_{2u} symmetry with the doubly degenerate unoccupied π^* orbitals of e_g symmetry. Transitions from the a_{2u} state to the $e_g\pi^*$ state are the lowest in energy and called the Q bands. In the free base

porphyrins this leads to 4 bands ranging from 480-650 nm. In metalloporphyrins only two peaks are seen in the Q bands due to their lower symmetry.^[38] The intensity of this transition is relatively weak due to the fact that it is symmetry forbidden. The transition from the a_{1u} level to the $e_g\pi^*$ orbital is a strong absorption called the Soret or B band. It ranges from 380 – 430 nm and the large intensity ($\epsilon \approx 10^5 \text{ M}^{-1}\text{cm}^{-1}$) is due to the fact that it is symmetry allowed. The actual peak positions and absorption intensity are dependent on substituents on the porphyrins ring, central metal, and axial ligands.

The regular fluorescence spectra for porphyrins shows two bands which mirror the Q bands, along with the possibility of phosphorescence bands. The fluorescence bands for metalloporphyrins are typically found near 600 nm and the phosphorescence bands are found near 700 nm. In normal type porphyrins and metalloporphyrins the excited state energy diagram is fairly simplistic due to the fact that the lowest singlet and triplet states derive from the porphyrins π system.

Porphyrin complexes which have closed shell metals generally only show fluorescence in solution at room temperature, but have some phosphorescent component at low temperatures (77 K).^[39] The quantum yield for fluorescence decreases with increasing atomic number of the metal, as does the phosphorescence lifetime. The phosphorescent lifetime of these complexes is usually in the range of several hundreds of μs to several ms. The addition of a diamagnetic metal to the porphyrin core typically quenches the room temperature fluorescence.^[39] The relatively weak fluorescence and short triplet lifetimes are due to the fact that the lowest energy excited state is typically metal based and has little contribution from the porphyrin π system. The exceptions are Pt^{2+} and Pd^{2+} which show both room temperature fluorescence and phosphorescence, due

to the fact that the $d \rightarrow d$ splitting of these metals is large and the porphyrin π system plays the dominant role in the excited state.^[40, 41] Paramagnetic metal porphyrin complexes generally only show phosphorescence with relatively short lifetimes.

The effects of substituents on the porphyrin core have little effect on the fluorescence position and intensity. The substitution of “light” atoms typically leaves the fluorescence intensity and lifetime unchanged. The addition of heavy atoms at the pyrrole position has a dramatic influence on the emissive properties. For example, the addition of bromine atoms at the pyrrole position of CoTPP dramatically changed the λ_{max} of the Soret absorption.^[42] This led to a sharp decrease in the fluorescence intensity and a dramatic increase in the ISC yield, which in turn lead to a greater phosphorescence yield.^[43] This effect can be explained in two different ways. One is the fact that substitution at the pyrrole would cause a steric effect at the porphyrin core, therefore inducing a distortion of the normal planar structure. The second possible explanation is that the a_{1u} orbital is more sensitive to changes to the pyrrole than that of the a_{2u} orbital. The strong electron-donating substituents, Br, could induce an inversion of the ground state by destabilization of the a_{1u} level greater than that of the a_{2u} level.^[44]

Porphyrins tend to be useful ligands for the sensitization of lanthanide emission in the near-infrared due to their ease of excitation and their low energy triplet state. Lanthanide porphyrins are less well known than that of transition metal and alkaline earth metal porphyrins. The first examples of lanthanide monoporphyrinate complexes were demonstrated in 1976 by Horrocks *et al.*^[45] Since then, there have been several papers describing the use of porphyrins to sensitize the near-infrared emission from lanthanides.^[46-52] They showed that the coordinated lanthanide rapidly deactivates the

singlet state by inducing intersystem crossing to the triplet state. As a result of this fast intersystem crossing, most emission from the singlet states is quenched.^[53] Lanthanide porphyrins such as GdTPP(acac) in which the energy of the metal is too high to accept energy from the ligand triplet, show emission typical of heavy metal porphyrin complexes such as PtTPP.

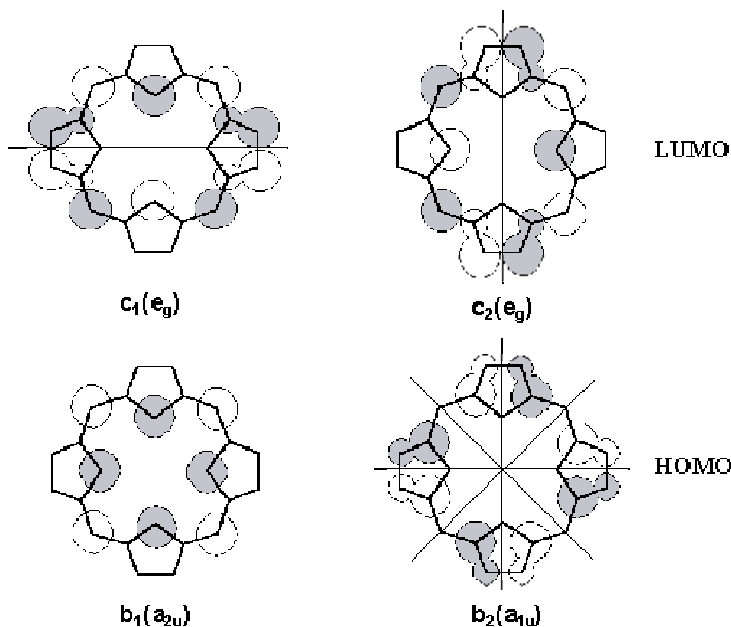


Figure 1-14. Molecular orbitals for the porphyrin macrocycle for the highest occupied molecular orbital and lowest unoccupied molecular orbital calculated using the Gouterman method.^[36]

Redox Properties

The use of electrochemical methods to estimate the redox properties of porphyrins is vital for understanding the photochemistry of porphyrins. In general, free-base porphyrins possess two oxidation peaks and two reduction peaks in cyclic voltammetry. These correspond to the one and two electron oxidation and reduction of the porphyrin π system. In “normal” metalloporphyrins a similar redox pattern is observed. The central metal cation simply acts as a substituent on the porphyrin ring. The redox properties

observed, exhibit a good correlation with the electronegativity or inductive parameter of the central metal atom.^[54, 55] Substituents on the porphyrin ring show a good correlation between the redox potentials and the Hamett σ values.^[54, 56] The electrochemical band gap corresponds well with the optical band gap determined by the lowest energy absorption in the Q band, indicating that the central metal and substituents equally effect the HOMO and LUMO levels.^[57] The number of substituents is also correlated with the shifts in the redox peak positions.^[58] Distortion from planarity seems to cause a dramatic change in the oxidation potential.^[54] The addition of a redox active metal complicates the overall electrochemical properties of porphyrins, due to the intervening oxidation and reduction potentials of the metal. The change in axial ligand also seems to play an important role in the redox potentials of porphyrins.^[59, 60]

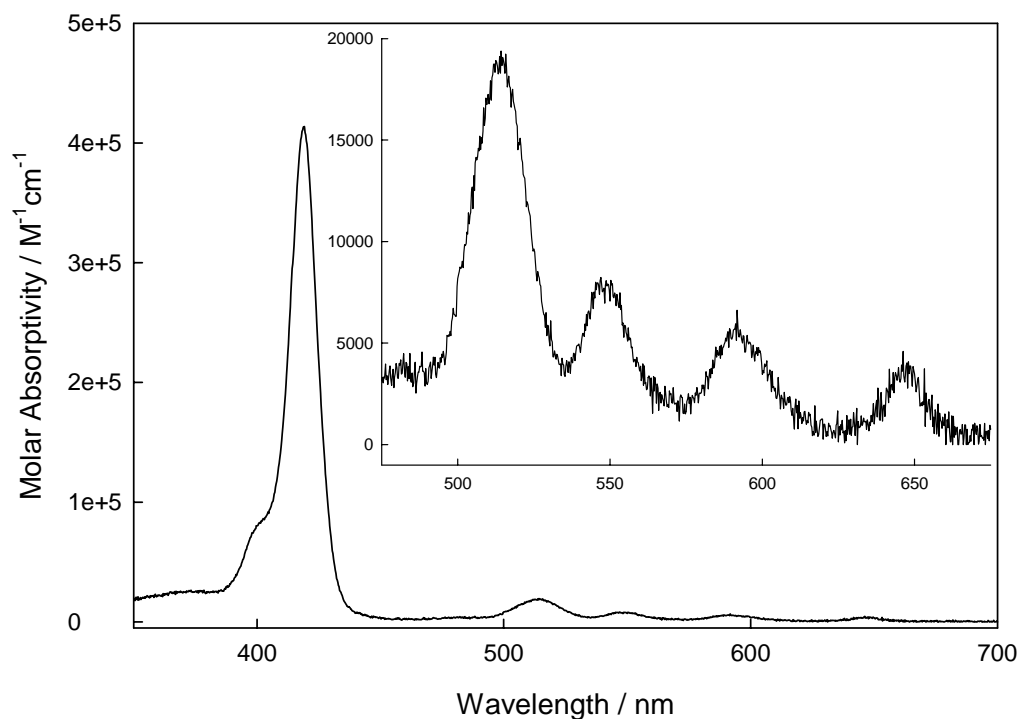


Figure 1-15. Absorption spectrum of tetraphenylporphyrin. Inset is magnification of Q-bands.

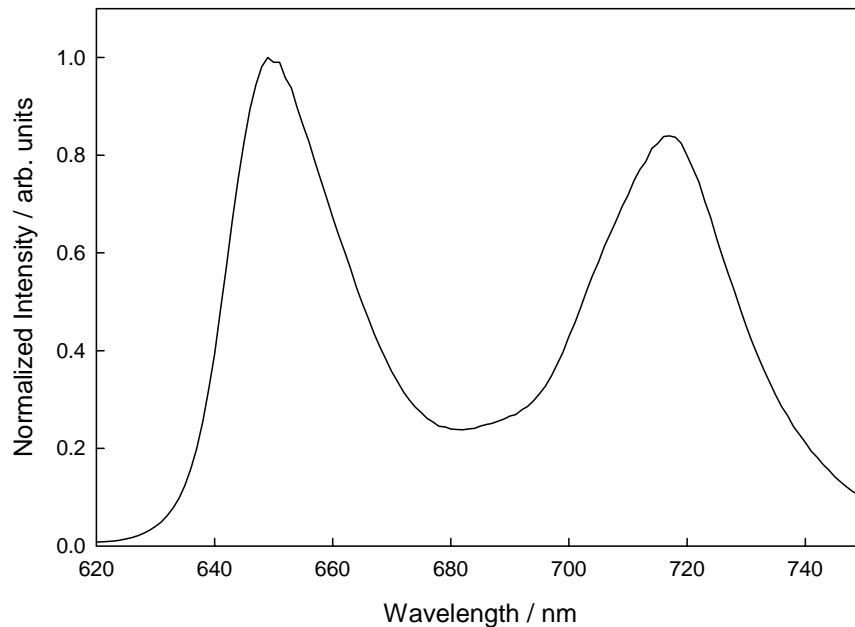


Figure 1-16. Fluorescence spectrum of tetraphenylporphyrin.

Synthesis

The synthesis of symmetric porphyrins involves the condensation of aldehydes with pyrroles in dilute solutions using catalytic amounts of an organic acid, organic base (Rothenmund synthesis, Figure 1-17) or strong Lewis acid followed by oxidation by such reagents as DDQ.^[61]

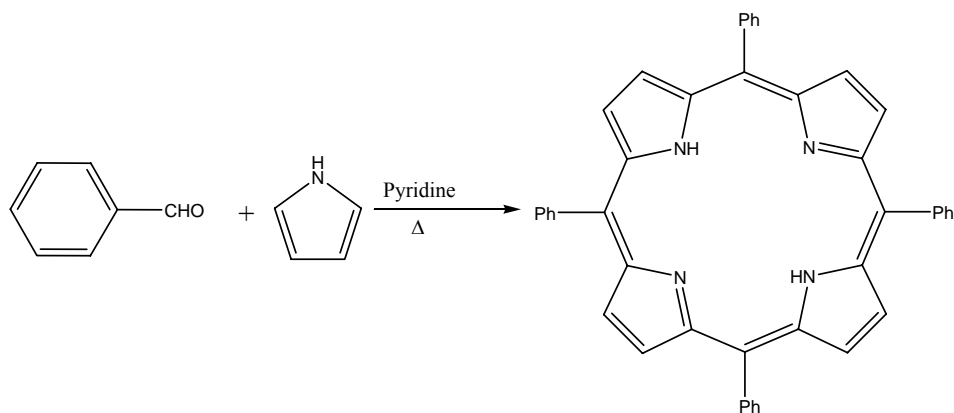


Figure 1-17. Schematic of Rothenmund synthesis.

The use of Lewis acids such as BF_3 (Lindsey method, Figure 1-18) generally leads to higher yields and milder reaction conditions.^[62, 63] The synthesis of asymmetric porphyrins according to the Lindsey method usually leads to a statistical distribution of mixed porphyrins, which can be difficult to separate.^[30] For porphyrins of the A_2B_2 type a 2 + 2 condensation of dipyrromethanes with aldehydes shown in Figure 1-19 is typically utilized..

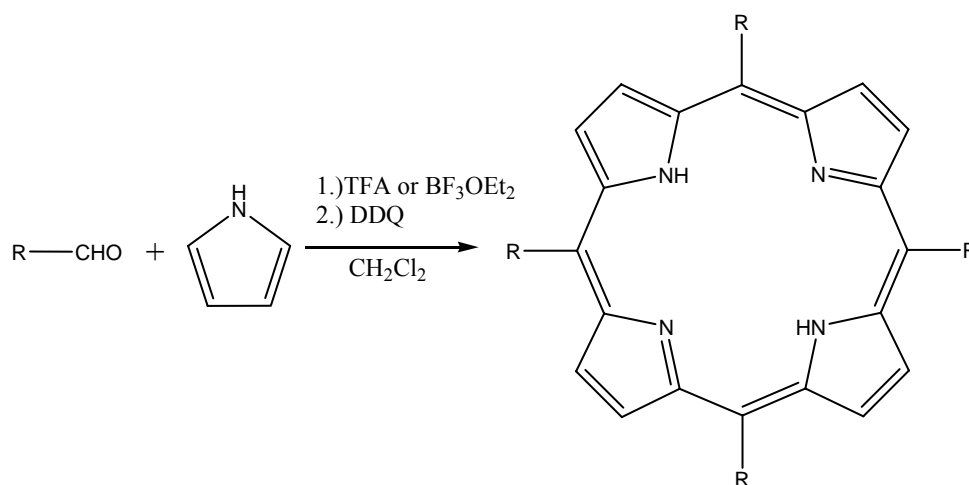


Figure 1-18. Schematic of Lindsey synthesis of porphyrins.

The metallation of porphyrins is typically simple. It involves stirring the free base porphyrin in a solution containing the metal organic complex or metal salt. This procedure works well for metals with a small ionic radius, such as Zn and Mg, but not as well for metals such as Pd or Pt. The larger metals require much higher temperatures and harsh conditions for insertion into the porphyrin core.

Lanthanides, for example, require stirring in acetylacetonone at 220°C in the presence of $\text{Ln}(\text{acac})_3$ and the porphyrin, resulting in the lanthanide porphyrin acetylacetonate complexes in relatively low yield.^[45, 64] This low yield is due to the fact that the complexes hydrolyze during the considerably long column chromatography times

necessary to separate the product. This method is also limited by the fact that the axial ligand is restricted to acac, due to the fact that the axial acac ligand is not very labile. Substitution of the diketonates can be achieved, but the high temperatures and harsh conditions results in significantly low yield.^[65-67] Lanthanide porphyrins have also been synthesized by amine or alkane elimination reactions of neutral lanthanide amides or alkyls with the free base porphyrin.^[68, 69]

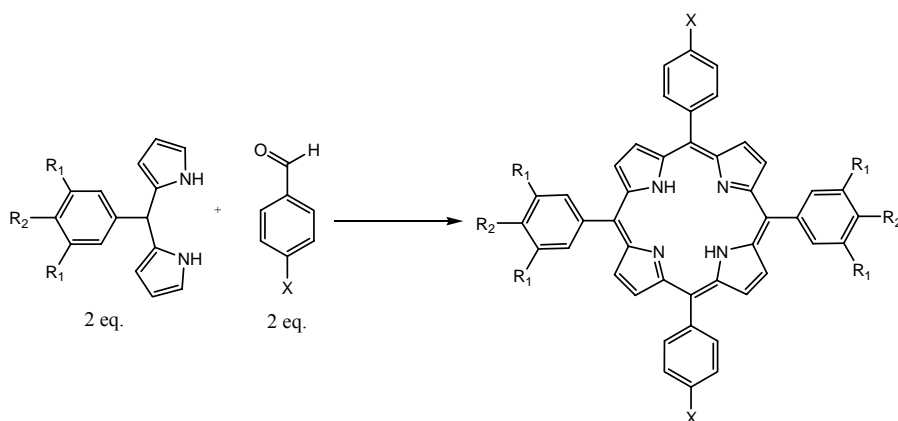


Figure 1-19. Schematic of 2 + 2 condensation method for synthesis A₂B₂ type porphyrins.

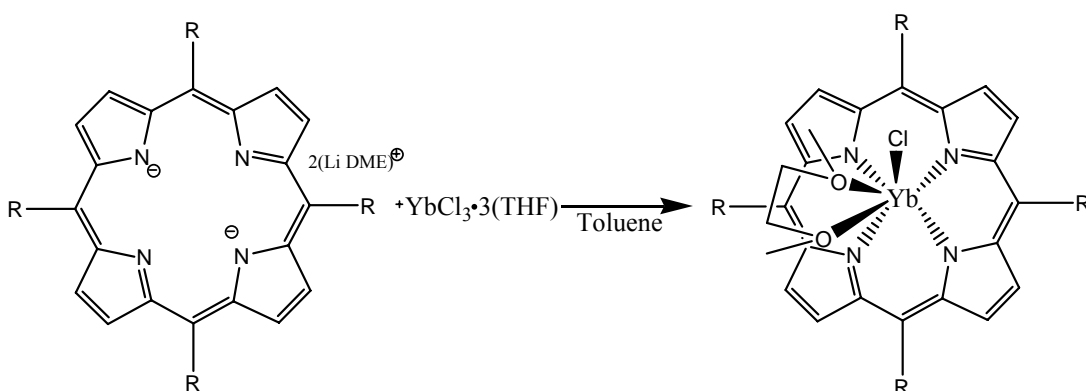


Figure 1-20. Schematic of lanthanide metallation of porphyrins using the Foley method.

Most recently, the Boncella group devised a method which increased the overall metallation yield. This lanthanide porphyrin complexes were synthesized by nucleophilic displacement of the halogen (Cl⁻ or I⁻) from anhydrous LnCl₃ or LnI₃ in the presence of

dilithiated porphyrin.^[70] This procedure allows for the simple substitution of the axial ligand by reaction of the Ln porphyrin halide complex with the potassium salt of the axial ligand.

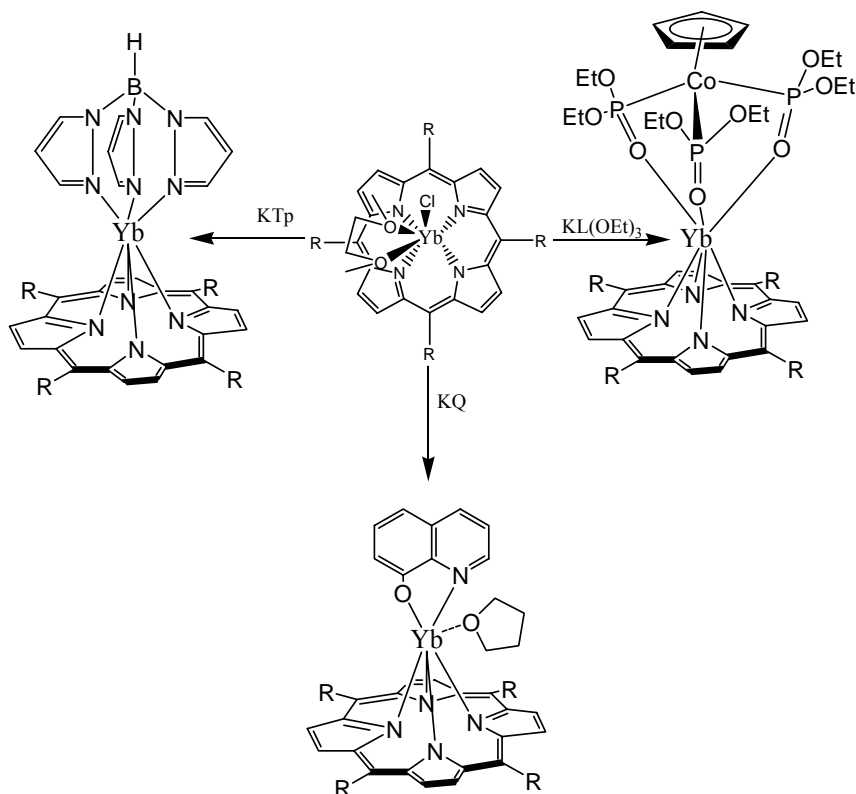


Figure 1-21. Axial substitution of lanthanide metalloporphyrins using salt metathesis.

Light Emitting Diodes

Research into the field of organic electroluminescent materials has grown dramatically since its inception. Electroluminescence of organic materials was first observed in 1963 in anthracene crystals.^[71, 72] However, due to the low efficiencies and high field strengths required, research into organic based electroluminescent materials was forgotten until Tang and Van Slyke prepared devices containing vapor deposited aluminum *tris*-(8-hydroxyquinolate)(Alq₃).^[73] An important discovery in the field of

organic based LED's came in 1990, when Friend produced the first polymer based device from poly(p-phenylenevinylene) (PPV).^[74]

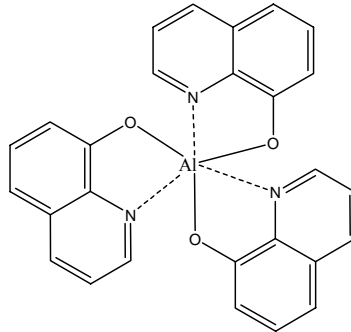


Figure 1-22. Structure of aluminum *tris*-quinolate.

Electroluminescence is the direct conversion of electrical energy into light. Electroluminescence was first described in the literature by Destriau in 1936.^[75] This paper showed electroluminescence from a semiconductor, ZnS, embedded into a dielectric matrix under high electric field. This led to high field electroluminescent materials.

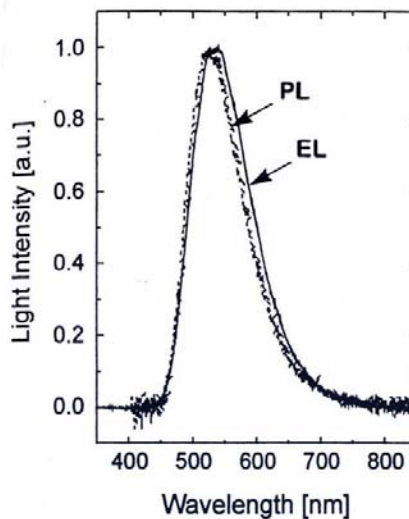


Figure 1-23. Photoluminescence and electroluminescence spectra of Alq₃.^[73]

Inorganic light emitting diodes are simple with respect to their operation. Forward current is driven over a p-n junction and electron-hole recombination occurs through

shallow states or in quantum wells. The tuning of the emission is done by choosing the correct ratio of starting materials. The major problem with these devices is that only single crystalline material is capable of exercising this type of recombination radiation efficiently enough for practical use. This means that one must obtain epitaxial growth on cheap substrates, which is not an easy task. Because of this limitation of inorganic LED use, researchers looked for other forms of electroluminescence and materials that could work in amorphous or polycrystalline films. This mainly led to the field of organic light emitting diodes (OLEDs) and polymer light emitting diodes (PLEDs).

The term LED used for the device structure is well justified in the fact that the basic mechanism is an injection of electrons and holes into a heterojunction, and a radiative recombination of excitons formed from the electron and holes. There are several points which differentiate inorganic light emitting diodes (ILED) from OLEDs and PLEDs. The main point is the low mobility of the carriers in organic systems, approximately five or six orders of magnitude lower than that of typical III – V type semiconductor systems. This is caused by the fact that the organic molecules and polymers used in these systems are amorphous and therefore the main pathway for carrier transport is a hopping mechanism. This causes an appreciable drop in voltage across the film thickness. The differences in spectral width are also dramatic. ILEDs have typically narrow linewidths, approximately 10 – 25 nm, whereas organic systems and polymers typically have linewidths typically on the order of 100 nm.

Most luminescent organic molecules are considered π conjugated compounds. That is, there exists an alternating series of single and double (triple) bonds. Due to this overlap of the π orbital wavefunctions of these adjacent atoms, the electrons occupying

these orbitals are relatively delocalized.^[76] In a perfect polymer the delocalized π electron cloud would extend along the entire length of the chain, but impurities and defects tend to break the conjugation. In the typical polymer film, the length of a conjugated segment rarely exceeds 15 repeat units.^[77]

There are two major barriers to highly efficient displays constructed of simple organic materials or polymers. The first major drawback comes in the form of spin statistics. Spin statistics shows that 25% of all excitations created by charge recombination produce the singlet excited state, while 75% results in the triplet. Since most organic materials do not phosphoresce, this energy is lost as heat. The second major barrier is the previously discussed problem of broad emission. In order to create efficient displays, there must be excellent color purity and good color saturation. Color saturation is difficult with the broad spectral width of organic and polymer emission. In order to fix the problem created by the quantum mechanical distribution of excited states, a material which shows phosphorescence must be used. This typically involved using heavy metal chelate complexes, such as $\text{Ir}(\text{ppy})_3$.^[78] While the problem of spin statistics has been taken care of, there is still the problem of color purity. This problem can be fixed by the use of lanthanide complexes. Since lanthanide emission is narrow, there can be efficient color saturation. Lanthanides also induce the heavy atom effect, which solves the first problem as well.

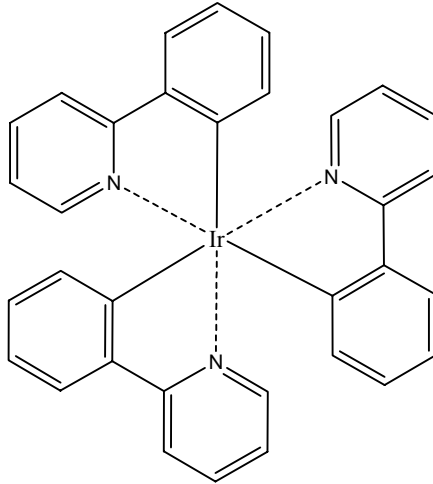


Figure 1-24. Structure of Ir(ppy)₃.

OLED and PLED Structure

The basic structure of a typical dc-biased OLED is shown in Figure 1-25. The first layer above the glass substrate is a transparent conducting anode, typically indium tin oxide (ITO). The next layer is usually the hole transport layer. This layer is usually a good hole transport material, and for most devices is some type of starburst amine or poly(3,4-ethylenedioxy-2,4-thiophene)-polystyrene sulfonate (PEDOT-PSS).^[79]

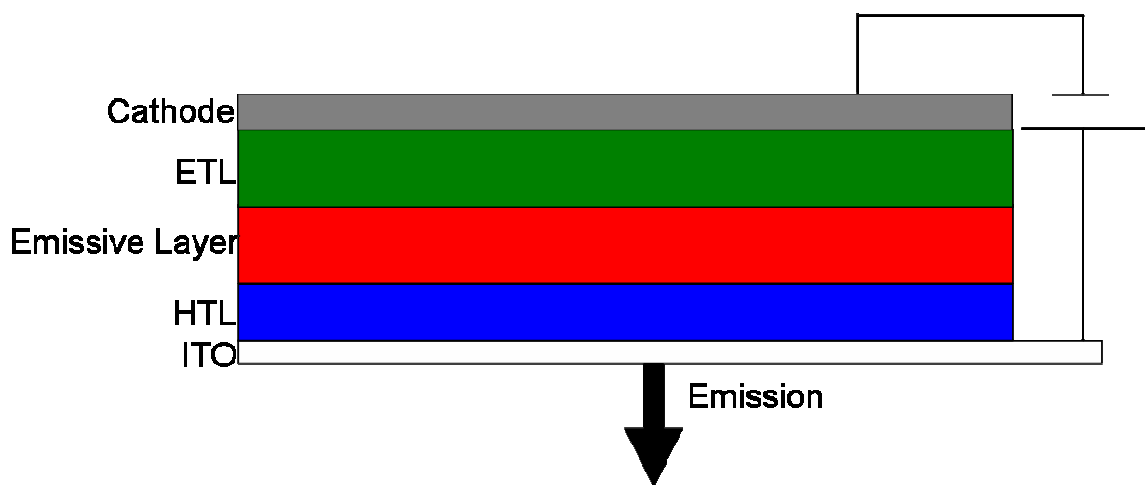


Figure 1-25. Schematic of light emitting diode, showing each individual layer.

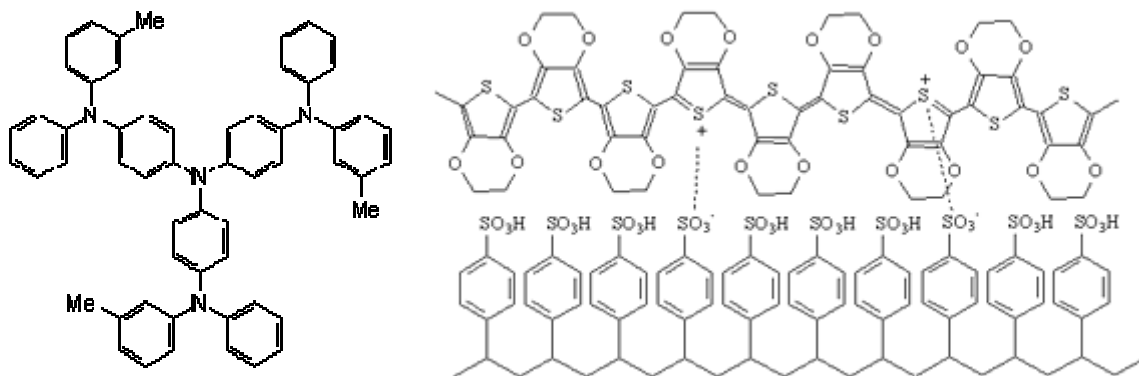


Figure 1-26. Structures of typical hole transport materials (a) NPD (b) PEDOT-PSS.

The next layer is the emitting layer. This layer is thermally evaporated or spin coated onto the hole transport layer. This layer is typically on the order of 100 nm thick. The next layer is the electron transport layer. This layer usually consists of an organic material, thermally evaporated, which possesses great electron mobility and also works well at blocking holes from reaching the cathode, therefore confining the carriers to the emitting layer. This material typically consists of aluminum *tris*-quinolate or an oxadiazole containing complex.^[80-86] The next layer is the cathode. This usually consists of a low workfunction (ϕ) metal such as Ca ($\phi = 2.87$ eV) deposited by thermal evaporation. A protective layer of aluminum is often deposited on top of the calcium layer to prevent oxidation.

Carrier Transport

The thin films used in organic or polymer light emitting diodes are typically amorphous. The amorphous structure leads to a reduction in quenching from internal conversion processes present in crystalline materials, due to the limit of phonon interactions, and therefore leads to a consequent increase in the radiative recombination of Frenkel type excitons.^[11] The efficient generation of excitons is strongly dependent on charge carrier injection and transport through the organic layers.

Due to the weak intermolecular coupling and the high disorder of amorphous materials, their measured carrier mobilities are dramatically lower than in most crystalline solids. Therefore, the conduction mechanism is usually not considered Ohmic in nature, but is often space charge limited, influenced by the presence of traps, or hopping.^[87] For example, carrier trapping in diamines has a negligible effect on its conduction properties, and the hole mobilities in these materials are of the order of $10^{-3} \text{ cm}^2/\text{V s}$.^[88] In electron transporting materials such as Alq₃, however, the trap density is much higher, which significantly lowers the carrier mobility.^[89] The electron mobility of Alq₃ is $10^{-4} \text{ cm}^2 / \text{V s}$ at an applied voltage of 10^6 V/cm , with hole mobilities at least two orders of magnitude lower.^[90] The carrier mobility of most organic materials is found to be dependent on both the electric field (E) and the temperature (T) according to^[91]

$$\mu(E, T) = \mu_0 e \left(-\frac{E_0}{kT_{\text{eff}}} \right) e \left(\frac{\beta E^{\frac{1}{2}}}{kT_{\text{eff}}} \right) \approx \mu_0^* e \left(\alpha E^{\frac{1}{2}} \right) \quad (0.15)$$

where k is the Boltzmann constant, $E_0 = kT_0$ is the activation energy at zero electric field corresponding to temperature T_0 , μ_0 and μ_0^* are the zero field carrier mobilities, $1/T_{\text{eff}} = 1/T - 1/T_0$, and β and α are constants.

The difference between the cathode (anode) Fermi level and the LUMO (HOMO) of the electron (hole) transport layer forms a barrier to injection of electrons (holes) into the active layer. For devices with a barrier larger than 0.4 eV, the current flow is primarily determined by the efficiency of carrier injection at the contacts.^[91] This is typically described as the injection-limited regime. The energy level offset at the

organic-electrode interface can be tailored by choosing an electrode with a work function corresponding to the energy levels at each layer.

In organic molecular light emitting diodes, three different conduction mechanisms are commonly observed: ohmic, space-charge limited (SLC) conduction, and trapped carrier limited (TCL) space charge conduction. Ohmic conduction is seen at low voltages when the density of injected carriers, n_{inj} , is smaller than the thermally generated background free charge density, n_0 . In this regime, the current density is given by Ohm's law:

$$J = q\mu_n n_0 V / d \quad (0.16)$$

where q is the electronic charge, μ_n is the hole or electron mobility, V is the applied voltage, and d is the layer thickness. Space charge limited conduction is observed when $n_{inj} > n_0$ when charge trapping is not observed. The current density is then described by Child's law:

$$J = (9/8)q\mu_n \varepsilon \frac{V^2}{d^3} \quad (0.17)$$

where ε is the dielectric permittivity.^[92]

The presence of ohmic and space charge limited conductivity is observed in the low-voltage operation of devices. At higher voltages, traps located near the LUMO tend to fill. If there exists a high density of traps, their concentration and energy distribution governs the current, resulting in the trapped charge limited (TCL) space charge conduction regime. As the traps fill, they reduce the density of empty traps and an increase in electron mobility ensues. An analytical expression relating the current to the voltage in the TCL regime is given for a continuous energy distribution of traps $N_t(E)$ below the LUMO, as given by^[92]

$$N_t(E) = \left(\frac{N_t}{kT_t} \right) e^{\left(\frac{E - E_{LUMO}}{kT_t} \right)} \quad (0.18)$$

where E_{LUMO} is the LUMO energy, N_t is the total trap density, k is the Boltzmann constant, and $T_t = E_t/k$, where E_t is the characteristic trap energy. The current density is then given by

$$J_{TCL} = N_{LUMO} \mu_n q^{(1-m)} \left[\frac{\varepsilon m}{N_t(m+1)} \right]^m \left(\frac{2m+1}{m+1} \right)^{(m+1)} \frac{V^{(m+1)}}{d^{(2m+1)}} \quad (0.19)$$

where N_{LUMO} is the density of states (DOS) in the LUMO band, $m = T_t/T$, and $\mu = \mu(E)$. From this equation, it can be seen that trap limited conduction results in a power-law dependence of current on voltage.

Device Efficiency

Efficiency of devices is an important issue not only for energy consumption, but also for its effect on the longevity of the devices. This effect on longevity is due to the minimization of ohmic heating that can be achieved by operation at lower voltages. Devices with high power efficiency imply a low current-voltage product for a given luminance. Power efficiency is only one of the ways to determine device efficiency. The most commonly reported efficiency from the literature is based on external quantum efficiency. External quantum efficiency is the measure of photons produced per electrons injected.^[93] One of the forms in which the basic equation for the external quantum efficiency η_{ext} of the device can be written as

$$\eta_{ext} = \xi \gamma r_{ST} \phi_{PL} \quad (0.20)$$

where ξ is the fraction of photons collected normal to the front surface of the device, γ is measure of the hole and electron recombination, r_{ST} is the ratio of singlet to triplet

excitons formed in the material, and ϕ_{PL} is the solid state photoluminescence quantum efficiency. It can be shown that for devices with a large refractive index:^[93]

$$\xi \approx \frac{0.5}{n^2} \quad (0.21)$$

where n is the refractive index of the medium. For devices with equal charge carrier balance the factor γ equals one, but this is rarely the case with organic materials. The value for r_{ST} is, according to spin statistics, 0.25, but recently there has been some evidence that this is not always the case.^[94-98] While the photoluminescence quantum efficiency can approach unity for many organic dyes, the efficiency in the solid state is typically much lower. This is due to “concentration quenching”, which is an effect due to the creation of nonradiative pathways.^[99-104] Given all of these conditions, devices which show only fluorescence have a upper level of efficiency approaching 15% of the solid state photoluminescence efficiency.

Device Failure Mechanisms

The overall stability of light emitting diodes is an important element in understanding their commercial impact. The degradation of an OLED and PLED during operation appears in four modes:^[105] (1) decay in emission intensity, (2) a voltage increase in the constant current mode, (3) the growth of nonemissive areas in the device, and (4) the eventual electrical short circuit.

One of the most evident mechanisms for the degradation of OLEDs is through the formation of nonemissive “dark” spots which in turn leads to a long term decrease in efficiency. These spots result from the delamination of the metal at the metal/organic interface due to a large amount of Joule heating.^[106] This tends to lead to a short-circuit

condition and carbonization of the active layer. This may also lead to electrode migration in these areas where the conductivity is high.^[107]

The most prevalent mechanism for decay in PLEDs is photooxidation during device operation.^[108, 109] The extended conjugation length of polymers tends to increase the electron density at the double bond making it more reactive to the electrophilic singlet oxygen. Carbonyl formation by the reaction of oxygen with alkoxy centers is also a facile method for the quenching of electroluminescence due to the fact that carbonyls are typically good nonradiative quenching centers. The source of the singlet oxygen is energy transfer from the polymer to molecular oxygen.

The primary degradation method in organic light emitting diodes is recrystallization. Excitons are rapidly quenched by defects and charge-dipole induced fields at the surface of a grain boundary. Any given amorphous layer will recrystallize slowly as its temperature rises towards its glass transition temperature.

The final mechanism, shared by both OLEDs and PLEDs is the electrical breakdown of the device caused by pinhole electrical arcs.^[110] These breakdowns occur usually at high voltage. The mechanism is the circuit opens around the pinhole which in turn stops the arcing. The resultant hole allows for moisture and air to enter the device and delaminate the material. When the number of burn-outs becomes too numerous, the circuit eventually shorts out and destroys the device.

Literature Review

The field of organic and polymer light emitting diodes has exploded in the latter part of the 20th century and has continued to expand into the present. Most of the focus has been on polymers and organic molecules which emit in the blue region of the electromagnetic spectrum. This focus on this region is due to the poor efficiency and

color saturation of organic systems and molecules which emit in the blue. This is unlike molecules which emit in the green and red, which have been designed with high efficiencies and exhibit adequate color saturation. Recently, there are several displays based on polymer and organic systems which are commercially available.^[111, 112]

The research carried out here at the University of Florida, focuses on the emission of organic and polymer systems which emit in the near-infrared. This can be accomplished by three means. The first involves organic molecules and polymers which exhibit a small HOMO-LUMO gap, which permits emission in the near-infrared. Although this is possible, the efficiency of fluorescence and device performance is severely limited by nonradiative decay processes. The second means for producing emission in the near-infrared is the use of organo-transition metal or organo-lanthanide complexes. The third means for the creation of near-infrared (NIR) emission is the use of organic functionalized semiconductor nanoparticles. In this section, a brief history of each of the possible directions is provided.

Organic Systems

There are several examples of groups obtaining near-infrared electroluminescence from organic and polymeric materials. The majority of this emission although is located in the visible, with emission carrying over into the NIR. The Holmes group, in 1995, showed near-infrared emission from a 2,5-bis(hexyloxy)terephthalaldehyde-3-dodecyl-2,5-thiophenediacetonitrile copolymer which showed broad emission extending out to 1000 nm, with an internal quantum efficiency of 0.2% photons/electron.^[113] Fujii, in 1997, fabricated devices showing emission tailing out to 1000 nm with phthalocyanine co-evaporated with DCM (4-(dicyanomethylene)-2-methyl-6-(p-dimethylaminostyryl)-4H-pyran), which showed efficient emission operating at 15 V.^[114] In 2000, Suzuki

showed emission from an organic ionic dye, 2-[6-(4-dimethylaminophenyl)-2,4-neopentylene-1,3,5-hexatrienyl]-3-methylbenzothiazolium perchlorate blended into poly(N-vinylcarbazole). These devices showed that the emission improved over time due to the alignment of the ionic dye molecules along the bias field, with the external efficiency eventually reaching 1%.^[115] Maltsev, in 2002, showed very narrow emission at 850 nm resulting from the electroluminescence of J-aggregates of cyanine dyes blended into a polyimide matrix.^[116] The Bazan group showed efficient electroluminescence ($\phi_{\text{ext}} = 0.1 - 0.3$ % photons/electron) of ethynyl linked porphyrin complexes, in 2003. These complexes show emission typical of porphyrins with a tail into the near-infrared.^[117] In 2004, Suzuki again produced devices with emission into the NIR, using organic ionic dyes. He used (2-[6-(4-dimethylaminophenyl)-2,4-neopentylene-1,3,5-hexatrienyl]-3-methyl-benzothiazonium perchlorate) (LDS821) and $[\text{C}_{41}\text{H}_{33}\text{Cl}_2\text{N}_2](+)\cdot\text{BF}_4^-$ (IR1051) to produce emission at 800 and 1100 nm, respectively.^[118] This year, Yang created devices from alkyl-substituted fluorene, 4,7-diselenophen-2'-yl-2,1,3-benzothiadiazole (SeBT), and 4,7-diselenophen-2'-yl-2,1,3-benzoselenadiazole (SeBSe), which showed emission in the 670 – 790 range. These devices showed external efficiencies ranging from 0.3 to 1.1%.^[119] Most recently, Thompson *et al* showed NIR emission peaking at 800 nm from a donor-acceptor copolymer of 1,4-(2,5-dihexadecyloxyphenylene) and 5,8-linked 2,3-diphenylpyrido[3,4]pyrazine.^[120]

Inorganic Nanoparticles

The use of solution processible semiconductor nanoparticles (quantum dots, QD) for electroluminescent emission in the near-infrared is a fairly recent process. These

devices are based on II-VI and IV-VI semiconductor nanoparticles blended into conductive polymer matrixes. The use of QDs for electroluminescent devices is an interesting concept due to the tunability of emission created by quantum confinement. As the nanoparticle is decreased in size, the band gap increases; therefore causing a hypsochromic shift in the emission. The QDs are made solution processible by the functionalization of the surface with organic ligands.

In 2003, Steckel showed tunable electroluminescent emission using PbS nanoparticles, with emission ranging from 1.3 – 1.6 μm , dependent on particle size.^[121] Bakeeva then increased the emission range from 1.1 to 1.6 μm by changing the organic molecule bound to the surface from oleate ligands to octadecylamine ligands. These devices showed an internal efficiency reaching 3%.^[122] Most recently, Sargent fabricated devices containing PbSe which showed tunable emission in the near-infrared.^[123] Progress in the field of nanoparticle based light emitting diodes was further advanced in 2004 by the production of HgTe based devices, which showed efficient emission and broad tunability.^[124]

Inorganic nanoparticles are extremely versatile due to the large tunability of the energy gap. Efficiency is also enhanced due to limited phonon interactions in nanoparticles, which allows for less nonradiative decay from the excited state. Nanoparticles also have severe limitations. The first limitation is that nanoparticles tend to aggregate in solution and disperse poorly in thin films. The second major limitation is the fact that nanoparticles tend to oxidize due to the abundance of non-bonded atoms on the surface.

Organo-Lanthanide and Organo-Transition Metal Complexes

The use of lanthanide and transition metal complexes is by far the most common method for emission in the near-infrared. The field of organic lanthanide metal complexes was born in the late 1950s and continued throughout the 1960s with research devoted to lanthanide beta-diketonates.^[125-133] Research then turned to lanthanide polypyridyl complexes.^[131, 134-136] In the 1970s much of the research into lanthanide organic complexes shifted to porphyrins.^[45, 46, 53, 64, 137-144] Since then, most of the research is into trying to improve the efficiency of the lanthanide emission.^[145-154]

The use of lanthanide organic complexes for electroluminescence was unknown until 1999, when Curry observed electroluminescence from *tris*-quinolato erbium(III) (ErQ₃). This complex showed the typical $^4I_{13/2} \rightarrow ^4I_{15/2}$ emission centered at 1.54 μm .^[155] Since then a great deal of research has been focused on ErQ₃ due to its potential use in optical communications.^[156-159] Near-infrared emission has also been seen for other lanthanide quinolate complexes. Kawamura in 2000, observed typical $^2F_{5/2} \rightarrow ^2F_{7/2}$ emission from Yb³⁺ *tris*-quinolate at 985 nm operating at 15V.^[160, 161] Several groups also observed near-infrared emission from Nd³⁺ *tris*-quinolate based devices, showing emission at 800, 1060, and 1300 nm.^[157, 159, 162-164] Since then the focus of rare-earth quinolate complexes has been on the effect of structure on the emissive properties. It was determined that functionalization of the quinolate complex with halogens has a dramatic improvement in the emission yield.^[165, 166]

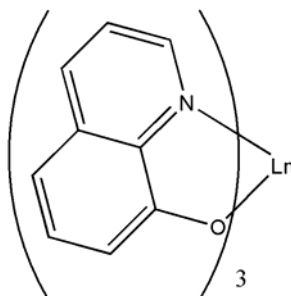


Figure 1-27. Structure of Lanthanide *tris*-quinolate.

Lanthanide quinolate complexes, although functional, are not the only means of sensitizing near-infrared emission of lanthanide ions. Near-infrared emission has also been observed for complexes of lanthanide diketonates. In 2001, Hong produced devices with $\text{Pr}(\text{DBM})_3\text{Bath}$ and $\text{Yb}(\text{DBM})_3\text{Bath}$ (see Figure 1-28), which showed the $^1\text{D}_2 \rightarrow ^3\text{F}_2$ (890 nm), $^1\text{D}_2 \rightarrow ^3\text{F}_3$ (1015 nm), $^1\text{D}_2 \rightarrow ^3\text{F}_4$ (1065 nm), and $^1\text{D}_2 \rightarrow ^1\text{G}_4$ (1550 nm) for Pr^{3+} and $^2\text{F}_{5/2} \rightarrow ^2\text{F}_{7/2}$ emission from Yb^{3+} respectively.^[167, 168] Harrison, later reported in 2003, emission from the $\text{Er}^{3+} \ ^4\text{I}_{13/2} \rightarrow ^4\text{I}_{15/2}$ (1520 nm) and $\text{Nd}^{3+} \ ^4\text{F}_{3/2} \rightarrow ^4\text{I}_{11/2}$ (880 nm), $^4\text{F}_{3/2} \rightarrow ^4\text{I}_{13/2}$ (1060 nm), $^4\text{F}_{3/2} \rightarrow ^4\text{I}_{15/2}$ (1330 nm) complexes of DBM.^[169] Previously unseen, in organic systems, transitions for Ho^{3+} , $^5\text{F}_5 \rightarrow ^5\text{I}_6$ (1500 nm), $^5\text{F}_5 \rightarrow ^5\text{I}_7$ (1200 nm), $^5\text{F}_5 \rightarrow ^5\text{I}_8$ (980 nm) and Tm^{3+} , $^3\text{F}_4 \rightarrow ^3\text{H}_4$ (1400 nm), $^3\text{F}_4 \rightarrow ^3\text{H}_6$ (800 nm) were finally observed in 2004 in DBM systems.^[170, 171]

The use of other molecular systems to produce near-infrared emission has been achieved. For example, Sloof in 2001, produced typical Nd^{3+} emission from a lissamine dye functionalized terphenyl based metal complex. They determined that a larger conversion to the triplet state under electrical excitation, resulting in a more efficient Nd^{3+} emission.^[172] Previous work in our group by Harrison *et al.* has produced NIR emission from lanthanide porphyrin complexes.^[173-177] It was determined that, the porphyrin efficiently transferred its energy to the lanthanide, producing the characteristic

metal emission. Emission from Nd^{3+} , Yb^{3+} , Ho^{3+} , and Er^{3+} were observed. They also determined that the change of axial coordination ligand has little effect on the electroluminescence efficiency. Recently dendrimer complexes with a lanthanide core were fabricated and showed efficient near-infrared emission.^[178] The core of the dendrimer was a nona-coordinated Er^{3+} atom with keto functionalized metalloporphyrin dendrons. Excitation of the porphyrin dendron resulted in the typical lanthanide emission.

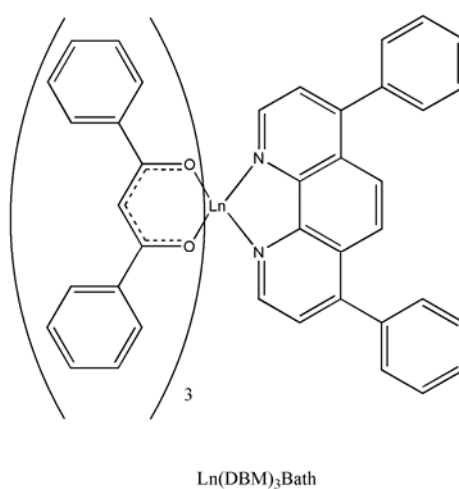


Figure 1-28. Structure of Lanthanide tris-DBM bathophenthroline complex.

CHAPTER 2 SUBSTITUTED PORPHYRIN COMPLEXES

This chapter discusses the results of the study of substituted lanthanide porphyrin complexes. Previous work by Harrison *et al* showed that, although the porphyrin ligand is useful in sensitizing the emission of lanthanides in light emitting diodes, its electronic properties are not ideal for highly efficient devices. This study was undertaken to further investigate the electronic properties of the porphyrin macrocycle, as well as to enhance the performance of devices created using lanthanide substituted porphyrin complexes. In order to accomplish this, several porphyrins were synthesized by Alison Knefely, according to the procedure described in chapter one, with substitutions of the meso phenyl group in an effort to vary the electronic properties of the complexes. Bulky groups were appended to the phenyl groups to understand the effect of aggregation in the devices. The axial ligand was also substituted. The structures of the resulting complexes are shown in Figure 2-1.

The first complex studied was (quinolinato)(5,10,15,20-tetraphenylporphyrinato)Yb(III) (Yb(TPP)Q). The hydroxyquinoline ligand was used as the axial ligand in an effort to increase the electron accepting nature of the complex due to the electron poor unsaturated nitrogen. This complex (see Figure 2-2) was also used because it closely resembled previously studied complexes.^[169] The second complex studied was (hydridotris(1-pyrazolyl)borato)(5,10,15,20-tetrakis(3,4,5-trimethoxyphenyl)porphyrinato)Yb(III) (Yb(TMPP)TP). The substitution of the electron donating alkoxy groups was chosen in an effort to perturb the overall electronic structure

of the complex. It was expected that the hole mobility for devices fabricated using this complex would be higher. The third complex studied was (cyclopentadienyl)tris(diethylphosphinito)cobaltate(5,10,15,20-tetra(4-pyridyl)porphyrinato)Yb(III) (Yb(TPyP)L(OEt)₃). The substitution of the phenyl groups for pyridyl groups was an effort to increase the electron transporting properties of the complex due to the presence of electron poor pyridine substituents. The use of the Klaui (L(OEt)₃) ligand was motivated by the fact that the analogous complex with the TP capping ligand was insoluble in all common organic solvents, and the Klaui ligand improved the solubility. It has been shown that the Klaui ligand has little effect on the overall properties of the complexes.^[169] The final complex studied was (hydridotris(1-pyrazolyl)borato)(5,10,15,20-tetra(4(2'-ethylhexyloxy)porphyrinato)Yb(III) (Yb(TPP_OEH)TP). It was expected that the long branched alkoxy side-chain would reduce aggregation due to the inability of complexes to approach each other. The photophysical, electrochemical, and device performance characteristics of these complexes are discussed in this chapter.

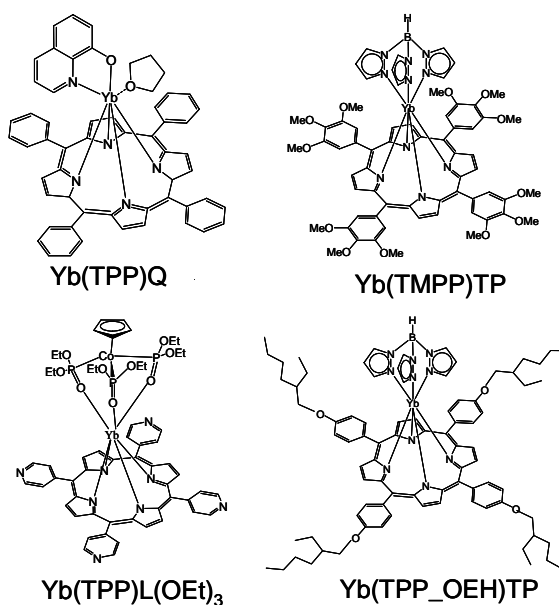


Figure 2-1. Yb porphyrin complexes used in study.

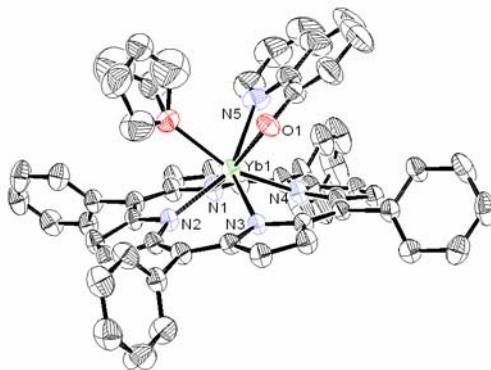


Figure 2-2. X-ray crystal structure of Yb(TPP)Q showing coordination of a molecule of THF.

Solution Photophysics

Absorption

All absorption measurements were made with the complexes as dilute solutions in methylene chloride (CH_2Cl_2) unless otherwise indicated. Figure 2-3 shows the absorption spectra for the studied ytterbium porphyrin complexes. The absorption spectra are dominated by the $\pi \rightarrow \pi^*$ transitions of the porphyrin ligand, including the Soret ($S_0 \rightarrow S_2$) band (~ 420 nm) and the weaker Q-bands ($S_0 \rightarrow S_1$) ($\sim 500 - 600$ nm). No absorption for the $4f \rightarrow 4f$ transitions could be seen due to their low molar absorptivities ($\sim 1-10 \text{ M}^{-1}\text{cm}^{-1}$) Furthermore, little evidence for absorption by the capping ligand was observed in the samples studied. The Soret band showed a bathochromic shift upon coordination to the lanthanide, from 412 nm in the free base to ~ 427 nm in the complex. Overall, the absorption spectrum resembles a “normal” metalloporphyrin absorption spectrum such as Ni(TPP).^[37] These results correlate with previously studied unsubstituted Ln(TPP)L complexes.^[169] Although the location of the absorption peaks of each complex is slightly different, there is little evidence to suggest that changes to the porphyrin periphery has a dramatic effect on the electronic properties

of the ligand. This suggests that there is little perturbation of the π -electronic system due to substitution upon the porphyrin ring. There exists some perturbation to the system by the introduction of the quinolate capping ligand. The Soret band blue-shifts with respect to other Yb(TPP) complexes, showing that the basic ligand has some effect on the overall electronic properties of the complex.

Table 2-1. Photophysical properties of Yb porphyrin complexes measured in CH₂Cl₂.

Complex	$\lambda_{\text{abs}} / \text{nm (Log } \epsilon)$	$\lambda_{\text{em}} / \text{nm}$
Yb(TPP)Q	375(4.12), 420(5.61), 516(3.48), 553(4.30), 591(3.68), 626(2.97)	600, 650, 715, 913, 927, 954, 980, 1005, 1025, 1047,
Yb(TMPP)TP	378(4.03), 404s(4.72), 428(5.75), 516(3.50), 554(4.30), 592(3.57), 630(2.97)	610, 650, 715, 925, 952, 978, 1003, 1029, 1049
Yb(TPyP)L(OEt)₃	403s(4.65), 427(5.76), 519(3.68), 558(4.44), 597(3.71), 626(2.92)	605, 645, 715, 923, 950, 985, 1005, 1018, 1048
Yb(TPP_OEH)TP	378(3.92), 404s(4.61), 427(5.64), 517(3.39), 553(4.18), 592(3.45), 627(2.86)	605, 650, 715, 927, 951, 974, 1003, 1020, 1050

Emission

Excitation of the Yb porphyrin complexes into the Soret or Q-bands resulted in both visible (Figure 2-4) and near-infrared emission (Figure 2-6). In the visible region from 600 – 750 nm, there are three emission bands. The weak visible fluorescence at ~650 and ~715 nm matches the visible fluorescence of free-base tetraphenylporphyrin.^[179] These assignments agree with previous studies of Ln(TPP)L, which came to a similar assignment partly due to the short (8 ns) lifetime of the 650 and 710 nm bands.^[169] A weak emission band at ~600 nm was observed in all of the Yb porphyrin complexes. The excitation spectrum of all three emission bands helps to elucidate the origin of each emission transition. The excitation spectra of the three emission peaks for the Yb porphyrin complexes are shown in Figure 2-5. Comparison of the Soret bands observed in the excitation spectra show that the 610 nm emissions are bathochromically shifted ~15 nm from the excitation spectra of the other emission bands.

This is similar to the UV-Vis absorption band shift which occurs when the porphyrin is coordinated to Ytterbium. Thus the visible emission bands at 654 and 720 nm can be attributed to “free” porphyrin emission which seems not to be influenced by the metal, while the 610 nm band corresponds to emission from the lanthanide metalloporphyrin complex. All of the structures show an excitation peak around 450 nm ($\lambda_{em} = 715$), which suggest that there exists the possibility of a more complex structure involved in the emission, such as an aggregate. This all leads to the conclusion that there is the presence of a free base impurity, which leads to less desirable features in the near-infrared.

The near-infrared photoluminescence properties of the substituted ytterbium porphyrins are different and vary dramatically, in contrast to the absorption spectra, which are similar for all of the complexes. Figure 2-6 shows the near-infrared emission of the substituted Yb^{3+} porphyrin complexes. The near-infrared region consists of a sharp peak at ~ 980 with additional broad bands on each side of the sharp peak. The structure of the spectra has been attributed to crystal field splitting effects which are calculated to be on the order of hundreds of cm^{-1} .^[125]

Previous work with Yb porphyrins suggests that the ${}^2\text{F}_{5/2} \rightarrow {}^2\text{F}_{7/2}$ emission transition is composed of eight different peaks.^[169] Through curve fitting using the commercially available program Origin[®], the crystal field induced emission structure was estimated. For $\text{Yb}(\text{TPP})\text{Q}$ seven peaks could be ascertained, and for all of the other complexes there were six peaks that could be determined with confidence. All of these peaks show evidence of a crystal field splitting of $\sim 500 \text{ cm}^{-1}$ which agrees well with previous results.^[169] Variable temperature work by others has shown that higher crystal field states can be thermally populated when the excited state possesses a long

lifetime.^[180, 181] This agrees well with variable temperature photoluminescence studies carried out on the porphyrin complexes. As an example Figure 2-7 shows 80 K and RT emission spectra for the complexes, which clearly shows the high energy emission band.

The use of different solvents can play a significant role in the optical properties of organic compounds. Therefore the solvent effects on the absorption and emission properties of the Yb³⁺ porphyrin complexes were examined. The changes in absorption properties for all complexes were similar in various solvents. The Soret band shows a slight bathochromic shift when placed in increasing polar solvents.

While the absorbance of Yb(TPP)Q varies by a few nanometers in different solvents, the solvent used has a more significant effect on the NIR photoluminescence quantum yield. The effect of solvents on the quantum yields of the other Yb porphyrin complexes was less important. In general, the quantum yields are low (<10%) due to non-radiative pathways of deactivating the excited state. Table 2-2 shows the NIR quantum yields of the Yb porphyrin complexes in different solvents. Since the lanthanide is positioned above the plane of the porphyrin ring (see figure 2-2), there remain several coordination sites where a solvent molecule can access the metal ion. Yb(TPP)Q has a relatively small axial ligand which may allow for trace amounts of water present in the solvent or the solvent itself, to coordinate to the metal, which in turn lowers the radiative quantum yield. The coordination of water to lanthanide metal centers is known to play a significant role in deactivating the excited state of the lanthanide ion by coupling to the non-radiative O-H vibrational modes. However, in coordinating solvents, the solvent displaces the coordinated water thus removing the O-H oscillators from the proximity of the metal ion, which in turn lowers the non-radiative rate.

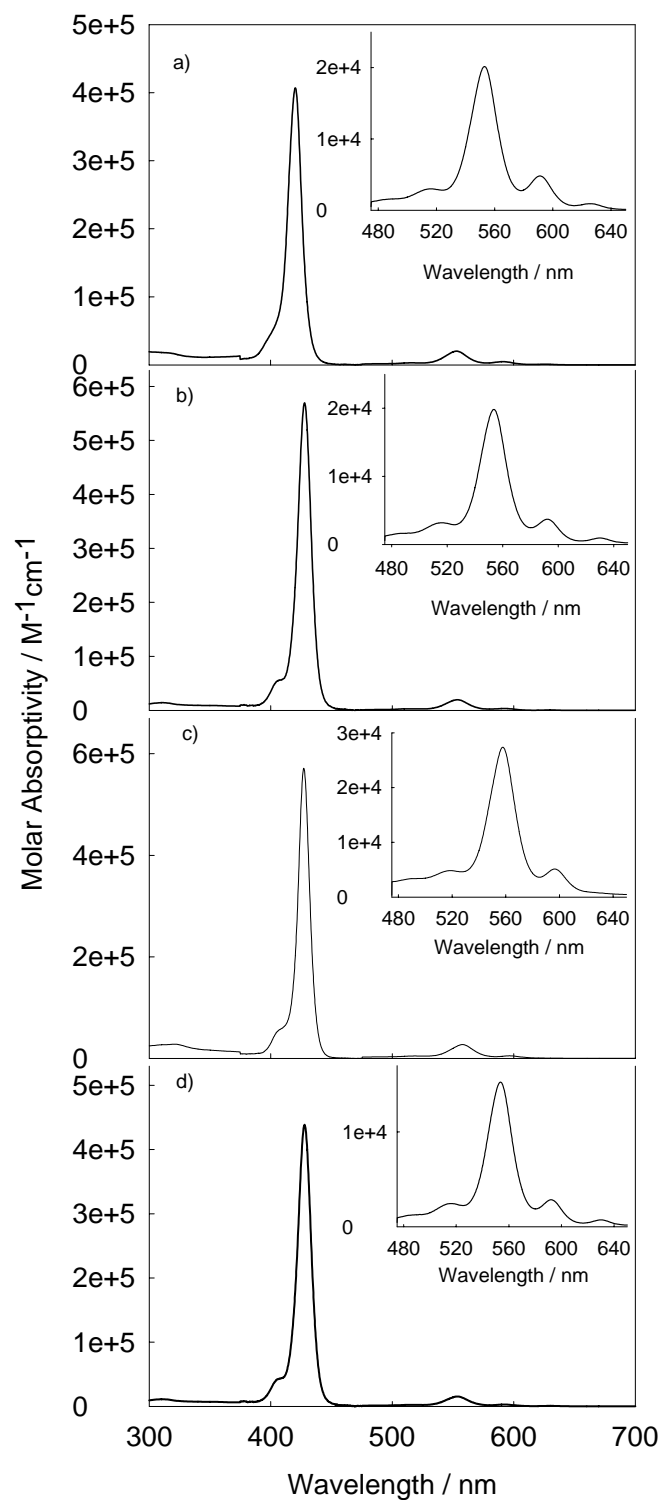


Figure 2-3. Absorption spectra for a) Yb(TPP)Q, b) Yb(TMPP)TP, c) Yb(TPyP)L(OEt)₃, d) Yb(TPP_OEH)TP in CH₂Cl₂ as a function of molar absorptivity.

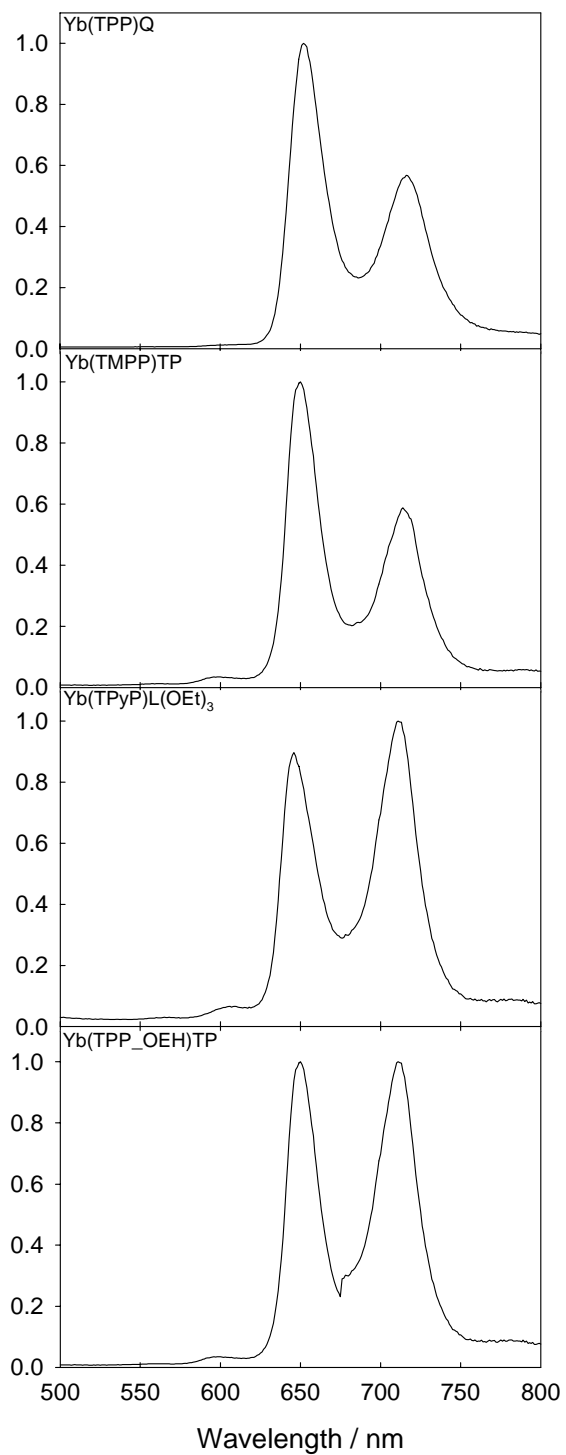


Figure 2-4. Visible emission spectra for substituted Yb³⁺ complexes in CH₂Cl₂ at room temperature ($\lambda_{\text{ex}} = 420$ nm).

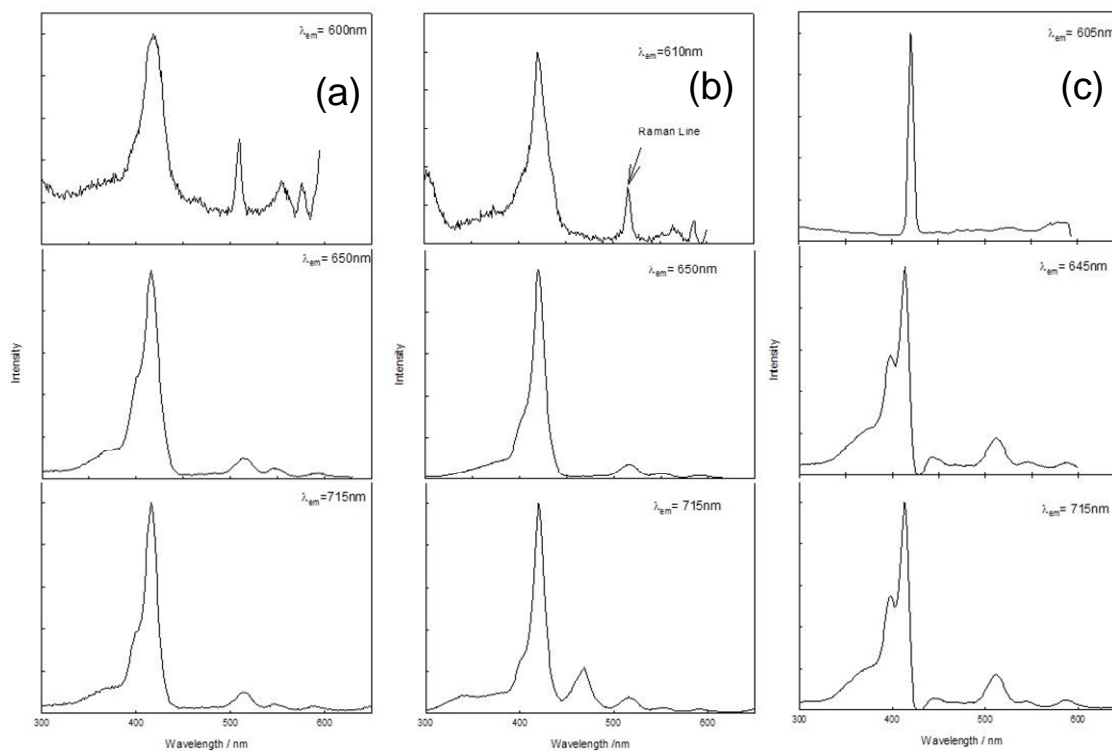


Figure 2-5. Excitation spectra of (a) Yb(TPP)Q, (b) Yb(TMPP)TP, and (c) Yb(TPyP)L(OEt)₃.

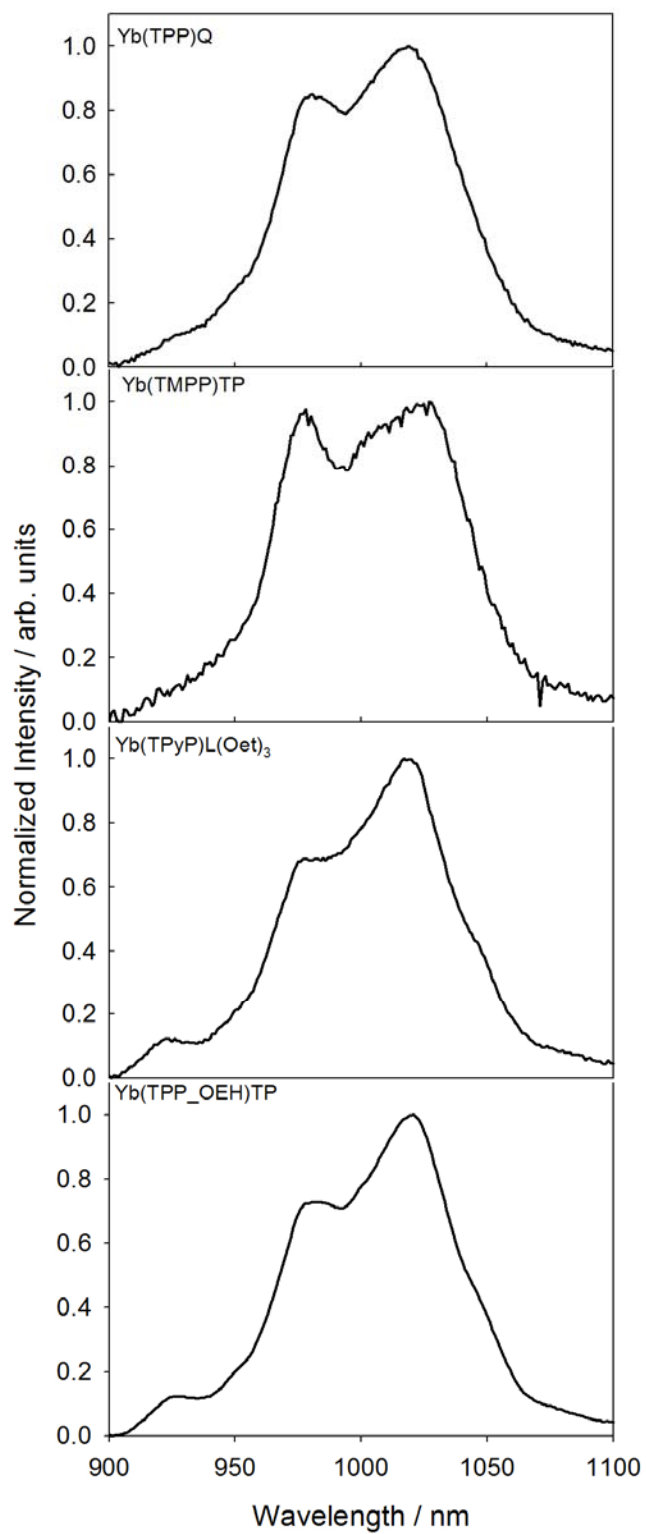


Figure 2-6. Near-infrared emission spectra for substituted Yb³⁺ porphyrin complexes in CH₂Cl₂ at room temperature ($\lambda_{\text{ex}} = 420$ nm).

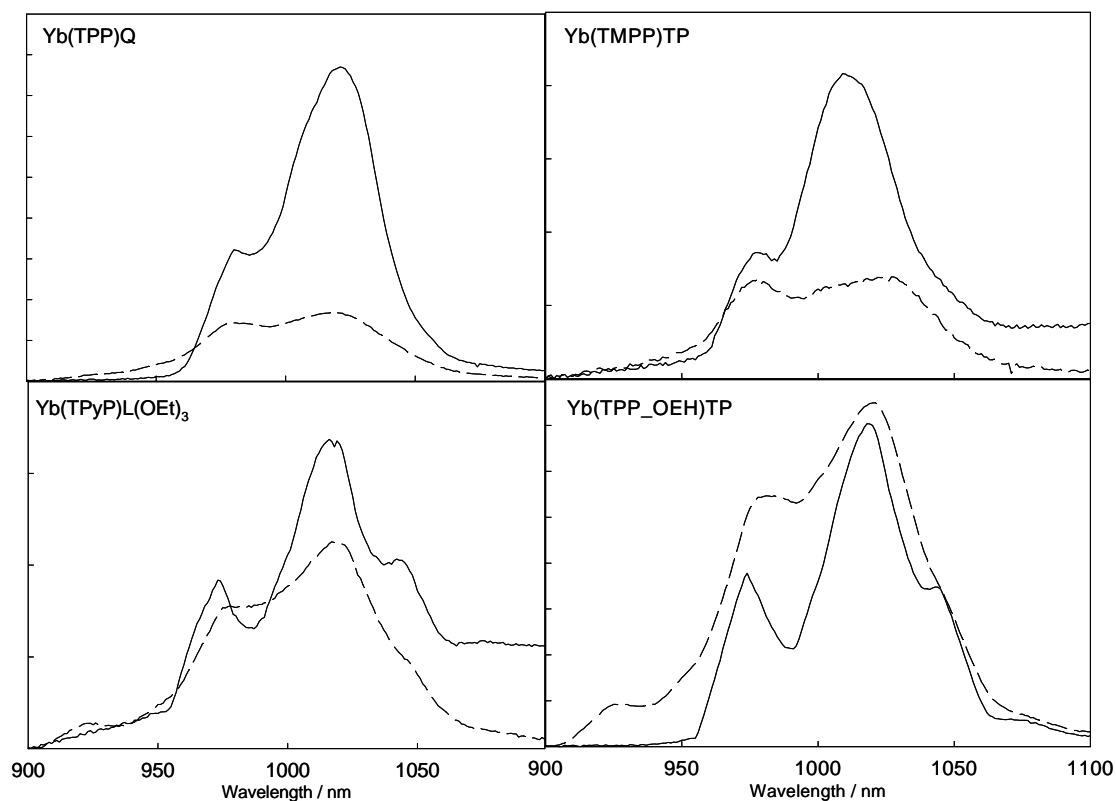


Figure 2-7. Near-infrared emission spectra for substituted porphyrin complexes in 2Me-THF($\lambda_{\text{ex}} = 420 \text{ nm}$) (— 80 K, --- 300 K).

Table 2-2. Solvent effects on the near-infrared quantum yields of Yb porphyrin complexes.

Solvent	Yb(TPP)Q Φ_{PL}	Yb(TMPP)TP Φ_{PL}	Yb(TPyP)L(OEt) ₃ Φ_{PL}	Yb(TPP_OEH)TP Φ_{PL}
CH₂Cl₂	0.0091	0.041	0.031	0.034
Toluene	0.0081	0.037	0.039	0.047
THF	0.0085	0.028	0.027	0.036
DMSO	0.029	0.031	0.032	---
CH₃CN	0.0097	0.026	---	---
Hexane	---	---	---	0.057

The presence of high energy oscillators within close proximity of the lanthanide ion will increase the non-radiative decay rates of the lanthanide excited states. By understanding the Energy Gap Law and using Siebrand's approach, the non-radiative rate can be found using Equation 2.1.^[182]

$$k_{nr} = \left(\frac{2\pi\rho_{nr}}{h} \right) N_{\rho} J^2 \left(\frac{M_{\rho}\omega_{\rho}}{2h} \right) F_{\rho} \quad (2.1)$$

In Equation 2.1, ρ_{nr} is the density of final vibrational states, J is the electronic coupling constant due to nuclear motion, $\frac{M_{\rho}\omega_{\rho}}{2h}$ measures the coupling to the vibrational modes, N_{ρ} is the number of modes and F_{ρ} is the Franck-Condon factor. The Franck-Condon factor can be described by Equation 2.2.

$$F_{\rho} = \frac{\exp(-\frac{1}{2}k\Delta^2) (\frac{1}{2}k\Delta^2)^{\nu}}{\nu!} \quad (2.2)$$

In Equation 2.2, k is a constant, Δ is the difference in positions of the final and initial vibrational states and ν is composed of the energy between the two states, ΔE_0 and the maximum oscillator of highest energy, ω_{\max} as shown in Equation 2.3.

$$\nu = \frac{\Delta E_0}{2h\omega_{\max}} - 1 \quad (2.3)$$

Using Sterling's approximation to expand the factorial in Equation 2.2 and the approximations for energy gaps of lanthanides corresponding to 1 to 3 vibrational quanta of the host, the non-radiative decay rate can be simplified to Equation 2.4.

$$k_{nr} = \beta \exp[-(\Delta E_0 - 2h\omega_{\max})\alpha] \quad (2.4)$$

The α and β terms vary very little between hosts. Therefore, as the radiative energy gap decreases, the non-radiative decay rate increases exponentially. Given the ${}^2F_{5/2} \rightarrow {}^2F_{7/2}$ transition is $\sim 10,000 \text{ cm}^{-1}$, it is evident that the use of C-H oscillators ($\sim 3200 \text{ cm}^{-1}$) plays a significant role in the deactivation of the lanthanide excited state.

Light Emitting Devices

Light emitting diodes used in this study were of the modified single emissive layer type, that is, there was no true electron transport layer. These devices were prepared by spin coating a thin layer of PEDOT-PSS (Bayer Baytron P VP 4083) onto cleaned ITO. The device was then dried in vacuo for 4 hours at 150° C in order to remove any residual solvent. The active layer was spin-coated and the device was placed in high vacuum (10^{-6} torr) for several hours, again to remove residual solvent. Calcium and aluminum metal were then thermally deposited under high vacuum. The devices were then encapsulated with a commercially purchased epoxy material. The device architecture is shown in Figure 1-25.

Devices were prepared with the Yb porphyrin complexes blended into polystyrene at varying wt% in order to determine the effects of dopant concentration on device performance. Electroluminescence spectra of the Yb porphyrin devices at 40 wt% are shown in Figures 2-8 – 2-9. The emission is shown as a function of voltage. At all concentrations, Yb^{3+} is the predominant emitter in the devices with a near-infrared emission at 977 nm. The emission observed results from direct electron-hole recombination which occurs at the Yb porphyrin complex. As the voltage is increased, the spectral shape of the Yb^{3+} begins to show a defined emission band at 920 nm. This could be due to the fact that the $^2\text{F}_{5/2}$ energy state of Yb^{3+} is in a non-symmetric environment and is split into three crystal field states. The splitting of these states is on the order of a few hundred cm^{-1} . With a sufficiently long excited state lifetime, thermal equilibrium is established between the lowest and second lowest excited states which results in emission of a higher energy band at 920 nm. The $\text{Yb}(\text{TPyP})\text{L}(\text{OEt})_3$ devices were less stable and failed at a lower voltage than the other devices. This can possibly be

attributed to the fact that electrochemical experiments show that there is no reversible oxidation of the complex. The current density-voltage (j -V) profiles of the devices are shown in Figure 2-10. The turn-on voltages for the devices were typically 6 V for the 40 wt% devices and 5 V for the 60 wt% devices. Although near-infrared emission is the predominant emission process, there exists a significant emission in the visible region which mirrors the typical porphyrin emission. This emission is roughly 1 – 5 % of the intensity of the near-infrared emission after correction for instrument response. This visible emission can be attributed to two possible pathways. Either the emission comes from a free base porphyrin impurity or it results from a more complicated process of delayed fluorescence. This process of delayed fluorescence, results from a back energy transfer from the lanthanide to the porphyrin triplet state. This in turn reacts with another porphyrin in a triplet state, resulting in a singly excited porphyrin, which then can emit.

The current densities of all of the devices were somewhat similar suggesting that change to the porphyrin structure has little effect on charge transport properties of the complex. As the amount of Yb porphyrin complex was increased, the efficiency increased. This is indicative of better charge transport through the device, confirming previous studies suggesting that the porphyrin is the key to charge transport.^[175, 183]

The near-infrared external quantum efficiencies, measured as photons collected per electrons injected, for 40 and 60 wt% are show in Figure 2-11. At 40 wt% the maximum efficiency of Yb(TPP)Q is $\sim 2 \times 10^{-4}$ and increases to 4×10^{-5} with increase in concentration to 60 wt%. Efficiency in the other devices ranged from $1 - 3 \times 10^{-4}$, which agrees with previous Yb(TPP)L device performance.^[169] This again suggests that the changes to the porphyrin have little effect on the electronic properties of the complexes.

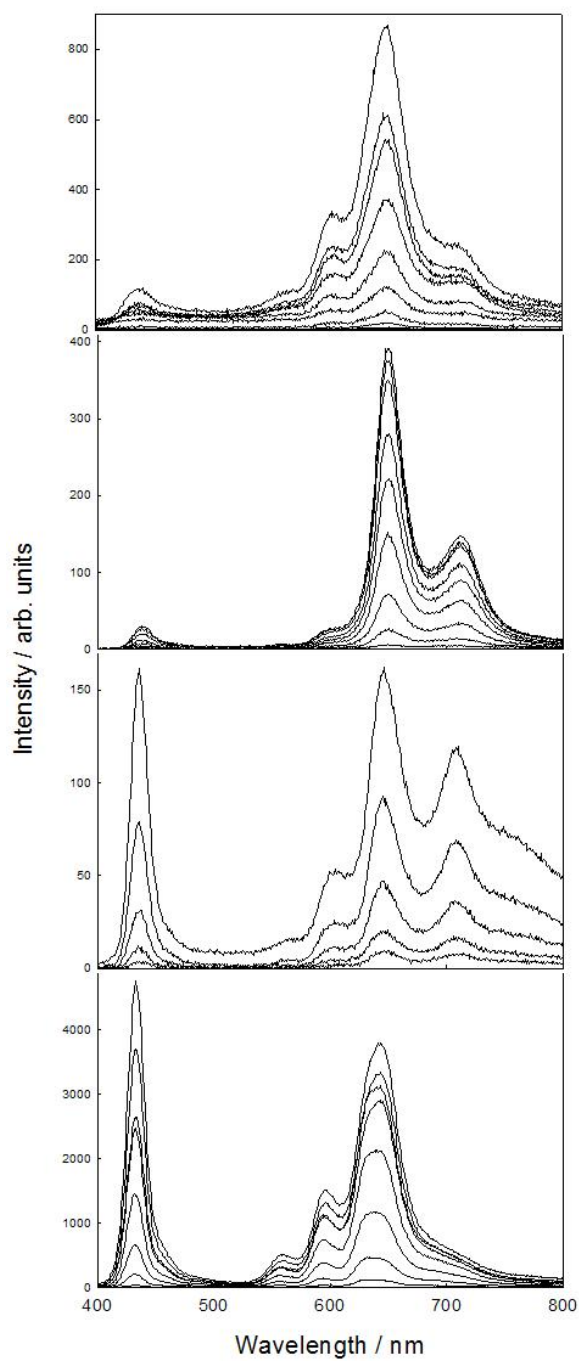


Figure 2-8. Visible electroluminescence of Yb(TPP)Q, Yb(TMPP)TP, Yb(TPyP)L(OEt)₃, and Yb(TPP_OEH)TP as a function of increasing voltage, starting at 6V.

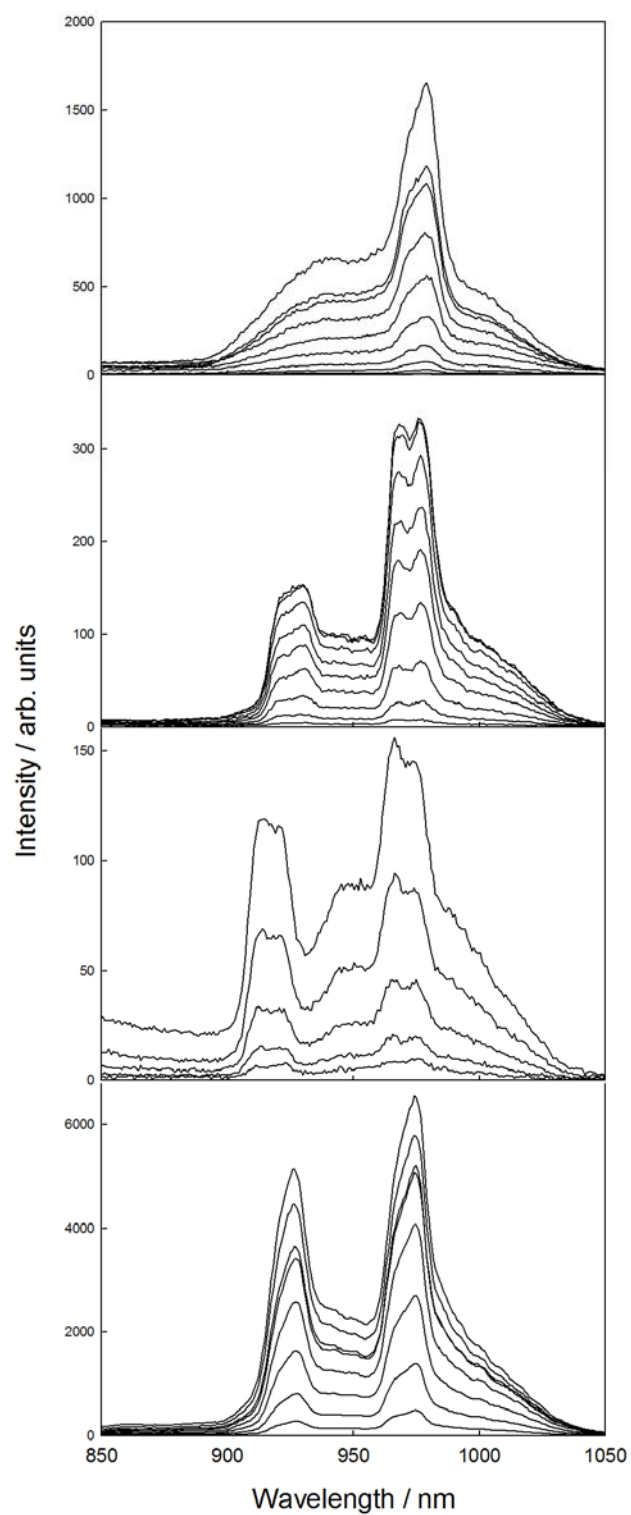


Figure 2-9. NIR Electroluminescence of Yb(TPP)Q, Yb(TMPP)TP, Yb(TPyP)L(OEt)₃, and Yb(TPP_OEH)TP as a function of increasing voltage, starting at 6V.

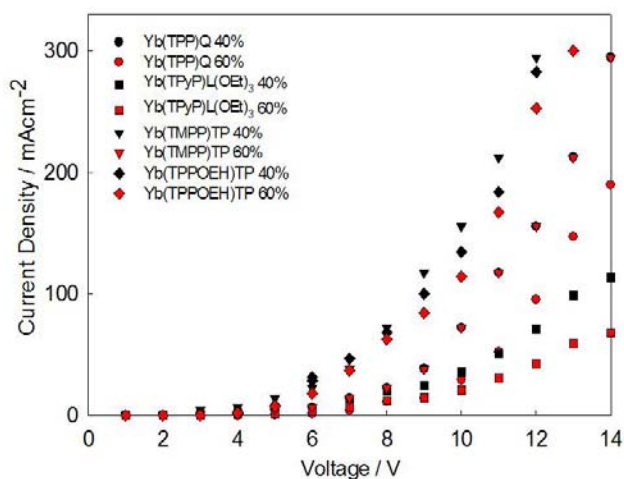


Figure 2-10. Current density – Voltage (j-V) plot of Yb porphyrin devices as a function of loading wt% in PS.

The decrease in near-infrared efficiency with increasing current density is due to three possible factors. First, because the lifetime of the lanthanide excited state is long, $\sim 40 \mu\text{sec}$, saturation of the emissive sites can occur at high current densities.^[184] Work by others has shown that the decrease in efficiency can be due to triplet-triplet annihilation.^[98] A final possibility is due to permanent degradation of the device through chemical reactions. Charge hopping is believed to be the primary charge transport mechanism in Yb porphyrin blended into the non-conducting polystyrene devices. Previous work with ZnTPP in poly(2-vinylpyridine) showed that, when ZnTPP molecules were within 1.1 nm of each other, charge hopping occurs.^[185] The porphyrin complexes in this study are expected to be within 1 nm of each other due to aggregate effects.

Figure 2-12 shows the charge-hopping model. In this model holes are injected at the anode and electrons are injected at the cathode. The carriers then hop along the porphyrins until they either combine with the opposite carrier, and create an excited porphyrin, or are annihilated at the opposite electrode.

Previous research showed that the rate of hole transport in Yb(TPP)L far exceeded the rate of electron transport.^[169] In order to study this effect, devices were fabricated in which a known electron transporter, tris(8-hydroxyquinolate) aluminum (Alq₃), was blended into the Yb(TPP)TP/PS matrix. Figure 2-13 shows the current density-voltage and NIR irradiance-voltage characteristics for 0, 33, and 50 wt% (Alq₃/Yb(TPP)TP) respectively. The current density at a given voltage drops dramatically with the increased introduction of Alq₃ until 66 wt% Alq₃, where the devices become unstable. This decrease in current density is characteristic of an increase in charge carrier balance. The NIR irradiance increases by a factor of two from 0 to 50 wt% Alq₃. This suggests that more excitons are recombining on the porphyrins resulting in greater light output. The NIR external quantum efficiency-current density characteristics are shown in Figure 2-14. The efficiency increases by a factor of ten and the data variance decreases with increasing Alq₃ concentration again suggesting better charge transport and improved device performance.

In order to determine if changes to the porphyrin structure improve the charge transport capabilities, the same Alq₃ blending experiment was carried out with Yb(TMPP)TP. Figure 2-15 shows the current density-voltage and NIR irradiance-voltage characteristics of the devices. Again, as in the Yb(TPP)TP based devices, there is a decrease in current density and an increase in NIR irradiance with increased concentration of Alq₃. The NIR external quantum efficiency, shown in Figure 2-16, also increases by approximately a factor of ten. These results mirror those of Yb(TPP)TP, suggesting again that the changes to the porphyrin structure have little effect on charge transport properties of the complexes.

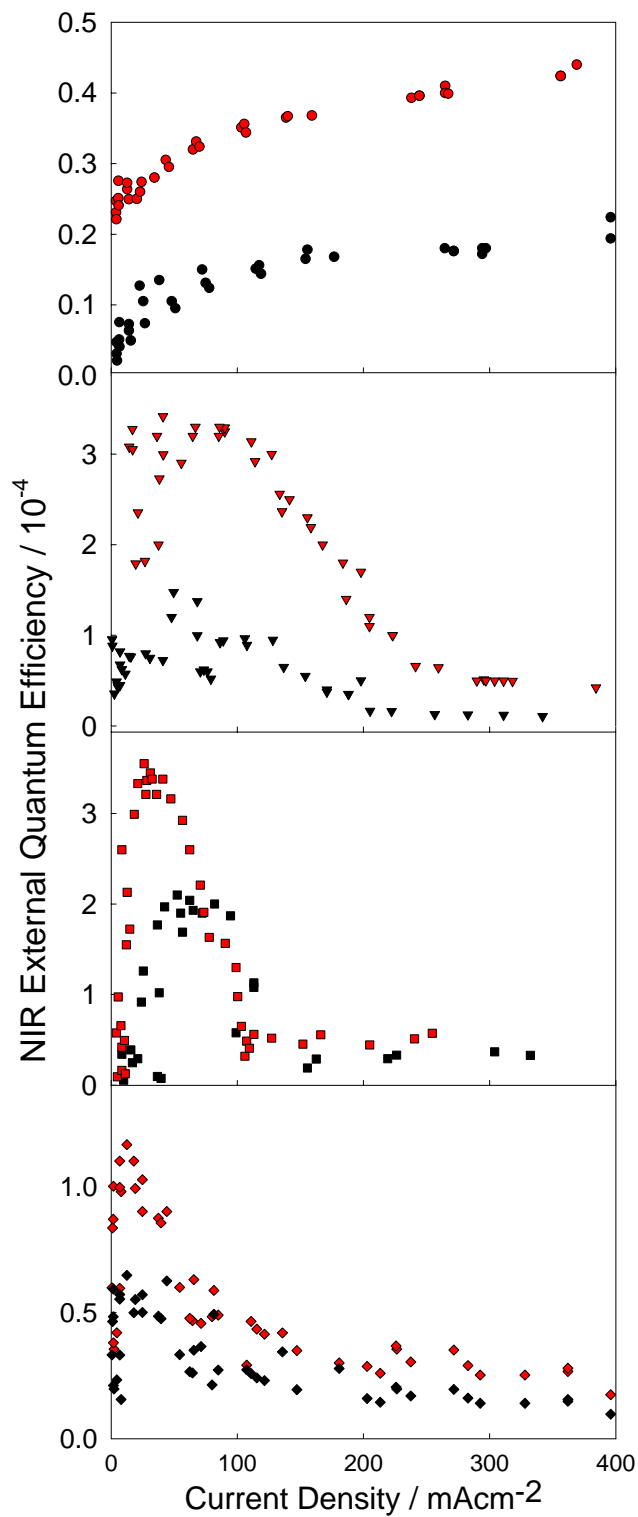


Figure 2-11. Near-Infrared external electroluminescent quantum efficiency for Yb(TPP)Q, Yb(TMPP)TP, Yb(TPyP)L(OEt)₃, and Yb(TPP_OEH)TP as a function of loading in PS. (black = 40%, red = 60%).

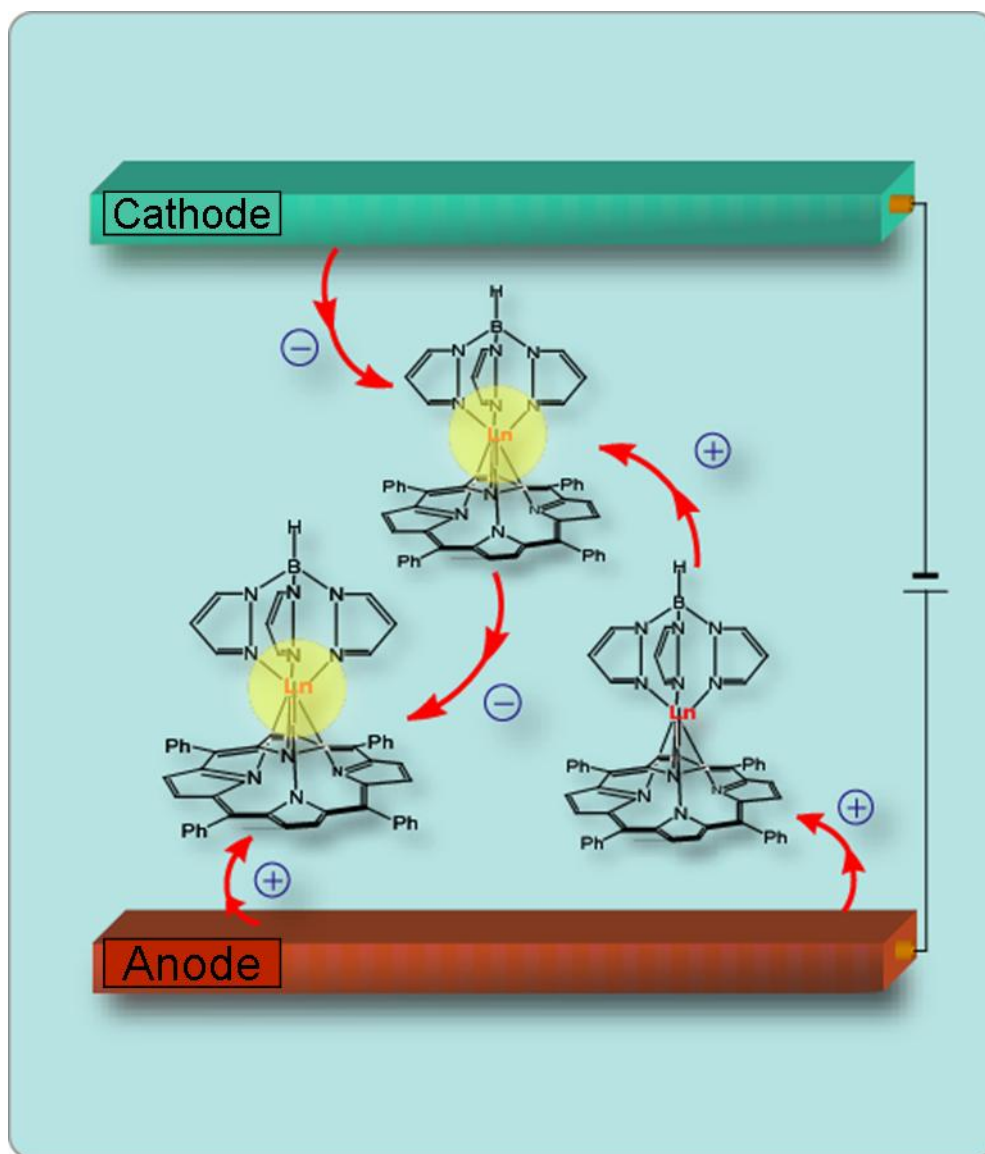


Figure 2-12. Charge hopping model showing transport of charges on porphyrin molecules. ^[177]

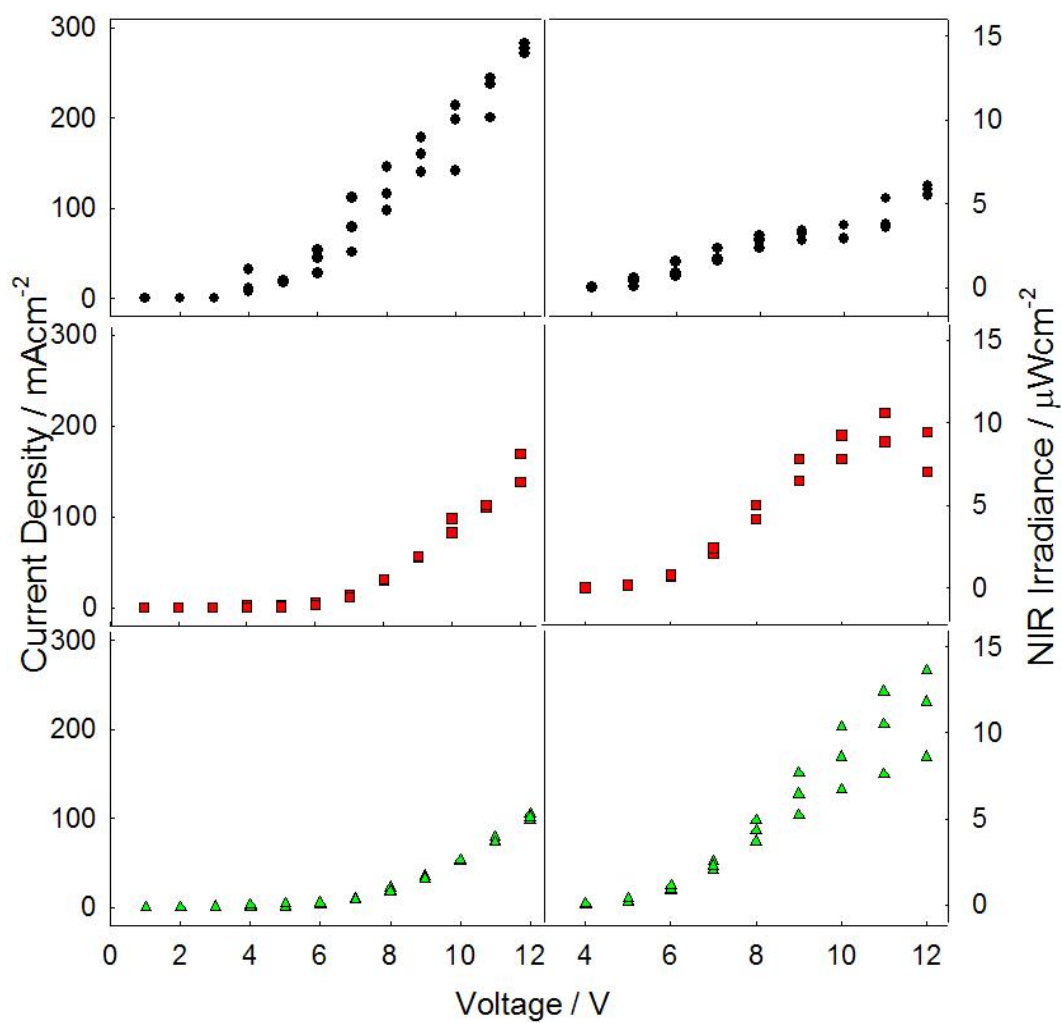


Figure 2-13. Current density-Voltage and NIR irradiance-voltage plots of Yb(TPP)TP as a function of Alq₃ loading: (●) 0 wt %, (■) 33 wt%, and (▲) 66 wt %.

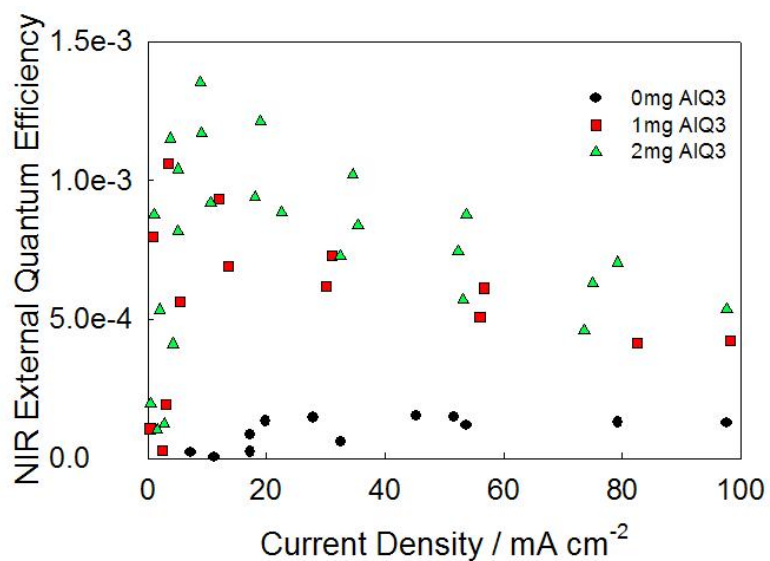


Figure 2-14. NIR External quantum efficiency of Yb(TPP)TP as a function of Alq₃ loading: (●) 0 wt %, (■) 33 wt%, and (▲) 66 wt %.

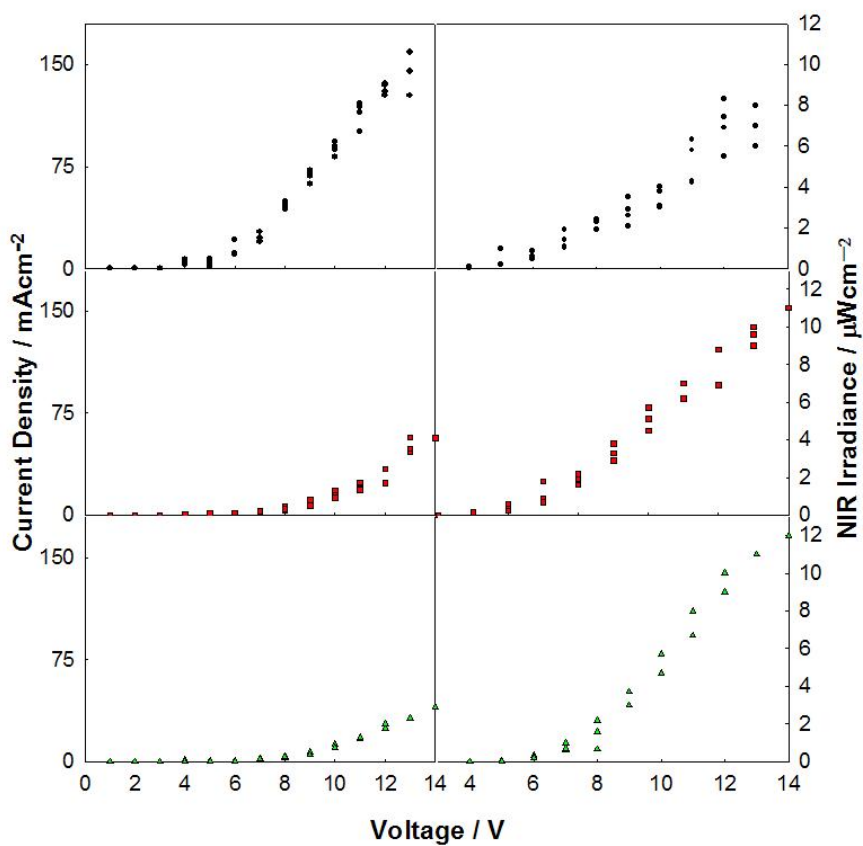


Figure 2-15. Current density-voltage and NIR irradiance-voltage plots of Yb(TMPP)TP as a function of Alq₃ loading: (●) 0 wt %, (■) 33 wt%, and (▲) 66 wt %.

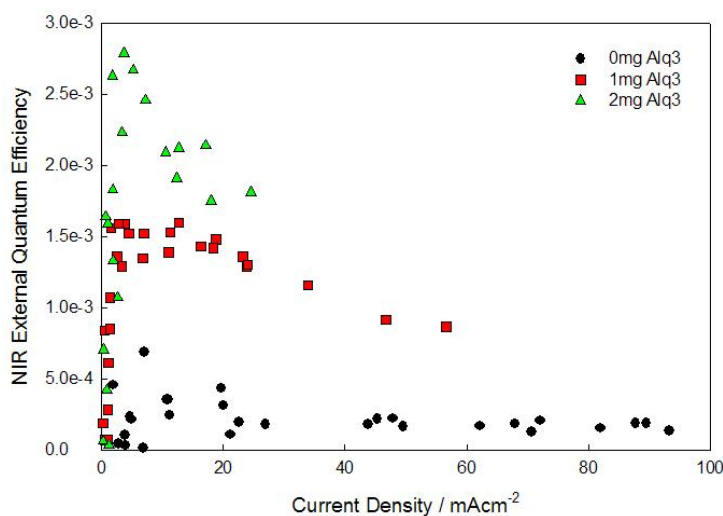


Figure 2-16. NIR external quantum efficiency of Yb(TMPP)TP as a function of Alq₃ loading: (●) 0 wt %, (■) 33 wt%, and (▲) 66 wt %.

Electrochemistry

Electrochemistry provides valuable insight into the electronic properties of molecules. This technique provides information on the position of the energy levels, in particular the highest occupied molecular orbital (HOMO) and the lowest unoccupied molecular orbital (LUMO) are easily discernable from these measurements. The position of the HOMO of a molecule is probed by determining its anodic potential, while the position of the LUMO is determined by its cathodic potential. These positions can be referenced with respect to the vacuum level by adding 4.7 eV to the onset of the peak (oxidation / reduction) with respect to the ferrocene / ferrocenium (Fc / Fc⁺) redox couple.^[186] Table 2-3 shows the electrochemical window of the solvents used in these experiments. The electrochemical measurements were undertaken by Avni Argun. The measurements of the oxidation potential(s) of all samples were carried out using a Pt working electrode in CH₂Cl₂. The measurements of the reduction potential(s) were carried out using either a Pt or glassy carbon working electrode in tetrahydrofuran (THF).

All measurements were carried out using 1 mM analyte in 0.1 M tetrabutylammonium hexafluorophosphate (TBAPF₆) with a platinum flag secondary electrode and a calibrated silver wire reference pseudo-electrode.

Table 2-3. Electrochemical windows of solvents.

Solvent	Anodic Limit*	Cathodic Limit*
THF	1.8 V	-3.5 V
CH ₂ Cl ₂	1.8 V	-1.9 V
MeCN	1.8 V	-2.0 V

* potentials vs. SCE

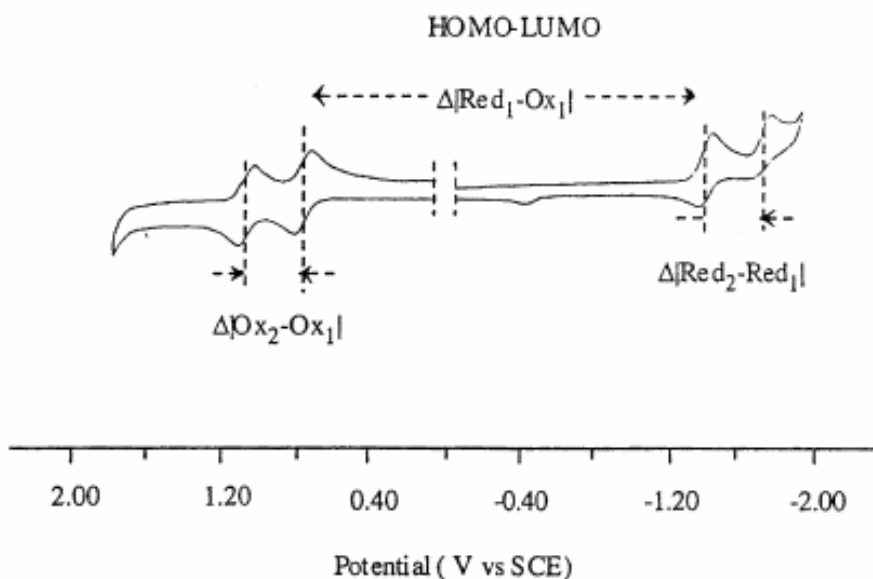


Figure 2-17. Redox properties of free-base tetraphenylporphyrin with respect to the saturated calomel electrode.^[187]

The electrochemical properties of tetraphenylporphyrin were determined in order to verify the validity of the experiment, given the fact that the electrochemical properties of TPP are well known. The first oxidation with respect to Fc/Fc⁺ was determined to be 0.54 V and was determined to be reversible. The first reduction peak was determined to be located at -1.75 V and was also reversible. These observations correspond well with

previously published results.^[187] The electrochemical “band-gap” (HOMO – LUMO gap), which was determined by the difference of the $E_{1/2}$ of the anodic and cathodic waves, was determined to be ~ 2.2 eV which corresponds well with the optical gap measured by absorption.

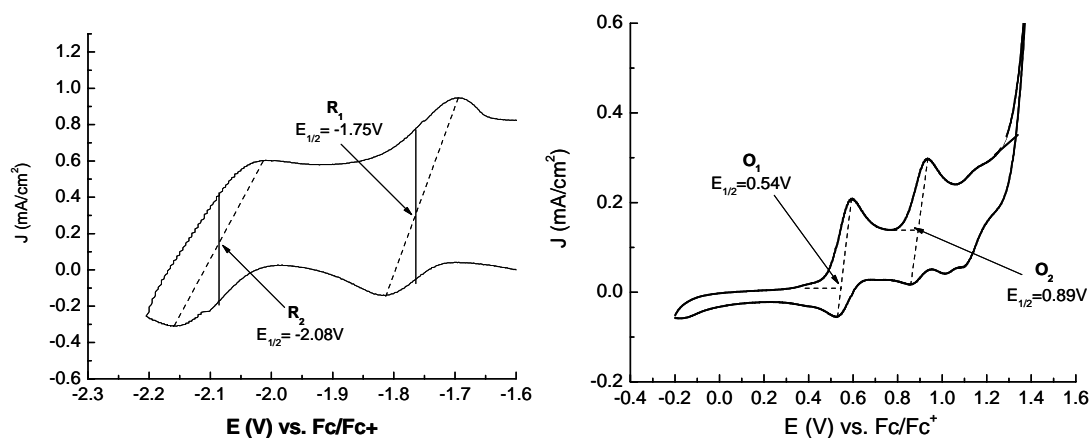


Figure 2-18. Reduction and oxidation waves for free-base tetraphenylporphyrin.

In order to understand the effect of the lanthanide metal on the redox properties of the porphyrin system, the electrochemical properties of Yb(TPP)TP were studied. The first oxidation was determined to be located at 0.58 V, which is nearly identical to the non-metallated porphyrin. The first reduction potential was determined to be located at -1.67 V and again corresponds well with the free-base porphyrin. This suggests that the lanthanide metal has little effect on the positions of the HOMO and LUMO levels. Although the first oxidation was similar to TPP, the reduction wave for Yb(TPP)TP was significantly different with respect to TPP. There exists an irreversible reduction at -2.2 V which has been attributed to $\text{Yb}^{3+} + \text{e}^- \rightarrow \text{Yb}^{2+}$.

The redox properties of Yb(TPP)Q are somewhat similar to those of Yb(TPP)TP with the first oxidation located at 0.58 V, while the reduction has shifted to -1.98 V.

There also exists an irreversible oxidation at 0.35 V which is possibly due to the oxidation of the quinolate axial ligand. The reduction of the quinolate was determined to be at -2.9 V. This evidence suggests that the quinolate ligand has only a minor effect on the electronic properties of the complex.

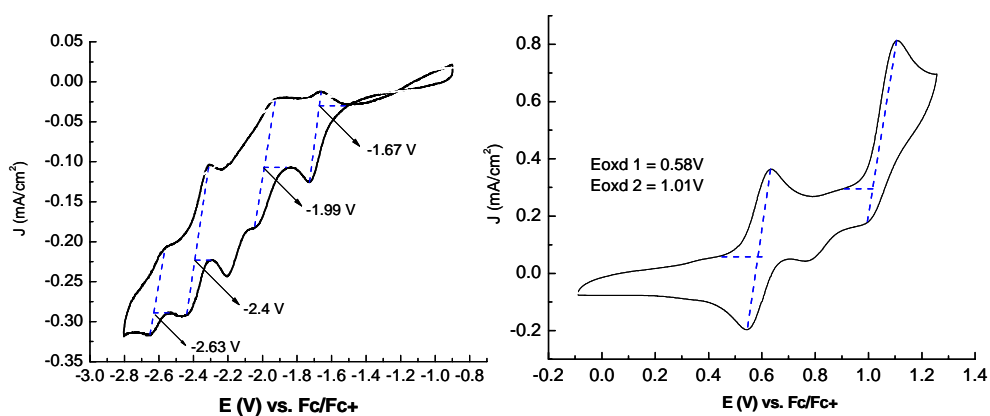


Figure 2-19. Reduction and oxidation waves for Yb(TPP)TP.

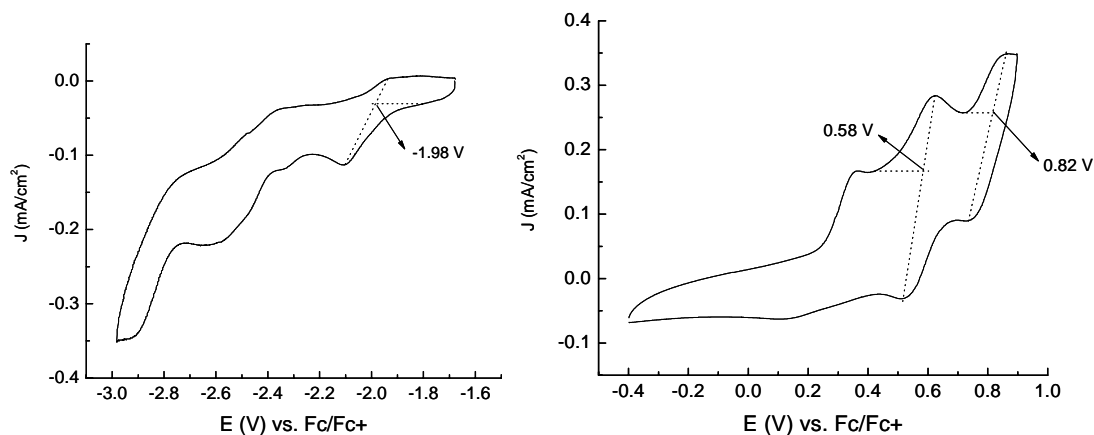


Figure 2-20. Reduction and oxidation potentials for Yb(TPP)Q.

The electrochemical properties of Yb(TMPP)TP were then studied. It was expected that the electron donating alkoxy groups would make the complex easier to oxidize, but that was not the case. The first oxidation potential was determined to be located at 0.6 V. The first reduction potential was determined to be located at -1.97 V.

This suggests that substitution on the meso phenyl groups has little effect in influencing the redox properties of the complex.

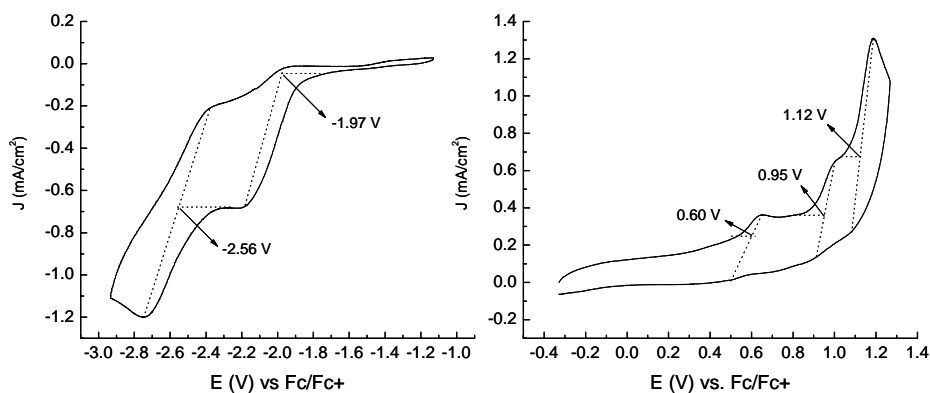


Figure 2-21. Reduction and oxidation waves for Yb(TMPP)TP.

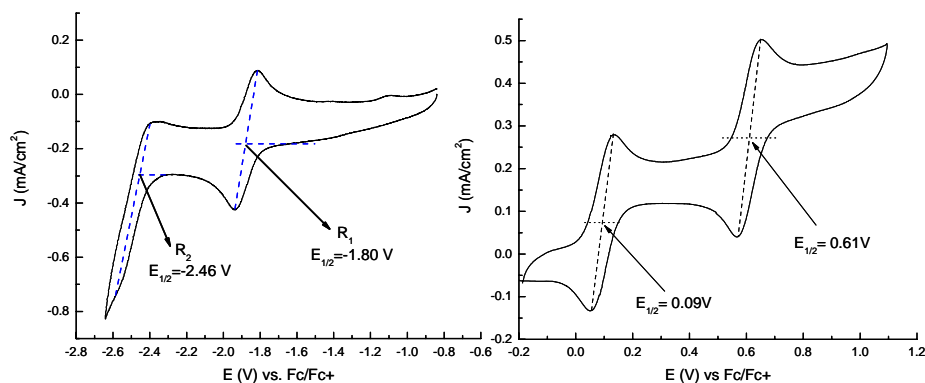


Figure 2-22. Reduction and oxidation waves for Yb(TPP)L(OEt)₃.

Next, the redox properties of Yb(TPyP)L(OEt)₃ were determined. In order to understand the effect of the axial Klaui ligand, the redox properties of Yb(TPP)L(OEt)₃ were first determined. It was shown that the first oxidation potential was dramatically changed from ~ 0.6 V for the TP complex to ~ 0.1 V for the Klaui complex. This lower oxidation is most likely the oxidation of the Klaui ligand.^[188] The second oxidation of the Klaui complex was similar to the first oxidation states of the other complexes, providing evidence to that suggestion. After showing that the Klaui ligand has little

effect on the overall properties, the redox properties due to the pyridine substitution could be determined. The complex showed no reversible oxidation, probably due to the creation of a reactive cation radical. This non-reversible oxidation is most likely contributing to the poor stability of electroluminescent devices fabricated from the complex. The first reduction was similar to that of all of the other complexes, again showing that substitution at the phenyl group has little effect upon the overall electronic properties of the system.

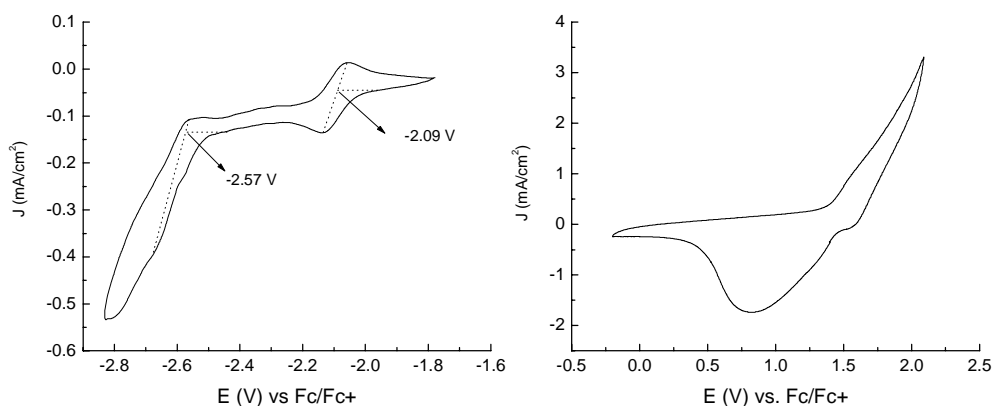


Figure 2-23. Reduction and oxidation waves for $\text{Yb}(\text{TPyP})\text{L}(\text{OEt})_3$.

Conclusions

From these results, there come two major problems which much be addressed in order to produce more efficient near-infrared devices. The first is that non-radiative decay is a controlling factor in the low near-infrared photoluminescence quantum yield of lanthanide porphyrin complexes. This process is facilitated by the large number of C-H oscillators which are in close proximity to the Yb^{3+} ion. In order to improve NIR PL quantum yield, and in turn increase the theoretical NIR EL quantum yield, substitution of these protons with heavier atoms (halogens) must occur.

The second major problem is the lack of carrier balance in Yb porphyrin LEDs. Substitution on the *meso*-phenyl groups of TPP has little effect on the charge transport properties of these complexes. Therefore these novel complexes still facilitate hole transport and hinder electron transport. In order to correct this problem, the electron transporting ability must be increased. This can be accomplished by either lowering the LUMO by substitution of electron withdrawing moieties on the pyrroles of the porphyrin or by creating a “molecular wire” in which electrons can flow freely, reducing the barrier for electron injection.

Table 2-4. Electrochemical properties of substituted porphyrins.

Compound	Oxidation Potential (Ox1) V*	Reduction Potential (Red1) V*	(Red1 -Ox1) (Eg)	Optical HOMO-LUMO gap (from the lowest energy Q band)
TPP Free base	0.54	-1.75	2.2 eV	664 nm (1.87 eV)
Yb (TPP) (L(OEt))	0.09	-1.8	1.9 eV	617 nm (2.00 eV)
Yb (TPP) TP	0.58	-1.67	2.2 eV	603 nm (2.06 eV)
Yb(TPP)Q	0.58	-1.98	-2.6	607 nm (2.04 eV)
Yb (TMPP) TP	0.6	-1.97	2.6 eV	609 nm (2.04 eV)
Yb (TPyP) (L(OEt))	-	-2.09	-	616 nm (2.01 eV)
Yb (TPP_OEH) TP	0.59	-1.64	2.2 eV	604 nm (2.05 eV)

* Potential vs. Fc/Fc⁺

Experimental

Photophysical Measurements

All photophysical studies were conducted in 1 cm square quartz cuvettes unless otherwise noted. All absorption and emission measurements were made in CH₂Cl₂ unless otherwise noted. Absorption spectra were obtained on a double-beam Cary-100 UV-

visible spectrophotometer. Fluorescence spectra were measured on a SPEX Fluorolog-2 equipped with a water-cooled Hamamatsu R928 PMT for visible measurements and a liquid nitrogen cooled InGaAs diode detector for near-infrared measurements. All measurements were corrected for detector response.

Photoluminescence quantum yields in solution (Φ_{PL}) were calculated using equation 2.5, where the absorption of the reference is given by A_R , and the absorption of the sample is given by A_S . The refractive indices of the solvents are given by the term n . The integrated area of the emission peaks of the sample and standard are given by, F_S and F_R respectively. Φ_R is the quantum yield for the standard. Yb(TPP)TP in CH_2Cl_2 ($\Phi = 0.033$) was used as the relative quantum yield standard.

$$\Phi_S = \frac{10^{-A_R} n_S^2 F_S}{10^{-A_S} n_R^2 F_R} \Phi_R \quad (2.5)$$

Device Fabrication

ITO Etching

Electroluminescent devices were prepared by masking, then etching the ITO coated glass (Delta Technologies, $R_s = 8 - 12 \Omega / \square$) by exposure to aqua-regia vapor. The ITO-glass sheets were cut into 1" x 1" squares by the use of a glass cutter. Packing tape was then carefully placed over the sheet of glass, ensuring that no bubbles were present. With the use of a black marker, a rectangle was drawn onto the tape to indicate where the tape would be removed. A razor knife was then used to remove the indicated areas. The ITO glass squares were then placed upon a beaker containing a freshly prepared solution of aqua-regia, where they remained for 6 minutes. After removal from the beaker, the exposed areas were wiped with a cotton swab removing the dissolved

ITO. The tape was then removed and the ITO was rinsed with isopropanol to ensure removal of any remaining acid.



Figure 2-24. Cartoon showing ITO substrate placed at top of beaker containing solution of aqua regia allowing vapors to etch surface.

Cleaning ITO

The etched ITO squares were then placed into a Teflon holder. They were subsequently sonicated for 10 minutes in each of the following solutions: aqueous sodium dodecyl sulfate (SDS, Fisher), Milli-Q water, acetone (Fisher, ACS grade), and isopropanol (Fisher, ACS grade). The ITO-glass squares were dried under stream of filtered air. They were then placed into an oxygen plasma cleaner (Harrick PDC-32G) for 15 minutes.

Spin Coating

PEDOT-PSS (Bayer, Baytron P VP Al 4083) was used as the hole transport layer. The PEDOT-PSS suspension was first filtered through a 0.2 micron Polysulfone filter to ensure removal of particulate matter. The PEDOT-PSS was then spin-coated (Chemmat, KW-4A) onto the ITO surface at 4000 rpm for 30 seconds. The PEDOT-PSS coated ITO-glass was then dried in a vacuum oven at 150°C for 4 hours in order to remove residual water.

Solutions of the desired wt% of porphyrin complex were created by dissolving the corresponding mass of Yb porphyrin complex into a 1 mL CHCl_3 solution containing 3mg of polystyrene (PS) (Aldrich, M_n 280,000). These solutions were then spin-coated onto the substrate at 1000 rpm.

Metal Electrode Deposition

The films were placed glass side down onto an inverted stage designed to fit into the chamber of the thermal evaporator (Denton Vacuum, DV502A). The ITO was then covered with a stainless steel mask with the pattern of the electrodes desired. The masked devices are then placed into the thermal evaporator and pumped down to 10^{-6} torr for 12 hours. Calcium (or LiF) and aluminum layers were sequentially deposited by thermal evaporation at 2×10^{-7} torr without breaking the vacuum. The thicknesses were adjusted by the use of a calibrated oscillating quartz crystal thickness monitor. The thicknesses used for all devices were: 50 Å for Ca, 5 Å for LiF and 2000 Å for Al. The devices were left in the evaporator to cool for 30 minutes after deposition. The chamber was then purged with nitrogen and the devices removed and encapsulated with epoxy (Loctite quick set epoxy) in order to minimize exposure to oxygen and moisture.

Electroluminescent Device Measurements

Visible and near-infrared (< 1000 nm) electroluminescence spectra were recorded on a ISA-SPEX Triax 180 spectrograph fitted with a liquid nitrogen cooled CCD detector (EEV CCD, 1024 x 128 pixels, 400 – 1100 nm). The devices were placed into the device holder such that electrical contact was made between the vapor-deposited electrodes of the device and the gold pins of the device holder. The device holder was then mounted onto an x-y stage as close as possible to the entrance slit of the Triax 180 (4.8 cm). Using the x-y stage, the electrode to be measured is placed in the center of the monochromator

opening. Power for electroluminescent measurements was supplied using a Keithley 228 voltage / current source. Positive bias was applied to one of the corners of the device holder, while negative bias was applied to the electrode under investigation. The CCD was calibrated into energy units by the use of a primary standard quartz tungsten halogen lamp.

Electrochemistry

All electrochemistry was performed using an EG&G PAR model 273A potentiostat/galvanostat in a three-electrode cell configuration containing a platinum button or a glassy carbon button as the working electrode, a platinum flag as the counter electrode, and a silver wire as the pseudo-reference electrode calibrated with a Fc/Fc⁺ redox couple. Lanthanide containing porphyrin complexes (1 mM) and 0.1M tetrabutylammonium hexafluorophosphate (TBAPF₆, a non-coordinating supporting electrolyte) were dissolved in non aqueous solvents such as dichloro methane (for oxidation) and THF (for reduction). CV studies were carried out under argon blanket at a scan rate of 50 mV/s, to determine the redox couples of the compounds. HOMO-LUMO gaps were obtained from the $E_{1/2}$ difference of the first oxidation and the first reduction couples.

CHAPTER 3 PORPHYRIN PENDANT POLYACETYLENES

Introduction

The Nobel Prize winning discovery of doped polyacetylene resulted in the field of conjugated polymers. Polyacetylene is the archetypical conjugated polymer, with alternating single and double bonds, which in its doped form shows metallic behavior.^[189] The polymer, however, is insoluble, infusible, and unstable in air. This severely limits its use in optical materials. Substituted polyacetylenes are quite different from unsubstituted polyacetylenes, especially when they contain bulky substituents.^[190] Backbone substitution results in an increase in photoluminescence yield and tunable emission properties dependant on the number and nature of substituents.^[191-210] These polymers have been studied for possible use in light emitting diodes, photovoltaic materials, nonlinear optical materials, gas permeable membranes, sensors, and magnetic materials.^[79, 197, 211-241]

The previous chapter focused on the emissive properties of lanthanide porphyrin systems blended into polystyrene and their electroluminescent properties. Previous work by Harrison and coworkers demonstrated the use of conjugated polymers as hosts for blended materials for light emitting diodes.^[169] This chapter discusses the combination of the two principles. The idea of the research was that the porphyrin could be appended to a conjugated polymer, resulting in more efficient carrier transport as well as enhanced emission through Förster energy transfer.

Monomer Synthesis and Polymerization

The use of porphyrin pendant polyacetylenes was first shown in a paper by Aramata, Kajiwara, and Kamachi in 1995.^[242] Their goal was to develop a polymer which had a magnetically active side chain. Their belief was that the π electron of the unsaturated main chain would enhance the magnetic properties of the metalloporphyrin pendant. They therefore synthesized a porphyrin monomer bearing a terminal alkyne which could be easily polymerized using commercially available catalysts. Although successful in the monomer preparation, they discovered that purification was extremely difficult and the resulting yield was extremely low (6 %). This difficulty in purification was due to the relative inability to separate the statistical mix of porphyrin products. The major problem was the choice of protecting groups. The use of the trimethylsilyl (TMS) group resulted in little polarity change from the base phenyl, and therefore made column chromatography difficult. Therefore a different procedure was needed in which purification could be achieved more easily. Lindsey *et al.* discovered that the use of polar protecting groups eased the purification process.^[243] This was the procedure carried out to synthesize the porphyrin pendent monomer used throughout this study, and the scheme is shown in Figure 3-1. The first step of the reaction was the Sonogoshira coupling of the protected acetylene to 4-bromobenzaldehyde to produce 4-(3-methyl-3-hydroxybut-1-yn-1-yl)benzaldehyde (**1**). The second step was the condensation of three equivalents of benzaldehyde with one equivalent of compound (**1**) with excess pyrrole in a dilute solution in CHCl_3 with the lewis acid, $\text{BF}_3 \cdot \text{OEt}_2$, acting as a catalyst. This was immediately followed by oxidation of the resulting porphyrinogen to the desired porphyrins by the addition of DDQ. The resulting product was a statistical mixture of tetraphenylporphyrin, and mono-, di-, tri-, and tetra-substituted porphyrins. Purification

was achieved by column chromatography. The desired product, 5-[4-(3-methyl-3-hydroxy-1-butyn-1-yl)phenyl]-10,15,20-triphenylporphyrin (**2**), was then deprotected using sodium hydroxide, resulting in the product, 5-(4-ethynylphenyl)-10,15,20-triphenylporphyrin (**3**). The porphyrin was then metallated using zinc (II) acetate to give the final product, Zn(II)-5-(4-ethynylphenyl)-10,15,20-triphenylporphyrin (**4**).

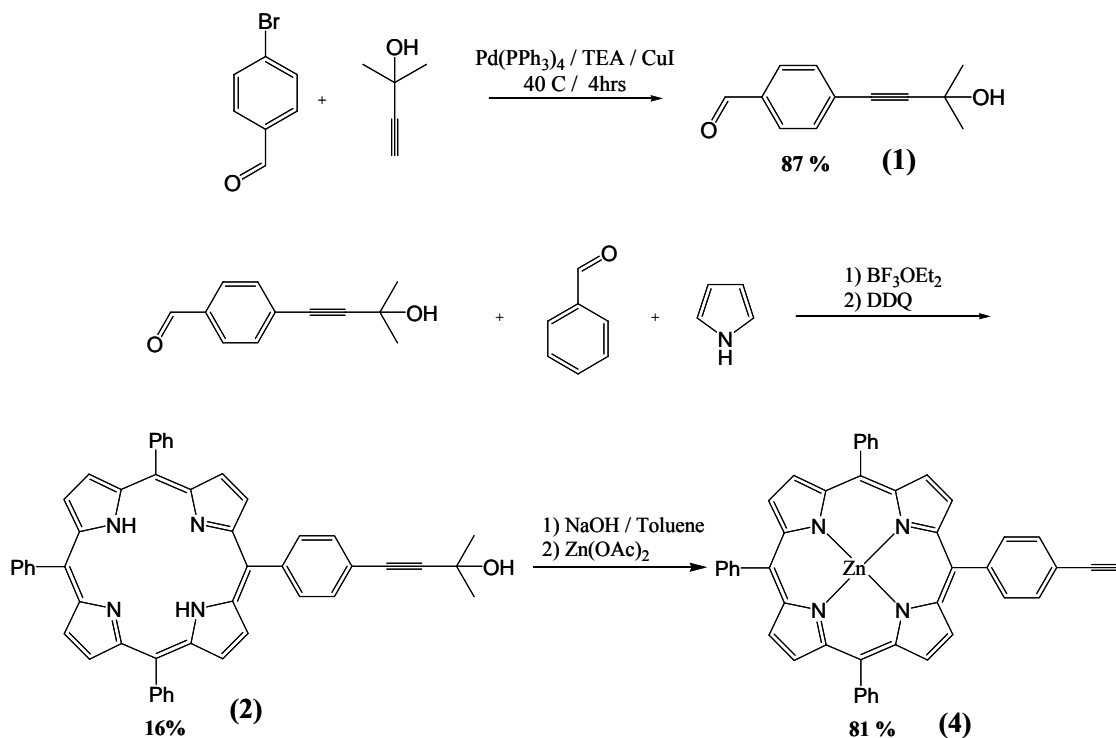


Figure 3-1. Synthesis of Zn(II)-5-(4-Ethynylphenyl)-10,15,20-triphenylporphyrin (**4**).

Oxadiazoles are well known for their electron transporting and hole blocking ability due to a high electron affinity.^[228-230, 244] In an effort to increase the electron transporting ability of the acetylene polymers, an oxadiazole containing molecule possessing a terminal acetylene was synthesized. This was accomplished by a procedure suggested by Cha and coworkers.^[245] The first step involved the synthesis of 4-bromobenzhydrazide

(5) by the reaction of 4-bromo-ethylbenzoate with hydrazine. The next step was the reaction of compound (5) with 4-methylbenzoyl chloride with first pyridine followed by the reaction with POCl₃ to give the product 2-(4-bromophenyl)-5-(4-methyl)-1,3,4-oxadiazole (6) in decent yield. The next step was the Sonogoshira coupling of (6) with 2-methyl-3-butyn-2-ol to give the product 4-(2-(4-(3-methyl-3-hydroxy-1-butyn-1-yl)phenyl)-5-(4-methyl)-1,3,4-oxadiazole (7). This was followed by the subsequent deprotection using NaH to give the final product 2-(4-methylphenyl)-5-(4-ethynylphenyl)-1,3,4-oxadiazole (8).

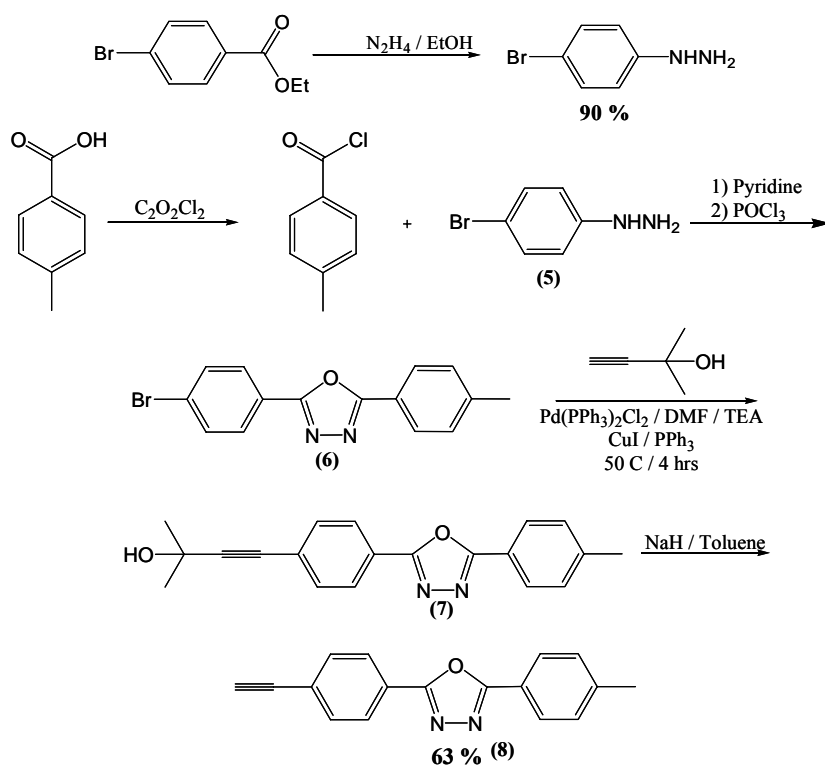


Figure 3-2. Synthesis of 2-(4-methylphenyl)-5-(4-ethynylphenyl)-1,3,4-oxadiazole (8).

The use of Rhodium catalysts for the polymerization of acetylenes has been known for many years.^[194, 246-251] The most commonly used Rh catalyst used for these

polymerizations is the rhodium norbornadiene chloride dimer shown in Figure 3-3. This family of catalysts involves an insertion type mechanism as opposed to the metathesis mechanism known for the transition metal chloride polymerization catalysts. This family of catalysts also results in the cis-transoid structure polymer as opposed to the transoid structure typically obtained by metathesis catalysts. The mechanism for the insertion type polymerization is shown in Figure 3-4. The dimeric rhodium catalyst dissociates into its monomeric form by association with the polymerization solvent. The acetylene monomer then coordinates with the rhodium metal center. The resulting vinylic complex is converted to the terminally bound acetylene by the interaction with the base to remove a proton. The polymeric chain begins and grows by insertion of the π -coordinated acetylene monomer with the metal-carbon σ bond on the metal acetylide catalyst. Termination is facilitated via monomer chain transfer. This transfer may occur when the acidic acetylenic hydrogen is transferred from the π -coordinated monomer to the propagating chain.

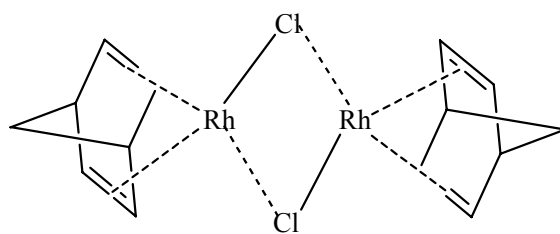


Figure 3-3. Structure of (Bicyclo[2.2.1]hepta-2,5-diene)chlororhodium(I) dimer.

For this study, the catalyst used was the rhodium norbornadiene chloride dimer. The reactions were all carried out in an argon atmosphere drybox. The monomer concentration was held at a constant ratio with respect to the catalyst (100:1). All reactions were performed with CHCl_3 as the solvent unless otherwise noted. The polymerization of compound (**4**) resulted in the homopolymer, poly(ZnETPP), shown in

Figure 3-5. A series of copolymers were also created using varying monomers as well as monomer concentrations. The copolymers created are also shown in Figure 3-6. These polymers are named as poly(ZnETPP)_x-co-(R)_y where $x + y = 1$. Thus, the polymers have the name poly(ZnETPP)_x-co-(PE)_y when the monomer is ethynyl benzene, poly(ZnETPP)_x-co-(PEOXAD)_y when the monomer is compound **(8)**, and poly(ZnETPP)_x-co-(3,5CF₃PE)_y when the monomer is 1-ethynyl-3,5-trifluoromethylbenzene. The details of the polymerizations are shown in Table 3-1. The isolated yield was fairly high for all of the polymers with the exception of poly(ZnETPP)_{0.5}-co-(PEOXAD)_{0.5} due to the fact that the polymer was extremely soluble in most common organic solvents, resulting in the lack of ability to precipitate the polymer. The molecular weights were determined by gel permeation chromatography carried out in THF with reference to polystyrene standards. The eluents were detected by a photodiode selectively tuned to the absorption of the porphyrin Soret (420 nm). The elution diagram of GPC for all of the polymers showed a unimodal pattern. The poly(ZnETPP) homopolymer was insoluble in THF and therefore the molecular weight was not determined. Determination of the absolute number average molecular weight can be estimated by the formula given by^[252]

$$\overline{M}_n = 1.48\overline{M}_n(GPC) \quad (3.1)$$

The IR band present in all of the monomers at $\sim 2110 \text{ cm}^{-1}$ assigned to the stretching vibration mode of the carbon-carbon triple bond disappeared upon polymerization. The infrared absorption bands characteristic of the porphyrin ring remained unchanged after polymerization. This confirms to the assumption that the polymerization occurs through the triple bond of the ethynyl group.

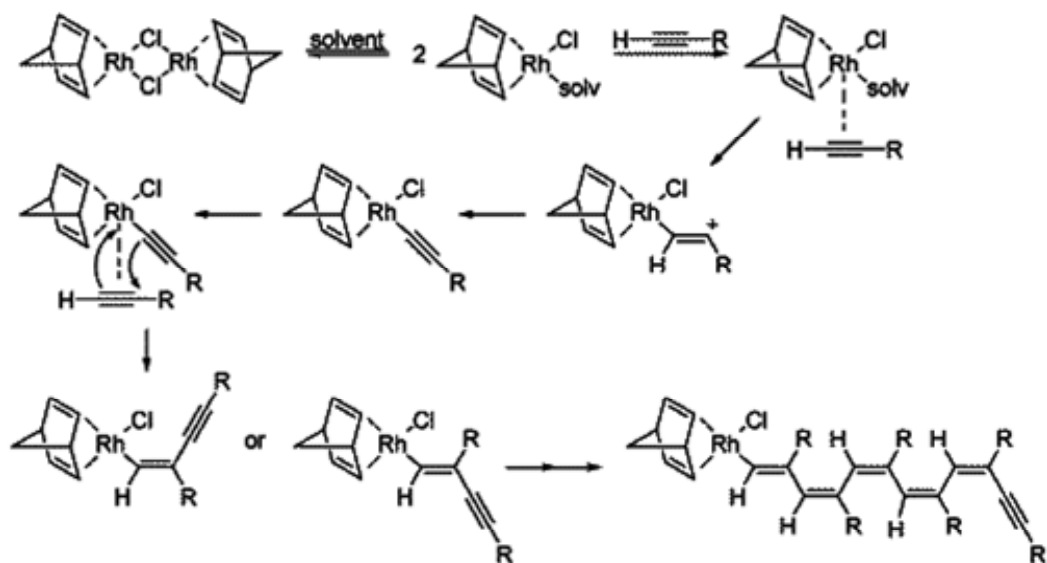


Figure 3-4. Representative scheme of insertion polymerization mechanism.^[253]

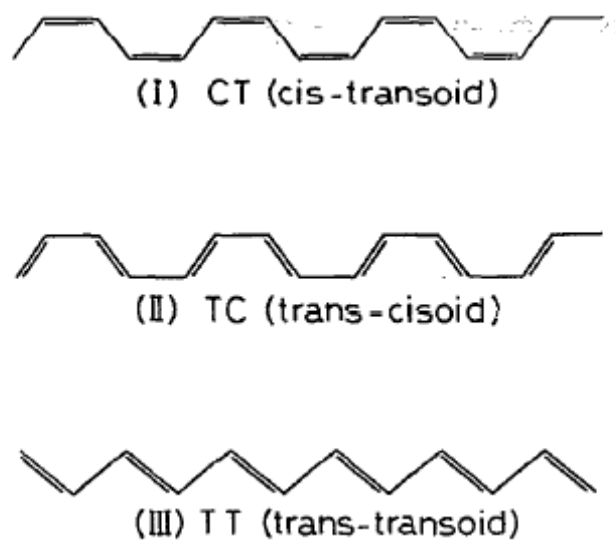


Figure 3-5. Polyacetylene isomer structures.^[250]

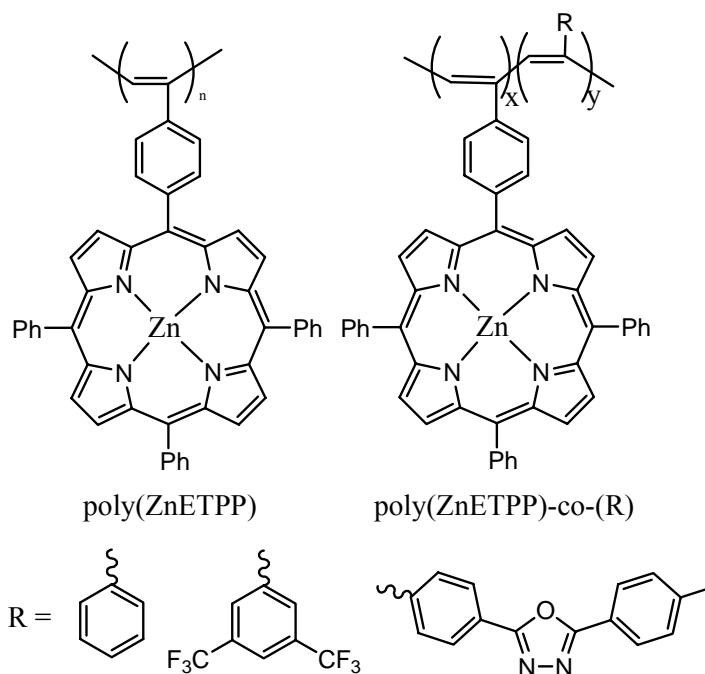


Figure 3-6. Structure of ZnETPP homopolymer and copolymers.

The copolymer ratio was determined by ^1H NMR. All NMRs were carried out in d_6 -DMSO at 90°C due to the poor solubility of the polymer. The NMR spectra showed broad peaks for the protons associated with the polymer (see Figure 3-7). The copolymer ratio was determined by the ratio of the integration of the protons on the pyrrole of the porphyrin with respect to the protons on the phenyl ring or methyl group of the other comonomer. The positions and widths of the peaks was determined by analyzing the NMR of the homopolymers. The results of these calculations are shown in Table 3-1. The copolymers ratios with (3,5 CF_3 PE) were unable to be determined by NMR due to the overlap in the spectrum. The copolymer ratios determined by NMR closely (within the ability to integrate peaks in NMR) match the ratios determined by monomer feed.

No glass transition was observed with DSC within the temperature range studied ($-80 - 180^\circ\text{C}$). As shown in Figure 3-8, the polymers display good thermal stability, with a 10% weight loss occurring above 300°C with the only exception being the

poly(ZnETPP) homopolymer. This stability has been attributed to the bulky pendant groups, which protect the polymer backbone.

Table 3-1. Polymerization details.

Polymer	Copolymer Ratio (NMR)	Mw	Mn	Mw/Mn	Isolated Yield %
Poly(ZnETPP)	—	*	*		65
Poly(ZnETPP) _{0.15} -co-(PE) _{0.85}	0.15/0.85	77500	33700	2.3	94
Poly(ZnETPP) _{0.3} -co-(PE) _{0.7}	0.25/0.75	74000	44000	1.7	88
Poly(ZnETPP) _{0.5} -co-(PE) _{0.5}	0.45/0.55	174000	78000	2.2	77
Poly(ZnETPP) _{0.7} -co-(PE) _{0.3}	0.65/0.35	160000	73000	2.2	82
Poly(ZnETPP) _{0.5} -co-(PEOXAD) _{0.5}	0.5/0.5	97000	47000	2.1	13
Poly(ZnETPP) _{0.5} -co-(3,5CF ₃ PE) _{0.5}	**	271000	162000	1.7	67

*Poly(ZnETPP) insoluble in THF. ** Unable to determine copolymer ratio via NMR.

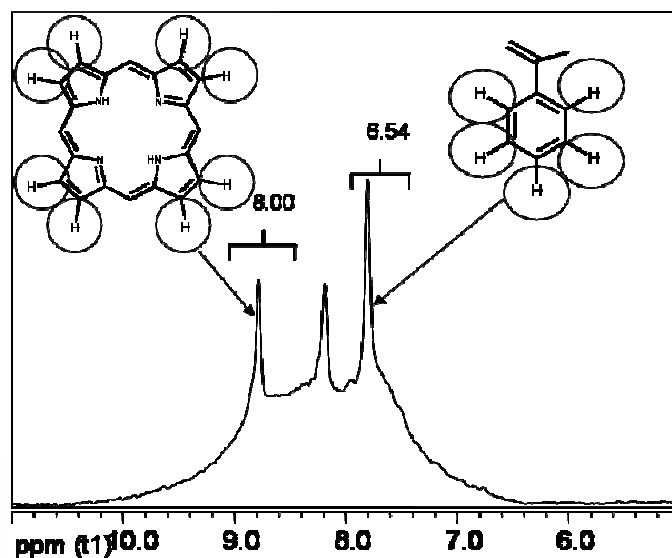


Figure 3-7. NMR spectra of poly(ZnETPP)_{0.5}-co-(PE)_{0.5}. Inset numbers indicate integration values.

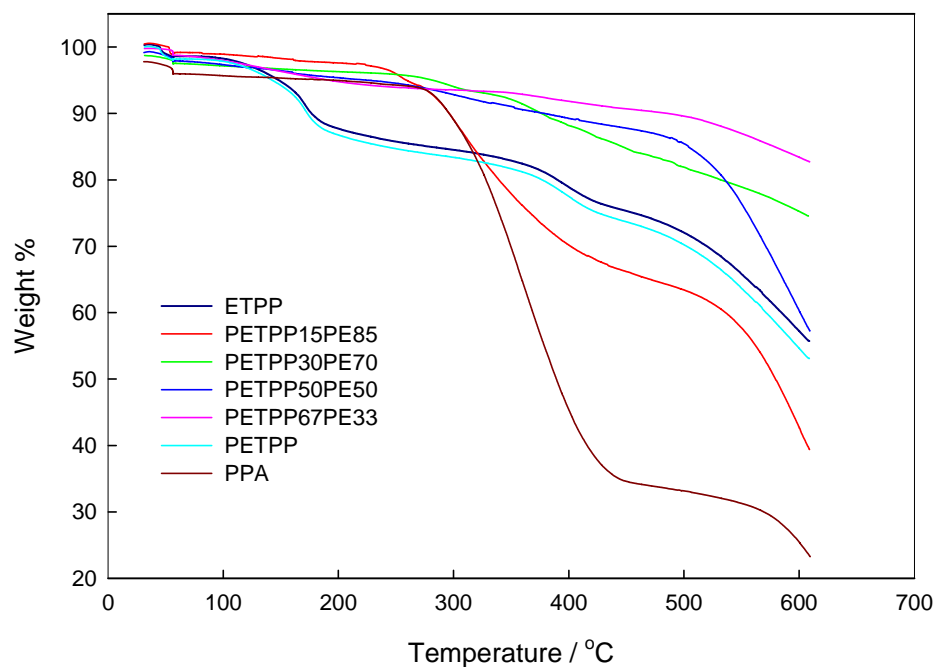


Figure 3-8. TGA traces of polymers of ETPP measured in air.

Photophysics

Absorption

All absorption measurements were made as dilute solutions in toluene unless otherwise indicated. The monomer ZnETPP shows absorption nearly identical to ZnTPP indicating the ethynyl group has little influence on the absorption of the porphyrin ring. Figure 3.9a shows the absorption spectrum of poly(ZnETPP). Close examination of the absorption spectrum shows that the molar extinction coefficient of the Soret band at 408 nm is roughly an order of magnitude weaker than ZnTPP. The Soret also shows evidence of broadening with the emergence of a second peak at 428 nm. These results indicate that hypochromism was due to electronic interactions occurring among porphyrin moieties in the polymer. This phenomenon has been observed for other porphyrin polymer systems and has been explained in terms of an exciton coupling model due to the

approach of two porphyrin rings.^[30, 37, 254] Although absorption bands due to the conjugated main chains of poly(ZnETPP) are expected to be observed in the range of 250 – 400 nm, the bands could not be distinguished from the absorption due to the porphyrin ring.^[255, 256] This indicates that the conjugation in the main chain is small as compared to that of unsubstituted polyacetylenes.^[256] The most probable reason for this observation is due to the bulkiness of the porphyrin ring.

Examples of the absorption of poly(ZnETPP)-co-(PE) copolymers are also shown in Figure 3.9b. These absorption spectra are nearly identical to the ZnETPP monomer and ZnTPP, suggesting that the incorporation of phenyl pendants limits the interaction of porphyrin rings reducing the excitonic coupling. The change in the copolymer ratio has little effect on the absorption properties, with nearly identical molar absorption coefficients after adjustment for chromophore concentration. The peak positions were also nearly identical. The absorption of the acetylenic backbone is again hidden by the absorption of the porphyrin π -system.

The absorption of the poly(ZnETPP)-co-(PEOXAD) copolymer is shown in Figure 3-9c. The spectrum shows the characteristic absorption of ZnTPP with a small decrease in the molar absorption coefficient of the Soret absorption transition when compared to the corresponding poly(ZnETPP)_{0.5}-co-(PE)_{0.5} copolymer. The Soret shows a 5 nm shift to lower energy, indicating electronic interaction between the co-monomers which results in a stabilization of the excited state. The Q-bands also show a similar red-shift. The strong band at 300 nm is attributed to the absorption of the oxadiazole moiety, shown in Figure 3-10.

The absorption spectrum of the poly(ZnETPP)-co-(3,5CF₃PE) is shown in figure 3.9d. The Soret shows a slight increase in intensity, when compared to the poly(ZnETPP)_{0.5}-co-(PE)_{0.5} copolymer suggesting that the chromophore concentration may be higher than expected. The position of the Soret shows a slight shift to lower energy. The Q-bands also show this bathochromic shift, suggesting electronic interactions with the other co-monomer resulting in stabilization of the excited state.

The absorption of the polymers studied show that there is little effect from the main chain and that polymerization has little effect on the overall absorption of the system, with the exception of the homopolymer poly(ZnETPP). This polymer has strong evidence of excitonic coupling and that incorporation of any co-monomer into the polymer chain lessens this interaction.

Table 3.2. Photophysical data.

Polymer	Quantum Yield*	Absorption, nm (ϵ , M ⁻¹ cm ⁻¹)	Emission (solution), nm	Emission (Film), nm
Poly(ZnETPP)	0.010	408(54840), 428(37058), 548(4840), 588 (888)	609, 655	621, 663
Poly(ZnETPP) _{0.15} -co-(PE) _{0.85}	0.029	420 (56250), 548 (3037), 588(608)	601, 650	613, 658
Poly(ZnETPP) _{0.5} -co-(PE) _{0.5}	0.032	420 (176250), 548 (9515), 586 (1900)	597, 646	617, 662
Poly(ZnETPP) _{0.5} -co-(PEOXAD) _{0.5}	0.031	306(49280), 425 (150850), 554 (13100), 599 (6170)	611, 657	**
Poly(ZnETPP) _{0.5} -co-(3,5CF ₃ PE) _{0.5}	0.034	422 (222710), 551(19675), 592 (5190)	613, 659	---

* Measured in reference to ZnTPP (0.033), ** Poly(ZnETPP)_{0.5}-co-(PEOXAD)_{0.5} non emissive in solid state.

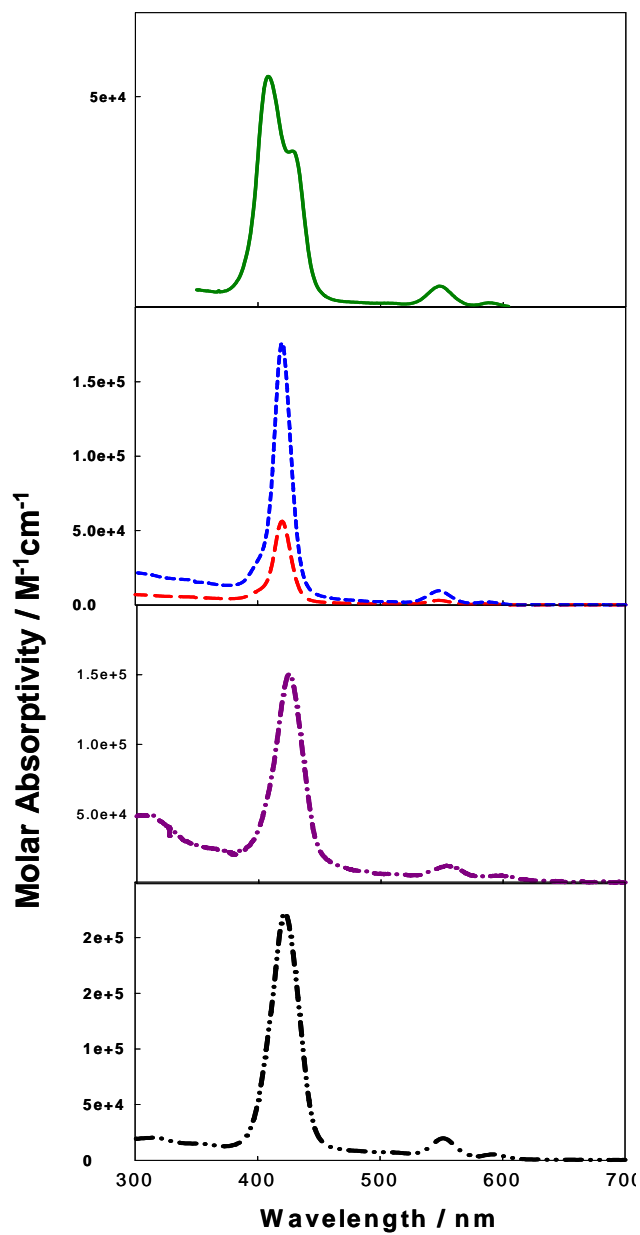


Figure 3-9. Absorption spectrum of (a) poly(ZnETPP) (—), (b) poly(ZnETPP)_{0.14}-co-(PE)_{0.86} (---), poly(ZnETPP)_{0.5}-co-(PE)_{0.5} (---), (c) poly(ZnETPP)_{0.5}-co-(PEOXAD)_{0.5} (—•—), and (d) poly(ZnETPP)_{0.5}-co-(3,5CF₃PE)_{0.5} (—••—).

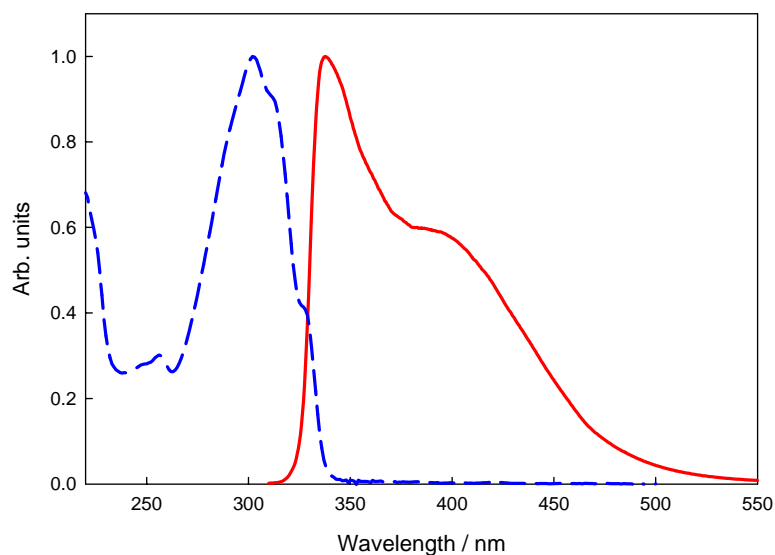


Figure 3-10. Absorption and fluorescence spectrum of PEOXAD monomer.

Emission

All emission experiments were carried out as dilute toluene solutions unless otherwise stated. Quantum yields were measured against the standard ZnTPP in toluene (0.033). The homopolymer poly(ZnETPP) showed emission, in solution, nearly identical in shape and position to that of ZnTPP. The only significant difference was the drop in quantum efficiency (0.01). This can be attributed to the excitonic coupling model suggested earlier, which increases the non-radiative decay rate. Emission in a spin coated film shows a slight bathochromic shift with respect to solution. This observation is understandable due to increased aggregation in the solid state. Figure 3-11a shows the emission of poly(ZnETPP) in solution and the solid state (thin film).

Figure 3-11b show the emission of the copolymers of poly(ZnETPP)-co-(PE). The incorporation of phenyl pendants on the polymer drastically reduce the fluorescence quenching due to excitonic coupling. The overall percent of PE incorporation seems to have little effect on the overall quantum efficiency. Several different copolymers,

ranging from 5% to 95% PE were prepared with almost identical, within experimental error, quantum efficiencies (see Table 3-2). The overall peak position and peak shapes are also nearly identical. As with the homopolymer, there exists a shift to lower energy of the emission peak in the solid state.

The emission spectrum of the copolymer with the oxadiazole moiety is shown in Figure 3.11c. The incorporation of PEOXAD has little effect on the overall quantum yield of the system. The peak shape of the porphyrin emission is slightly different with respect to ZnTPP, but not enough to draw any valid conclusions. The peak positions are slightly red-shifted (~ 10 nm) with respect to ZnTPP, suggesting electronic interaction in the excited state. The only other significant change in the overall emission properties of the system, in solution, is the emergence of a high energy emission band, centered at 350 nm (see Figure 3-10) when excited at high energy ($\lambda_{\text{ex}} = 300$ nm). The system was nearly non-emissive in the solid state, suggesting a ground state electron transfer occurring in the complex. The ΔG for this electron transfer can be calculated using:

$$\Delta G = E_{1/2}(\text{por} / \text{por}^+) - E^0(\text{ox} / \text{ox}^-) - E_{0-0} \quad (3.2)$$

where $E_{1/2}(\text{por} / \text{por}^+)$ is the oxidation potential of the porphyrin, $E^0(\text{ox}/\text{ox}^-)$ is the reduction potential of the oxadiazole moiety, and E_{0-0} is the zero-phonon energy absorption of the porphyrin complex. Given the values of 0.51 eV for the oxidation potential for the porphyrin, -1.47 eV^[257] as the reduction potential for the oxadiazole moiety, and 2.1 eV as the zero-phonon energy of the ZnTPP complex in the solid state, the calculation yields a $\Delta G = -0.12$ eV. This suggests that the electron transfer is energetically favorable, causing the non-emissive solid state.

The emission of the copolymers with the electron withdrawing CF₃PE monomer, are shown in Figure 3-11d. The emission properties, in solution, are again nearly identical to that of the reference, ZnTPP. The emission of these copolymers is also red-shifted, giving further evidence that electron withdrawing groups on the polymer have an effect on the porphyrin excited state. This suggests that the polymer backbone plays a role in the overall electronic properties of the system. Some broadening of the emission peaks is also evident. This may be caused an aggregate present in solution.

Thermally Induced Isomerization

Thin films of poly(ZnETPP) were prepared by spin-coating a solution onto a glass substrate. The films were then placed in a vacuum oven at 150°C for a fixed period of time, and then the emission properties were measured. Figure 3-12 shows the emission of thin films of poly(ZnETPP) as a function of annealing time. The unannealed film shows little emission and no evidence of emission from the polyacetylene backbone. Upon heating for 90 minutes, the appearance of a new band growing in at 510 nm suggests the beginning of isomerization from the *cis* conformation to the *trans* conformation. Upon heating for 3 hours the emission at 510 nm is significantly stronger, as is the emission of the porphyrin. The enhanced emission of the polymer can possibly be attributed to Förster energy transfer. This energy transfer can occur due to the fact that the absorption of the porphyrin Q-bands have significant overlap with the emission of the polyacetylene backbone. The film shows a further enhancement of both the backbone as well as the porphyrin emission after heating for 24 hours. This *cis* to *trans* isomerization has been observed for other singly functionalized polyacetylenes.^[194, 258-264]

The mechanism of this transformation involves bond scission and rotation.

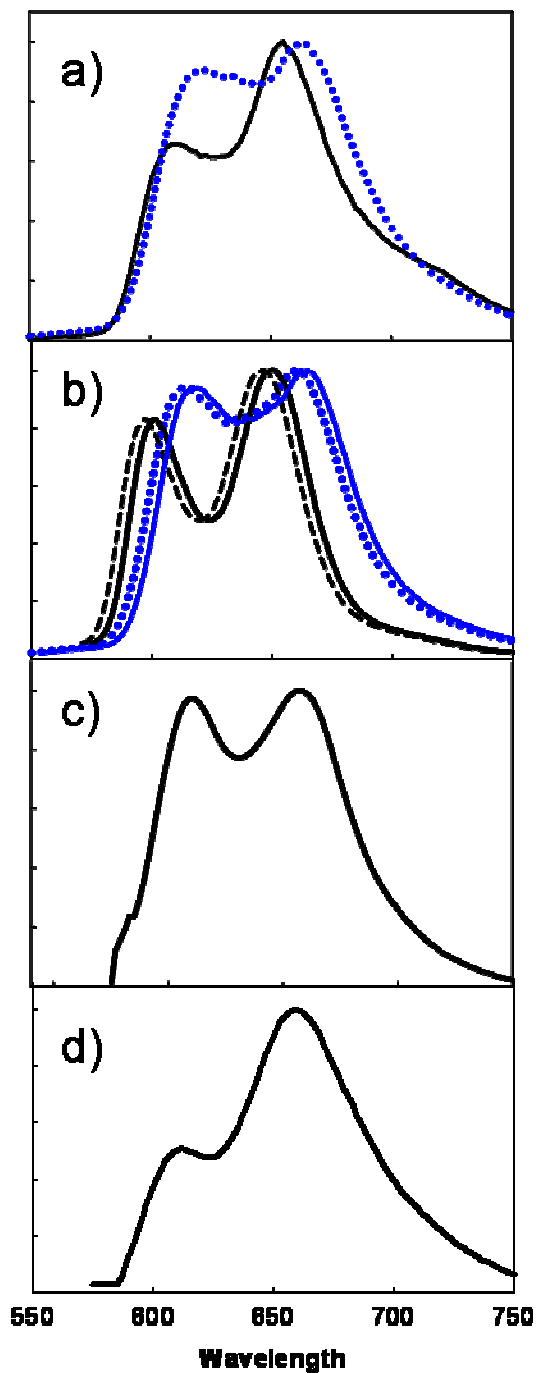


Figure 3-11. a) Emission ($\lambda_{\text{ex}} = 420 \text{ nm}$) of poly(ZnETPP) in solution (—), film (•••), (b) poly(ZnETPP)_{0.14}-co-(PE)_{0.86} in solution (—), film (•••) (---), poly(ZnETPP)_{0.5}-co-(PE)_{0.5} in solution (---), film (—), (c) poly(ZnETPP)_{0.5}-co-(PEOXAD)_{0.5} in solution (—), and (d) poly(ZnETPP)_{0.5}-co-(3,5CF₃PE)_{0.5} in solution (—).

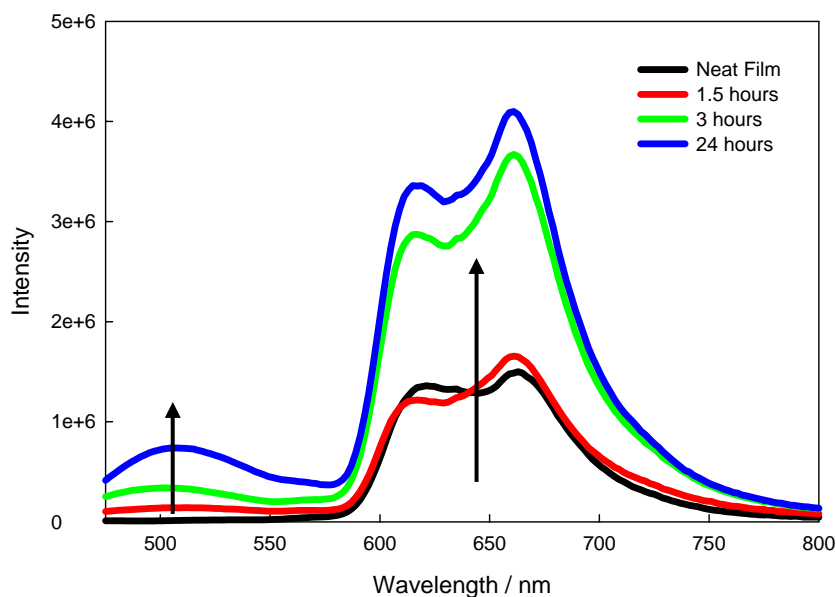


Figure 3-12. Emission of poly(ZnETPP) in film as a function of annealing time at 150° C in vacuum. Intensity increases as a function of annealing time.

Light Emitting Devices

Light emitting diodes were fabricated with the polymers, by spin-coating the polymer solution neat or in a blend with the non-conjugated polymer polystyrene. Figure 3.13a shows the current density – voltage and irradiance – voltage curves for poly(ZnETPP). The neat polymer showed a turn on voltage of 10 V but showed almost no electroluminescence emission. Figure 3.14 shows the emission spectrum of the polymer in the device. The addition of 1 mg of polystyrene, (25 wt%), caused a dramatic increase in irradiance, as well as an increase in the current density. The devices also show a turn on voltage of 4 V. This can be explained by the earlier discussed excitonic coupling model. This excitonic coupling acts as a trap causing the lowered current, as well as lowered emission. The addition of polystyrene acts to dissociate the excitonic state, by reducing the interaction of individual porphyrin pendant molecules. The addition of increased amounts of polystyrene had little additional effect on the overall properties.

The overall current density of the system was extremely high with a current density of 1 A/cm² at 12 V. The irradiance was fairly low for porphyrin based devices and results in only 1.2 μW/cm², which is over an order of magnitude lower than devices fabricated from ZnTPP blended into polystyrene (18 μW/cm²). The external quantum efficiency (photons emitted / electrons injected) is shown in figure 3.16a. Given the fact that the emission is based on current injected and photons collected, the external quantum efficiency of the neat polymer was extremely low ($< 1 \times 10^{-6}$). The addition of polystyrene induces an order of magnitude increase in the quantum efficiency. This is still approximately one order of magnitude lower than similar devices fabricated from porphyrin based complexes.^[31, 265-268] There are several possibilities for the high current densities found in this system. The first is the high hole mobility of the polyacetylene main chain. The second major cause of the high current densities was the presence of rhodium nanoparticles formed by Joule heating during device operation. This rhodium comes from the catalyst that remains attached to the polymer chain at the termination of the polymerization. TEM images confirmed the presence of these particles (Figure 3-15).

Figure 3.13b shows the current density – voltage and irradiance – voltage curves for the copolymer poly(ZnETPP)_{0.5}-co-(PE)_{0.5}. The neat polymer shows a further increase in current density, passing 1.5 A/cm² at 12 V, and a maximum irradiance of 1 μW/cm². The addition of 1 mg of polystyrene, (25 wt%), caused a 1/3 decrease in the current density as well as a 1/3 increase in maximum irradiance. There are two possible suggestions for this finding; the first is that there was still aggregation in the solid state and that the addition of polystyrene acted to reduce the amount of aggregation, or the polystyrene was acting as a carrier blocker (mainly holes), minimizing the amount of

intra-chain carrier transport as well as reducing the amount of holes reaching the cathode interface and the resultant annihilation. All devices turned on at approximately 4 V. Figure 3.16b shows the external quantum efficiency as a function of current density. These devices showed a maximum external quantum efficiency of 1.5×10^{-5} , which was nearly identical to devices created from blends of PS with the poly(ZnETPP) homopolymer. The emission of the copolymers is shown in Figure 3.14 and the peak position is slightly red-shifted with respect to the parent complex in solution. The relative intensities of the high energy peak to that of the low energy peak are also different, when compared to that of the polymer in solution. In electroluminescent devices, the high energy peak is significantly less intense as compared to the solvated polymer.

Figure 3.13c shows the current density – voltage and irradiance – voltage curves for poly(ZnETPP)_{0.5}-co-(PEOXAD)_{0.5}. In this system the current density for the neat polymer was nearly one order of magnitude lower than that of the homopolymer or of copolymers with PE. This change was attributed to two factors. The first factor is the hole blocking ability of the oxadiazole moiety, and the second is the electron transport capability of oxadiazole group. The former is the most reasonable due to the fact that the current density decreased by nearly an order of magnitude but the irradiance showed very little increase. This suggests that the oxadiazole is blocking holes from reaching the electrode interface, therefore limiting “non-active” carriers. The addition of polystyrene further lowered the current density and increased the irradiance, suggesting that further blocking of holes was occurring, allowing for more efficient devices. Figure 3.16c shows the external quantum efficiency as a function of current density. The devices with

polystyrene showed an order of magnitude increase in efficiency, putting these devices on magnitude with ZnTPP based devices (3×10^{-4}). The EL emission spectrum for the polymer is shown in Figure 3.14. There was a significant blue-shift in the emission spectrum (~ 20 nm).

Figure 3.13d shows the current density – voltage and irradiance – voltage curves for the copolymer poly(ZnETPP)_{0.5}-co-(3,5CF₃PE). The current density was similar to devices fabricated with the homopolymer as well as with the copolymers containing PE. The major difference was the dramatic increase in the irradiance. The irradiance increased by an order of magnitude from devices fabricated with the other copolymers. This can be explained by the presence of the electron withdrawing trifluoromethyl groups present in the polymer. These groups helped to enhance electron transport within the polymer and therefore accounted for more exciton recombination on the active chromophore (the porphyrin). The addition of polystyrene had little effect on the current density or the irradiance, and therefore the data is not shown. The external quantum efficiency as a function of current density is shown in Figure 3.16d. The results were similar to the devices fabricated with the copolymer containing the oxadiazole group. This suggests that the addition of electron transporting / hole blocking groups further enhanced the devices properties. The EL emission spectrum for the copolymer is shown in Figure 3.14. The emission was also blue-shifted ~ 20 nm with respect to the solvated polymer.

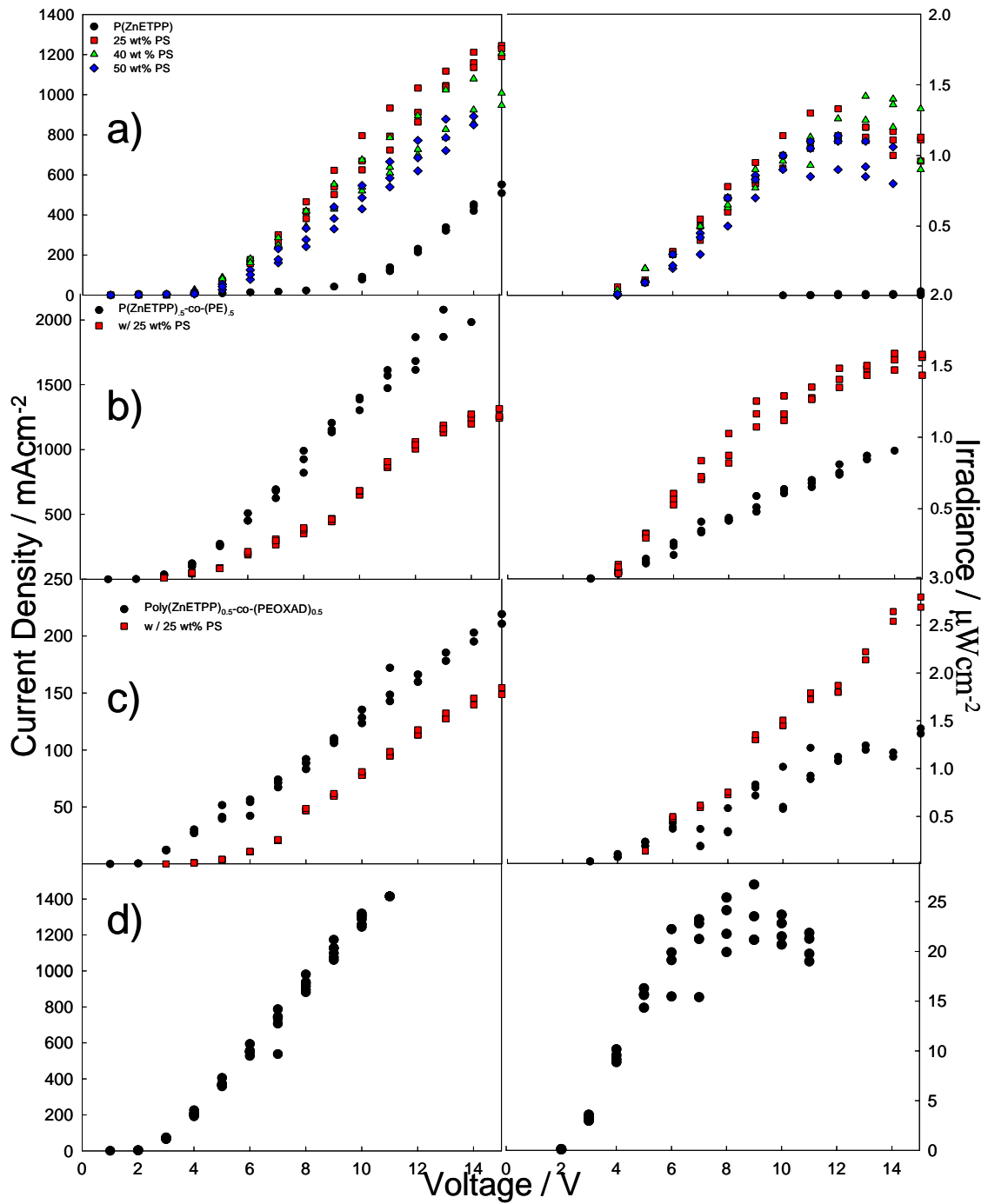


Figure 3.13. Current density vs. voltage and irradiance vs. voltage for a) poly(ZnETPP) b) poly(ZnETPP)_{0.5}-co-(PE)_{0.5}, c) poly(ZnETPP)_{0.5}-co-(PEOXAD)_{0.5} d) poly(ZnETPP)_{0.5}-co-(3,5CF₃PE)_{0.5} as a function of wt% of polystyrene.

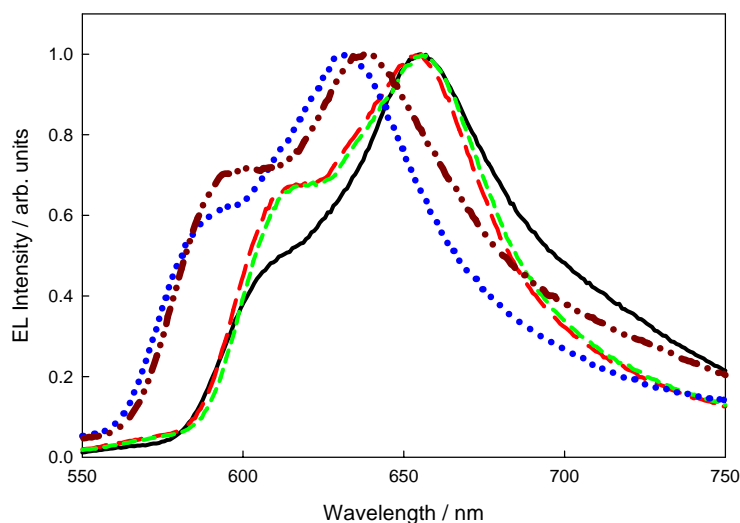


Figure 3-14. Electroluminescence emission of spectrum of poly(ZnETPP) (—), (b) poly(ZnETPP)_{0.14}-co-(PE)_{0.86} (---), poly(ZnETPP)_{0.5}-co-(PE)_{0.5} (---), (c) poly(ZnETPP)_{0.5}-co-(PEOXAD)_{0.5} (•••), and (d) poly(ZnETPP)_{0.5}-co-(3,5CF₃PE)_{0.5} (—••—).

Table 3-3. Electroluminescence data.

Active Layer	Turn on (V)	Max EL Efficiency	Peak Current Density (mAcm ⁻²)	Peak Irradiance (μWcm ⁻²)	Peak Radiance (cdm ⁻²)
Poly(ZnETPP)	10	1.6×10^{-6}	962	0.06	0.2
Poly(ZnETPP)75% / PS 25%	4	1.1×10^{-5}	1287	1.33	3.5
Poly(ZnETPP)60% / PS 40%	4	1.5×10^{-5}	1329	1.43	3.7
Poly(ZnETPP)50% / PS 50%	4	1.8×10^{-5}	900	1.15	3
Poly(ZnETPP) _{0.5} -co-(PE) _{0.5}	3	3.3×10^{-6}	2079	0.9	2.3
Poly(ZnETPP) _{0.5} -co-(PE) _{0.5} 75%/ PS 75%	4	1.9×10^{-5}	1570	1.66	4.4
Poly(ZnETPP) _{0.5} -co-(PEOXAD) _{0.5}	4	5.1×10^{-5}	286	2.5	6.5
Poly(ZnETPP) _{0.5} -co-(PEOXAD) _{0.5} 75% / PS 25%	4	3.0×10^{-4}	162	3.1	8.1
Poly(ZnETPP) _{0.5} -co-(3,5CF ₃ PE) _{0.5}	4	2.9×10^{-4}	1414	26.7	69.4

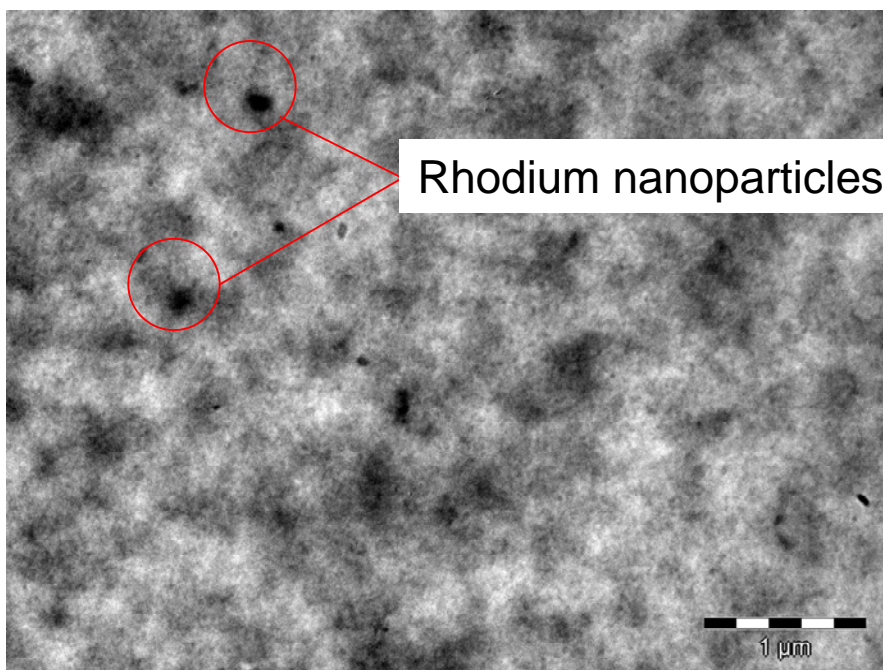


Figure 3-15. TEM image of poly(ZnETPP) showing presence of Rh nanoparticles

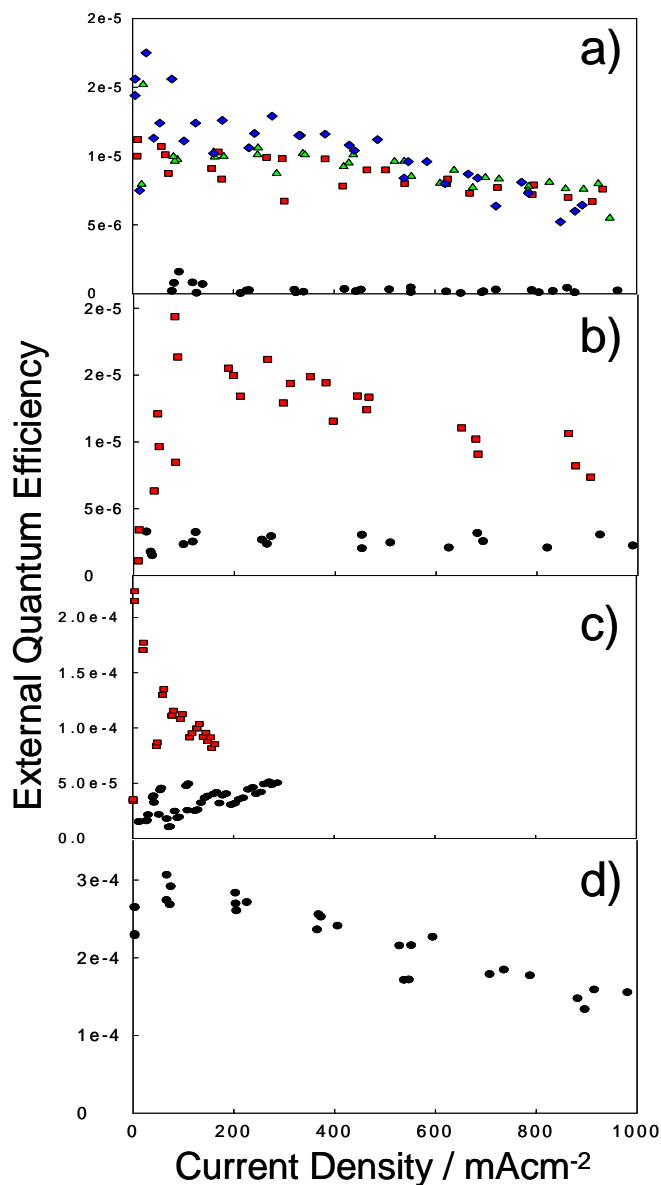


Figure 3.16. External quantum efficiency vs. current density for a) poly(ZnETPP) b) poly(ZnETPP)_{0.5}-co-(PE)_{0.5}, c) poly(ZnETPP)_{0.5}-co-(PEOXAD)_{0.5} d) poly(ZnETPP)_{0.5}-co-(3,5CF₃PE)_{0.5} as a function of wt% of polystyrene (● = 0 wt%), (■ = 25 wt%), (▲ = 40 wt%) and (◆ = 50 wt%) .

Discussion

The photoluminescent and electroluminescent properties of mono- and di-substituted polyacetylenes typically is dependant on emission from the backbone of the polymer, and pendant groups act to increase the conjugation. This is not the case for the

polymers fabricated using the ZnETPP monomer. This is most likely caused by the break in conjugation at the phenyl group of the porphyrin. This allows the porphyrin based polymers to act as an independent chromophore. Therefore the optical and electroluminescent properties act more like ZnTPP than typical polyacetylenes. Several groups have produced polyacetylenes and have tested their electroluminescent properties. The EL emission is typically in the blue or green regions of the spectrum, depending on the substituents. The Epstein group fabricated devices using di-substituted polyacetylene which contained a carbazole pendant group which showed emission centered around 550 nm with high current densities (1 A / cm^{-2}) for 100 nm thick films.^[232] The high hole mobility and low external EL efficiency mirrors devices fabricated using poly(ZnETPP) polymers. This suggests that devices fabricated using polyacetylenes tend to have poor device performance, mainly due to the high conductivity of the main chain.

Conclusions

A large series of polymers containing the porphyrin pendant acetylene monomer were fabricated. All of the polymers exhibited high molecular weights, with adequate to poor solubility in most common organic solvents. Evidence suggested that the homopolymer exhibited a great deal of excitonic coupling resulting in low emission yield, both in solution and in solid-state devices. The incorporation of a phenyl pendant into the polymer reduced this coupling and therefore increased the photoluminescent quantum yield similar to that on ZnTPP. This suggested that the polyacetylene chain had only a minor effect on the photoluminescent properties and that the major emissive properties are due to the porphyrin pendant. Devices fabricated with these polymers were inefficient due to the high hole mobility present. This could be drastically reduced by incorporation of hole blocking or electron transporting groups appended to the polymer.

These groups acted to reduce the total number of holes or to increase the total number of electrons within the active layer. These devices fabricated with the electron deficient groups were on par with devices fabricated with ZnTPP. As also seen in the previous chapter, the major flaw found in devices fabricated with porphyrin pendant polymers, is the lack of carrier balance. The problem of Rhodium contamination also contributed to poor device performance.

Experimental

Monomer Synthesis

All reagents and solvents were obtained from Fisher, Aldrich, Strem, or GFS, were reagent grade, and were used as received unless noted otherwise. Substituted porphyrin synthesis was achieved with significant help from Fengqi Guo.

4-(3-methyl-3-hydroxybut-1-yn-1-yl)benzaldehyde (1). Following a standard procedure,^[269] samples of 4-bromobenzaldehyde (17.40 g, 93 mmol), Pd(PPh₃)₄ (1.136 g, 2.2 mmol), and CuI (102 mg, 0.5 mmol) were placed in a Schlenk flask. The flask was then purged with argon several times. Freshly distilled and degassed triethylamine (50 mL) was added. After again purging with argon, 2-methylbut-3-yn-2-ol (11 mL, 112 mmol) was added. The reaction mixture was stirred for 6 hours at 40° C. Column chromatography (silica, CH₂Cl₂) of the crude reaction mixture followed by bulb-to-bulb distillation afforded a pale yellow oil (16.5 g, 93%): ¹H NMR (CDCl₃) δ 1.62 (s, 6H), 2.21 (broad s, 1H), 7.52 (2H), 7.81 (2H), 9.02 (s, 1H); ¹³C NMR δ 31.9, 66.1, 81.9, 98.8, 129.8, 130.1, 132.7, 135.9, 192.3.

5-[4-(3-methyl-3-hydroxy-1-butyn-1-yl)phenyl]-10,15,20-triphenylporphyrin (2). Following a standard procedure,^[61] a solution of 4-(3-methyl-3-hydroxybut-1-yn-1-yl)benzaldehyde (1) (2.75 g, 14.6 mmol), benzaldehyde (4.6 mL, 44 mmol), and pyrrole

(4.0 mL, 58 mmol) in CHCl_3 (800 mL) was treated with $\text{BF}_3 \cdot \text{OEt}_2$ (1.8 mL, 14 mmol). The mixture was stirred at room temperature for 1.5 hours under argon. Then, a solution of DDQ (12 g, 53 mmol) in THF (100 mL) was added, and the mixture stirred for 1 hour in air. The mixture was concentrated to one-fourth of the original volume and passed over a silica plug (CH_2Cl_2). The resulting porphyrins were chromatographed [silica, CH_2Cl_2 /hexanes (1:1)]. A second chromatography column [silica, CH_2Cl_2 /hexanes (1:5)] afforded pure compound (1.21 g, 16 %): $^1\text{H NMR}$ (CDCl_3) δ -2.53 (s, 2H), 1.56 (s, 6 H), 2.1 (s, 1 H), 7.5 – 7.7 (m, 11 H), 8.1 – 8.3 (m, 8 H), 8.6 – 8.8 (m, 8 H); λ_{abs} (CH_2Cl_2) 419, 514, 550, 591, 646 nm.

5-(4-ethynylphenyl)-10,15,20-triphenylporphyrin (3).^[243] A solution of **2** (0.6 g, 0.78 mmol) in toluene (50 mL) was treated with powdered NaOH (0.5 g, 12.5 mmol) and the reaction mixture was refluxed for 4 hours. After cooling the reaction mixture was directly poured onto a dry silica pad. The product was eluted with toluene (0.495 g, 92 %): $^1\text{H NMR}$ (CDCl_3) δ -2.57 (s, 2H), 3.3 (s, 1 H), 7.5 – 7.7 (m, 11 H), 8.1 – 8.3 (m, 8 H), 8.6 – 8.8 (m, 8 H).

Zn(II)-5-(4-ethynylphenyl)-10,15,20-triphenylporphyrin (4).^[243] A solution of **3** (0.25 g, 0.39 mmol) in CH_2Cl_2 was treated with a solution of $\text{Zn}(\text{OAc})_2 \cdot 2\text{H}_2\text{O}$ (1.15 g, 5.24 mmol) in methanol (20 mL). The mixture was stirred overnight at room temperature and poured into aqueous NaHCO_3 . The organic layer was dried, filtered, and chromatographed [silica, CH_2Cl_2 / hexanes (1:1)] to afford the title product (0.25 g, 92% yield): $^1\text{H NMR}$ (CDCl_3) δ 3.3 (s, 1 H), 7.4 – 7.6 (m, 11 H), 8.0 – 8.2 (m, 8 H), 8.6 – 8.8 (m, 8 H).

4-bromobenzhydrazide (5).^[245] A mixture of methyl-4-bromobenzoate (5g, 33 mmol) and hydrazine monohydrate (6 mL, 120 mmol) were refluxed for 24 hours in 100 mL of ethanol. After the reaction was complete, the mixture was cooled to room temperature, and poured into ice water to precipitate the white solid, which was collected on a filter and washed with hexane to remove the unreacted starting materials. The resulting product was dried in a vacuum oven for 24 hours. The product yield was 90 % (4.75 g): ¹H NMR (D6-DMSO) δ 4.53 (broad s, 2H), 7.67 (m, 2 H), 7.75 (m, 2 H), 9.86 (s, 1H).

2-(4-bromophenyl)-5-(4-methyl)-1,3,4-oxadiazole (6).^[245] 1.0 g (7.3 mmol) or 4-methyl benzoic acid was added to 20 mL of oxalyl chloride and refluxed for 2 hours to give 4-methylbenzoyl chloride. The excess oxalyl chloride was removed by vacuum distillation and the reaction mixture was cooled to room temperature. After 30 minutes, 1.57 g (10 mmol) of 4-bromobenzylhydrazide dissolved in 20 mL of pyridine were added to the reaction flask through a dropping funnel over a period of 20 minutes. After stirring for 2 hours, the reaction mixture was poured into distilled water. The product was collected on filter paper and subsequently placed into a round bottom flask and POCl₃ (20 mL) was added. The mixture was refluxed for 6 hours under an argon atmosphere. After the completion of the reaction, the reaction mixture was slowly poured into cold water in an ice bath and 0.5 M NaOH solution was added to neutralize the reaction mixture. The precipitate was collected on a filter, washed with distilled water, and recrystallized from ethanol/water (3:1 v/v). The product was a white solid with a yield of 65% (1.14 g) ¹H NMR (d6-DMSO) δ 1.7 (s, 3 H), 7.7 – 7.8 (m, 8 H).

4-2-(4-(3-methyl-3-hydroxy-1-butyn-1-yl)phenyl)-5-(4-methyl)-1,3,4-oxadiazole (7).^[245] 2-(4-Bromophenyl)-5-(4-methyl)-1,3,4-oxadiazole (0.6 g, 2 mmol) was added to a Schlenk flask containing 10 mL DMF, 20 mg Pd(PPh₃)₂Cl₂, 20 mg CuI, and 20 mg PPh₃. The solution was degassed with argon for 30 minutes. 10 mL of freshly distilled and degassed triethylamine was added and the solution was again degassed for 30 minutes. 1 mL of 2-methyl-3-butyn-2-ol was added and the reaction was stirred at 50° for 4 hours under argon atmosphere. After completion of the reaction, the mixture was cooled to room temperature. The ammonium salt and other insoluble materials were removed by filtration. The product was purified by column chromatography [silica, hexane/ethyl acetate (1:1)] to yield a yellow-white solid (0.48 g, 81% yield): ¹H NMR (CDCl₃) δ 1.4 (s, 3 H), 1.6 (s, 6 H), 2.3 (broad s, 1 H), 7.6 – 8.1 (m, 8 H).

2-(4-methylphenyl)-5-(4-ethynylphenyl)-1,3,4-oxadiazole (8).^[245] A mixture of compound 7 (0.4 g, 1.5 mmol) and NaH (0.2 g, 8.3 mmol) was refluxed for 1 hour in 20 mL of toluene. The reaction was then allowed to cool to room temperature and the unreacted NaH was quenched by the addition of isopropanol. The product was extracted with diethyl ether several times. The product was purified by column chromatography [silica, hexane/ethyl acetate (1:1)] and subsequently dried in a vacuum oven for 24 hours. The yield was 0.25 g (70%): ¹H NMR (CDCl₃) δ 1.4 (s, 3 H), 3.3 (s, 1 H), 7.5 – 8.1 (m, 8 H).

Polymerization

The homopolymerization of **4** as well as the copolymerization of **4** with ethynylbenzene, **8**, and (5-ethynyl)-1,3-(trifluoromethyl)benzene was carried out using a commercially available (bicyclo[2,2,1]hepta-2,5-diene)rhodium(I) dimer [Rh(NBD)Cl]₂ (Aldrich) as a catalyst.^[242] The ratio of the monomers to the catalyst was maintained at (100:1)

respectively. The monomers were dissolved in 1 mL of CHCl_3 in an argon atmosphere for 30 minutes. In a separate reaction vessel the catalyst was dissolved in 0.5 mL of CHCl_3 along with 100 equivalents of triethylamine (~ 0.2 mL) also under an argon atmosphere and stirred for 30 minutes. The catalyst solution was then added at once via syringe to the monomer solution. The monomer solution was then allowed to stir at room temperature for 36 hours. The crude polymers were then purified by precipitation from CHCl_3 / acetone several times. The resulting polymers ranged in color from deep purple to light red. The molecular weight was determined via gel permeation chromatography (THF) with respect to polystyrene standards. All polymers showed a unimodal pattern in the elution diagram determined by GPC. The results of the polymerization are summarized in table 3.1. The copolymer ratios were determined by NMR.

Thermogravimetric Analysis

TGA thermograms were taken using a Perkin Elmer TGA-7 under an air atmosphere at a rate of 10°C / minute after holding at 40° for 30 minutes. The samples all weighed between 1.5 and 2.5 mg each.

Photophysical Measurements

All photophysical studies were conducted in 1 cm square quartz cuvettes unless otherwise noted. All absorption and emission measurements were made in toluene unless otherwise noted. Absorption spectra were obtained on a double-beam Cary-100 UV-visible spectrophotometer. Fluorescence spectra were measured on a SPEX Fluorolog-3 equipped with an air-cooled Hamamatsu R928 PMT for visible measurements. All measurements were corrected for detector response. Quantum yields were measured against $\text{Zn}(\text{TPP})$ in toluene ($\Phi = 0.033$).

Device Fabrication and Measurement

Devices were fabricated and tested as stated in the experimental section of Chapter 2.

CHAPTER 4 FUTURE DIRECTIONS

The previous chapters focused on the individual projects carried out during the dissertation research. This chapter is designed to provide insight into the bigger picture and to provide a future direction for this research project.

Non-Radiative Decay

Chapter two was devoted to functionalized ytterbium porphyrin complexes for use in light emitting diodes. It was concluded that there were two major problems with the overall molecular design. The first major deficiency is the large pathway for non-radiative decay through the coupling of the lanthanide excited state to the C – H bond phonon.^[270] This coupling leads to a dramatic decrease in the overall population of the excited state and therefore affects both photoluminescent and electroluminescent efficiencies. The second major problem is the inherently poor stability of the organic anion radical. This leads to the large imbalance in the overall carrier density and mobility allowing for inefficient devices. The first correction to this problem is to lower the phonon energy of the complex and therefore limit coupling with the excited state. As stated in Chapter 2, energy transitions which can be bridged by three or less phonons have large non-radiative decay rates. This can be accomplished by substitution of protons on the complex with atoms with higher atomic mass, in turn reducing the energy of the oscillation. There are several different methods to accomplish this substitution. The first is to exchange the protons for deuterium atoms. This would cause a significant shift of the vibrations to lower energy. Although this is possible, the starting materials are

prohibitively expensive, and the possibility of proton exchange with organic solvents exists. The substitution of the protons with halogens has been shown to increase the intersystem crossing rate, therefore increasing the triplet yield.^[271, 272] Halogenation has a twofold effect. It would reduce the energy of the phonon modes of the system as well as increase the electron affinity of the complexes. This increase in electron affinity is due to the electrophilic nature of the halogens which in turn reduce the electron density on the porphyrin macrocycle. This causes a stabilization of the LUMO of the complex. Halogens also cause a distortion of the planar nature of the complex which therefore destabilizes the HOMO. Terbium X₈TPP complexes have been made and the results show that halogenation causes a decrease in HOMO-LUMO gap and a large decrease in the energies of oxidation as well as reduction.^[273] These halogenations are currently synthetically challenging using the synthetic method referred to in Chapter 1, due to the fact that lithiation of halogenated organics has been shown to be somewhat unsafe. Alison Knefely has developed a method of lanthanide insertion into the porphyrin macrocycle using *tris* alkyl lanthanide complexes, which has shown promise alleviating this problem.

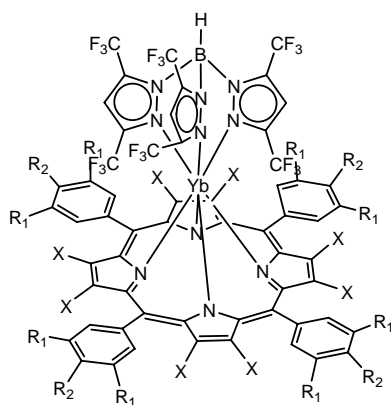


Figure 4-1. Molecule proposed to increase emission quantum yield. X represents a halogen and R represents organic groups or hydrogens.

Table 4-1. Vibrational frequencies of common bonds in organic molecules.

Bond	Bond Stretching Frequency (cm ⁻¹)
C-H	2900 - 3200
C=C	1450 - 1680
C=N	~1800
O-H	2500 - 3650
C-D	2200 - 2400
C-F	1100 - 1350
C-Cl	800 - 700
C-Br	700 - 500
C-I	< 500

Carrier Transport

The problem of poor carrier transport can be addressed in two methods. The first method is to append electron withdrawing groups (EWG) to the β positions of the porphyrin macrocycle. This was briefly touched upon earlier in this chapter with substitution of halogens. This process can also be carried out using other EWG's on the pyrroles. The most logical example would be the substitution of cyano groups. Cyano groups are known to be electron withdrawing and substitution at the β position on the porphyrin is known to cause a dramatic influence on the electronic properties of the system. This combination has been shown to cause a dramatic stabilization of the LUMO in porphyrins, inducing the first reduction to appear at positive values with respect to Fc/Fc^+ for tetracyano(tetraphenylporphyrin).^[274] The second method was discussed in Chapter three, where the porphyrin can be appended to a polymer chain which contains electron transporting moieties. This method was shown to be effective for ZnTPP appended to polyacetylene, but not for lanthanide substitute porphyrin due to synthetic challenges posed by the terminal acetylene. The lithiation step, required for lanthanide metallation, resulted in deprotonation of the terminal acetylene followed by indeterminate side reactions.

Porphyrin Containing Polymers

Although the previous processes may work, there are several other directions which can be undertaken to further enhance the overall efficiencies of devices created using lanthanide porphyrin complexes. The first is a combination of a conjugated polymer with the lanthanide porphyrin, where the porphyrin is part of the polymer backbone. Figure 4-2 shows an example combining the previously discussed solutions, by placing a β halogen or EWG substituted porphyrin into the main chain of a conjugated polymer, poly(phenylene ethynylene) (PPE), which also contains the electron transporting / hole blocking oxadiazole moiety.

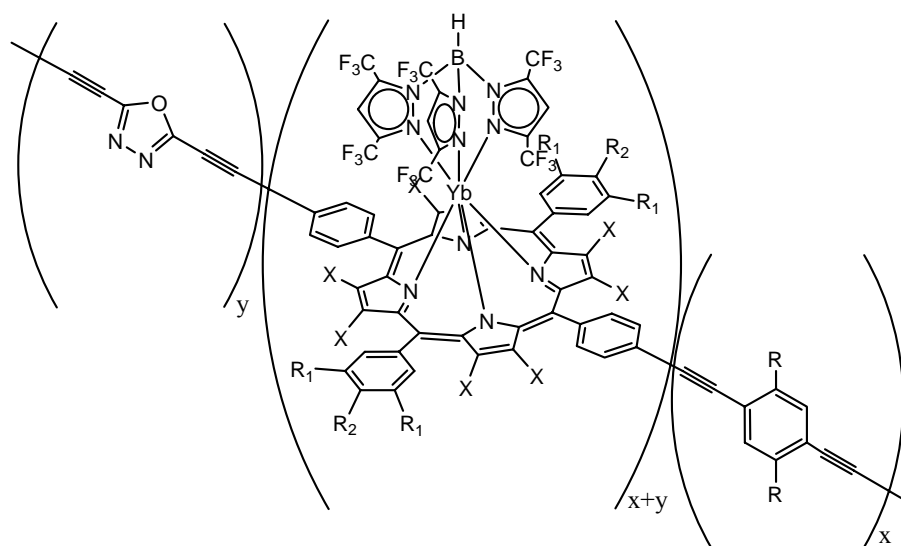


Figure 4-2. Conjugated polymer, PPE, containing substituted porphyrin and oxadiazole in main chain. R represents a solublizing alkyl or alkoxy ligand. X is a halogen or EWG.

A second possible future direction involves lanthanide porphyrins appended to non-conjugated polymers. These polymers are designed to reduce the aggregate properties of the complexes as well as to limit the conductivities associated with conjugated polymers. They are also designed to reduce phase segregation observed when porphyrins are blended with non-conjugated polymers. Several different polymers were synthesized

using free radical induced chain growth mechanism. A styrenyl lanthanide porphyrin was copolymerized with 4-*tert*-butyl styrene (TBS) and 2,2,2-trifluoroethylmethacrylate (TFEM) using 2,2'-azobisisobutyronitrile (AIBN). The resulting polymer contained ~ 1 mol % of the porphyrin species. The molecular weight was determined to be 200,000 by GPC. Absorption studies of the polymer show that the porphyrin Soret is observed but the Q-bands were too weak to detect. Fluorescence studies showed only weak fluorescence from the porphyrin with no lanthanide emission observed. Attempts to create a polymer with a higher concentration of the porphyrin species were unsuccessful.

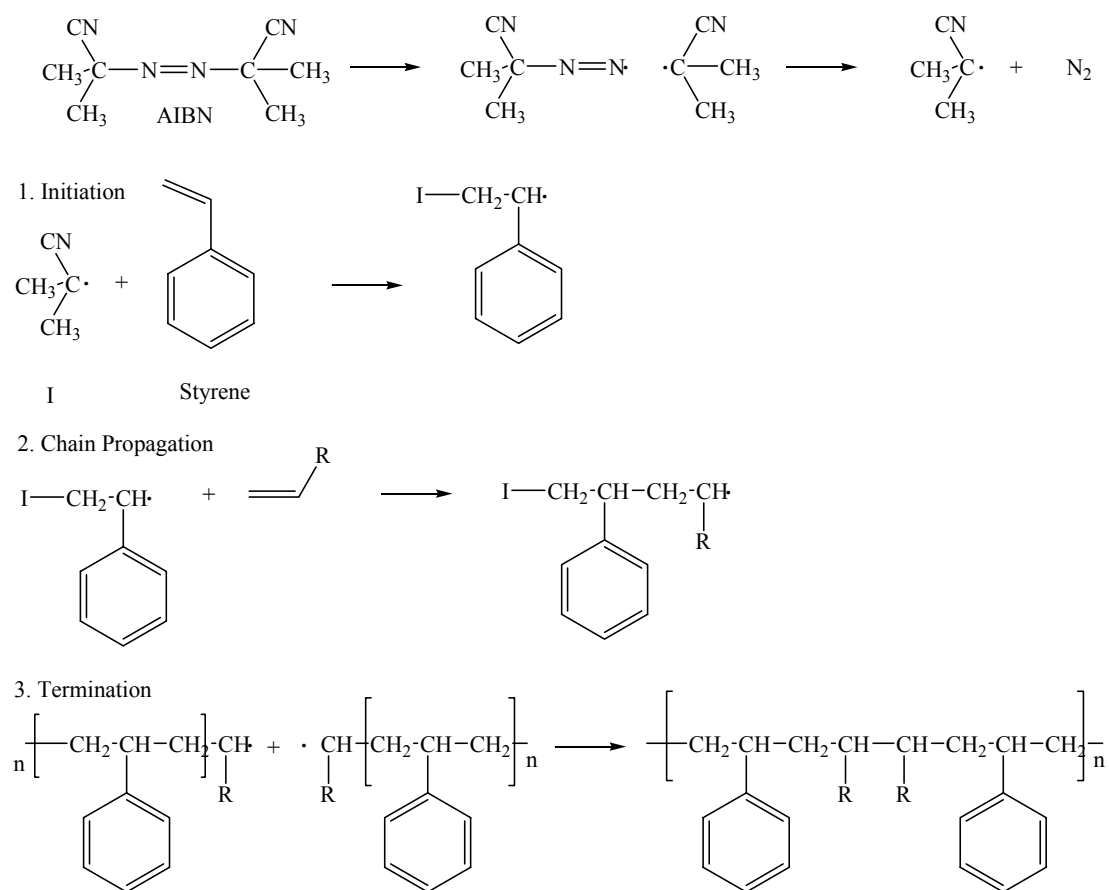


Figure 4-3. Scheme of a free radical chain growth mechanism.

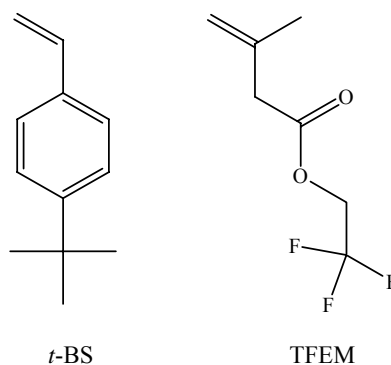


Figure 4-4. Structures of monomers.

Non-conjugated polymers containing the trispyrazole borate (Tp) units were synthesized by Prof. Frieder Jaekle's group in order to incorporate LnTPP complexes onto polymers. Alison Knefely appended the lanthanide porphyrin onto the polymer using the salt metathesis reaction discussed in Chapter 1. The resulting polymers were insoluble in most organic solvents with the exception to the slight solubility in *o*-dichlorobenzene. Molecular weights were indeterminate. Absorption studies performed in dichlorobenzene showed typical metallated porphyrin spectra with the Soret band ~ 423nm and three Q bands between 520 and 630nm. Emission studies showed Yb-emission ~980 nm emission of the $\text{Yb}^{3+} \text{}^2\text{F}_{5/2} \rightarrow \text{}^2\text{F}_{7/2}$ transition with weaker emission bands at lower wavelengths, which is attributed to the crystal field splitting of the $\text{Yb}^{3+} f$ -states by the axial and porphyrin ligands. Devices were not fabricated due to the poor solubility of the polymer complex. Incorporation of alkyl or alkoxy groups onto the porphyrin may help with the solubility issues of this polymer.

Conclusions

Although the major deficiencies of efficient non-radiative decay pathways and poor carrier transport in lanthanide porphyrin based near-infrared devices have been identified, the challenge still exists to help alleviate these problems. Progress has been made in the

form of polymers which contain electron withdrawing groups and polymers which reduce phase separation, but there is plenty of work to be done.

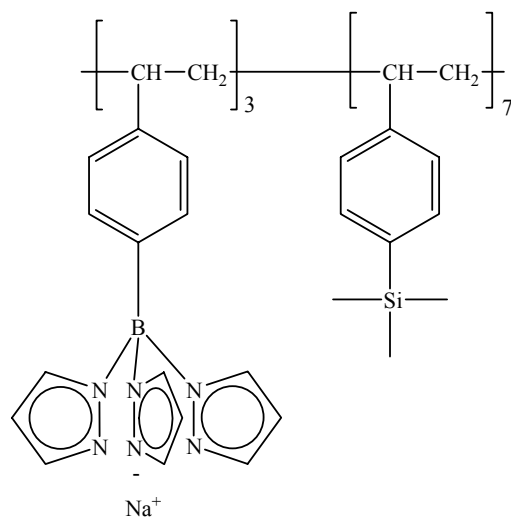


Figure 4-5. Structure of TP polymer.

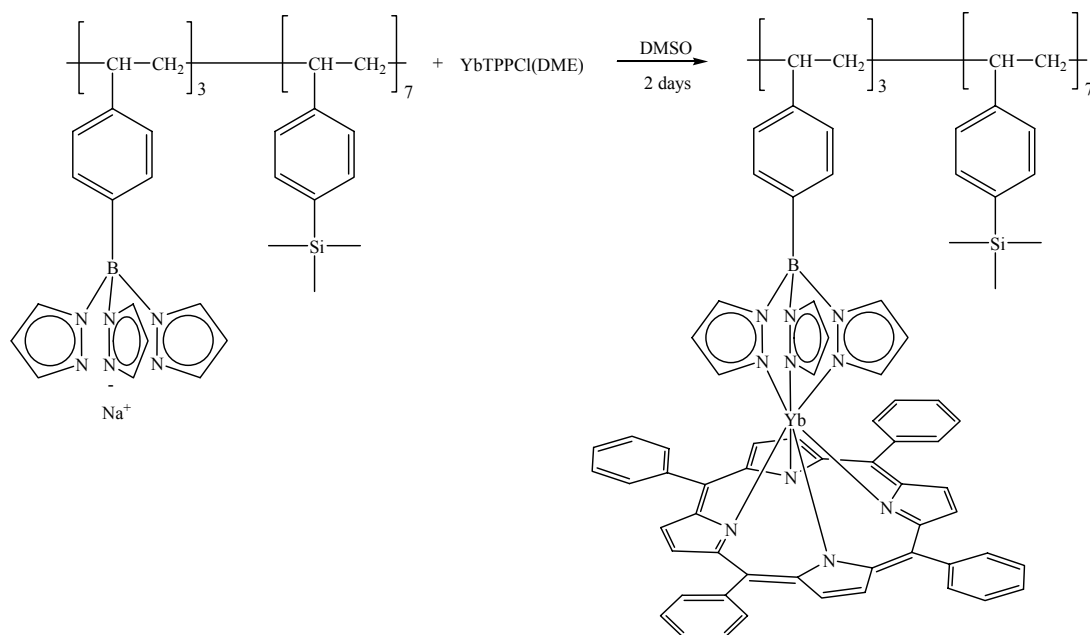


Figure 4-6. Synthesis of YbTPP-TP polymer.

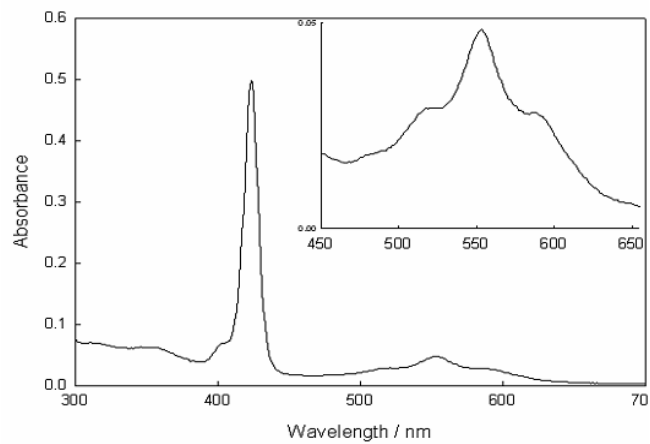


Figure 4-7. Absorption spectrum of YbTPP-TP polymer.

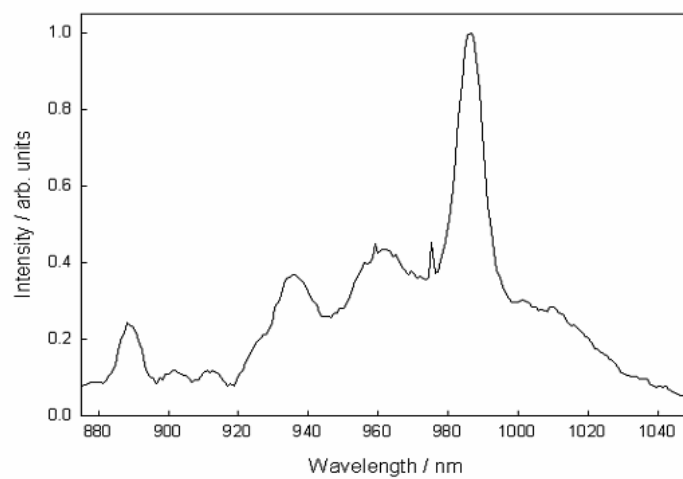


Figure 4-8. NIR emission spectrum of YbTPP-TP polymer. (RT, o-dichlorobenzene)

APPENDIX ELECTRONIC PROPERTIES

The theoretical prediction of the energy levels of a lanthanide metal complex is extremely complicated, if not impossible, because it is a many-body problem. The general approach to solving the problem is to separate it into three parts. The first part is to determine the wavefunctions and energy levels for the ions in a spherically symmetric environment using the quantum mechanics of many electron atoms. This is known as the free-ion problem. The second part of the problem involves calculating the energy levels of the metal ion in the static electric field produced by the metal ion nearest neighbors. This is called the crystal field problem. The final part of the problem involves the coupling of the metal's electronic states to the organic molecular states.

The Free-Ion Problem

Several approaches have been developed to determine the energy level structure of an isolated, multi-electron atom.^[275-278] These methods are covered in many different quantum mechanics textbooks.^[279-283] The following discussion is a brief review of the important concepts involved in the calculations.

The free-ion Hamiltonian, H_{FI} , for a multi-electron atom is given by

$$H_{FI} = \sum_{i=1}^n \left(\frac{p_i^2}{2m} - \frac{Ze^2}{4\pi\epsilon_0 r_i} + \zeta(r_i)(l_i \cdot s_i) \right) + \sum_{i>j} \frac{e^2}{4\pi\epsilon_0 r_{ij}} \quad (\text{A.1})$$

where the first summation is over the N electrons and the second summation is over the electron pairs, r_i is the position of the i^{th} electron, e is the electron charge, and m is the rest mass of an electron. There are four contributions to the full Hamiltonian. The first

term is the kinetic energy of the electrons expressed in terms of the momentum operator, p_i , and the electron mass. The second term is the potential energy of the electrons and a nucleus containing Z protons. The third term is the spin-orbit interaction and the last term is the inter-electron Coulomb interaction. To simplify the problem, the inter-electron Coulomb interaction is averaged over 4π radians to obtain a spherically symmetric potential that each electron experiences due to the other electrons. This is known as the central-field approximation. The Hamiltonian is now of the form

$$H_{FI} = \sum_{i=1}^n \left(\frac{p_i^2}{2m} + V_i'(r_i) + \zeta(r_i)(l_i \cdot s_i) \right) \quad (\text{A.2})$$

Where

$$V_i'(r_i) = -\frac{Ze^2}{4\pi\epsilon_0 r_i} + \left\langle \sum_{i \neq j} \frac{e^2}{4\pi\epsilon_0 r_{ij}} \right\rangle_{\theta, \phi} \quad (\text{A.3})$$

If the spin-orbit interaction is smaller than the inter-electronic Coulomb interaction (valid for atoms with low atomic numbers) the Russell-Saunders approximation can be applied and the spin-orbit interaction causes a splitting of the Russell-Saunders LS terms into J multiplets based on the Landré interval rule. We assume for now that the spin-orbit interaction can be ignored and we are left with the orbital Hamiltonian, H_o .

$$H_o = \sum_{i=1}^n \left(\frac{p_i^2}{2m} + V_i'(r_i) \right) \quad (\text{A.4})$$

The eigenfunctions of H_o consist of radial and angular components. The angular part of the eigenfunction for each electron is given by the angular components of the hydrogen eigenfunctions, but the radial components differ from the radial components of the hydrogen functions. The eigenfunctions of H_o for each electron are given by

$$|nlm_l\rangle = R'_{n,l}(r_i)Y_l^{m_l}(\theta_i, \phi_i) \quad (\text{A.5})$$

The one-electron eigenfunction of the Hamiltonian, H_0 , are assumed to consist of independent radial, angular, and spin components. The one-electron eigenfunctions of H_0 are given by

$$\psi_i = R'_{n,l}(r_i)Y_l^{m_l}(\theta_i, \phi_i)S(m_{s_i}) \quad (\text{A.6})$$

The multi-electron eigenfunction of H_0 is given by the product of the one-electron eigenfunctions.

$$\psi = \prod_i \psi_i \quad (\text{A.7})$$

In order to ensure that the wavefunctions are invariant under interchange of two electrons and that the Pauli exclusion principle is satisfied, the multi-electron wavefunctions are written in the form of a Slater determinant.

$$\psi(1,2,3,\dots,N) = \frac{1}{\sqrt{N!}} \begin{vmatrix} \psi_1(1) & \dots & \psi_N(1) \\ \vdots & \ddots & \vdots \\ \psi_1(N) & \dots & \psi_N(N) \end{vmatrix} \quad (\text{A.8})$$

The eigenfunctions of H_0 are a set of functions labeled as $|LSM_L M_S\rangle$. L is the total orbital angular momentum quantum number given by

$$L = \sum_i l_i \quad (\text{A.9})$$

where l_i is the orbital angular momentum of the i^{th} electron. S is the total spin quantum number given by

$$S = \sum_i s_i \quad (\text{A.10})$$

where s_i is the spin of an electron, which is equal to $\frac{1}{2}$. M_L is the orbital magnetic quantum number, and M_S is the spin magnetic quantum number.

Returning to the Hamiltonian

$$H_{FI} = H_o + H_{ee} \quad (\text{A.11})$$

Where

$$H_{ee} = \sum_{i \neq j} \frac{e^2}{4\pi\epsilon_0 r_{ij}} \quad (\text{A.12})$$

H_{ee} commutes with L and S so that it can only mix states with the same L and S quantum numbers. Configurational mixing of levels occurs whenever equivalent LS terms are derived for the same electronic configuration. To the extent that the configuration mixing is small, the eigenfunctions of Equation A.11 are the same as the eigenfunctions of H_o . The degeneracy of the LS terms under H_o is removed when the Coulomb interaction, H_{ee} , is included in the Hamiltonian. Assuming negligible configurational mixing, the shifts of the various LS terms from their central field values are calculated by solving the matrix elements

$$\langle LSM_L M_S | H_{ee} | LSM_L M_S \rangle \quad (\text{A.13})$$

These matrix elements consist of spin, angular, and radial overlap integrals. The spin and angular contributions can be calculated exactly but the radial wavefunctions are not known and so the radial overlap integrals are expressed in terms of Slater-Condon parameters, F_k . In this manner the energy of each LS term can be calculated and the values of the Slater-Condon parameters are determined empirically.

The derivation of the free-energy eigenvalues and eigenfunctions of rare-earth ions depends upon the relative strengths of ζ and H_{ee} . If $H_{ee} \gg \zeta$ then the problem proceeds as listed above. For the case where the spin-orbit coupling is not small with respect to H_{ee} then mixing of $|LSM_L M_S\rangle$ functions with the same values of J and M_J

requires that the eigenfunctions of the full Hamiltonian, H_{FI} , be labeled by the functions, $|LSJM_J\rangle$, where

$$|LSJM_J\rangle = \sum_{M_L M_S} |LSM_L M_S\rangle \langle LSM_L M_S | LSJM_J\rangle \quad (\text{A.14})$$

and $\langle LSM_L M_S | LSJM_J\rangle$ are vector-coupling coefficients.

In conclusion, the energy spectrum of a multi-electron atom is not usually determined solely from theory. If the wavefunctions of the complete Hamiltonian are taken to be Slater determinant wavefunctions, the energy levels can be expressed in terms of a small number of Slater-Condon parameters. The values of these parameters are determined by measuring the emission or absorption spectrum of the atom.

The Crystal Field Problem

The second part of the problem is the crystal field problem. This is the structure dependent part of the problem. The presence of a metal ion in a “lattice” can be modeled by assuming that the metal ion is surrounded by a set of fixed point charges^[284, 285] intended to represent nearest neighbor ligands. The point charge model is an approximation because ligand covalency and non-spherically symmetric ligand bonding interactions are neglected. This problem can be viewed as lowering the physical symmetry of the free ion to symmetry consistent with the bonding environment imposed by the lattice. For the sake of simplicity the organic system will be treated similar to a “lattice” of similar atoms.

After solving the free-ion problem the energies and wavefunctions of the free ion are known. These energy levels are then perturbed by placing the free ion into the crystal field environment of the “lattice”. Crystal field theory is used for the calculation of the

energy levels of a metal ion in a solid state bonding environment. The full Hamiltonian for the metal ion in the crystal can be expressed as

$$H = H_{FI} + H_{CF} = H_O + H_{ee} + H_{SO} + H_{CF} \quad (\text{A.15})$$

where H_{FI} is the free-ion Hamiltonian. H_{CF} is the crystal field Hamiltonian and can be expressed by

$$H_{CF} = \frac{1}{4\pi\epsilon_0} \sum_i \sum_l \frac{Ze^2}{|R_l - r_i|} \quad (\text{A.16})$$

where the summation over l is the sum over the electrons in the unfilled shell of the metal ion and the summation over i is the sum over the neighboring ions (6 for octahedral) which occupy equilibrium positions, R_i . The eigenfunction and eigenvalues of H are found using one of the following methods.

When the crystal field interactions is smaller than the inter-electron interaction and the spin-orbit coupling interaction, the eigenfunctions of H are taken to be the eigenfunctions of H_O and the new energy level structure can be determined using perturbation theory. This weak field approach works well for the shielded ions such as the trivalent rare-earth ions.

The intermediate crystal field approach is used when the crystal field interaction is intermediate between that of the inter-electron interaction and the spin-orbit coupling interaction. Now, the spin-orbit interaction is neglected initially. The orbital angular momentum wavefunction of the free-ion are used as the starting basis functions. The matrix elements of $\langle L' | H_{CF} | L \rangle$ are calculated and used to generate new orbital wavefunctions. These orbital wavefunctions are multiplied by spin wavefunctions and then the effect of the spin-orbit interaction is included as a final perturbation.

The last case is the strong crystal field case in which the crystal field interaction is stronger than the inter-electronic interaction. In this case, the inter-electron and spin-orbit interactions are initially neglected and the starting wavefunctions are products of one electron crystal field orbitals. The inter-electron interaction is taken into consideration and new orbital eigenfunctions and eigenvalues are determined. The eigenfunctions are multiplied by spin wavefunctions and then the effect of spin-orbit interaction is calculated.

A qualitative understanding of the role of the crystal field can be obtained by considering the effect of an octahedral crystal field on a system containing f orbitals. One way of labeling these orbitals is according to their orbital magnetic quantum numbers. An electron in an f orbital has orbital angular momentum equal to 3 so the possible orbital magnetic quantum numbers are +3, +2, +1, 0, -1, -2, and -3. These f orbitals are labeled f_{+3} , f_{+2} , f_{+1} , f_0 , f_{-1} , f_{-2} , and f_{-3} . In a spherically symmetric environment these orbitals are degenerate. When these orbitals are placed in a non-spherical environment such as an organic lattice, these orbitals listed above are no longer eigenstates of the system. In order to correct this problem, new orbitals which are real functions are created. These symmetrical orbitals are linear combinations of the orbitals labeled by their magnetic quantum number.^[286]

The crystal field Hamiltonian, HCF, for a metal ion with a single outer electron located a distance, a , away from six lattice ions each with a charge of Ze is given by

$$\begin{aligned}
H_{CF}(O_h) = & \left[\frac{-Ze^2}{4\pi\epsilon_0} \left\{ \frac{1}{\sqrt{r^2 + a^2 - 2ax}} + \frac{1}{\sqrt{r^2 + a^2 + 2ax}} \right\} \right] + \\
& \left[\frac{-Ze^2}{4\pi\epsilon_0} \left\{ \frac{1}{\sqrt{r^2 + a^2 - 2ay}} + \frac{1}{\sqrt{r^2 + a^2 + 2ay}} \right\} \right] + \\
& \left[\frac{-Ze^2}{4\pi\epsilon_0} \left\{ \frac{1}{\sqrt{r^2 + a^2 - 2az}} + \frac{1}{\sqrt{r^2 + a^2 + 2az}} \right\} \right]
\end{aligned} \tag{A.17}$$

where r ($r^2 = x^2 + y^2 + z^2$) is the position of the electron of the metal ion. The Hamiltonian can be expanded assuming $r < a$ to obtain a new expression for the Hamiltonian valid to sixth order in r .

$$H_{CF}(O_h) = \left[\begin{aligned} & \frac{-1}{4\pi\epsilon_0} \frac{6Ze^2}{a} + \frac{35Ze^2}{4\pi\epsilon_0 4a^5} \left\{ (x^4 + y^4 + z^4) - \frac{3}{5}r^4 \right\} + \\ & \frac{21Ze^2}{4\pi\epsilon_0 2a^7} \left\{ (x^6 + y^6 + z^6) + \frac{15}{4}(x^2y^4 + x^2z^4 + y^2x^4 + \right. \\ & \left. y^2z^4 + z^2x^4 + z^2y^4) - \frac{15}{14}r^6 \right\} \end{aligned} \right] \tag{A.18}$$

The Hamiltonian can be further simplified by writing in terms of spherical harmonics.

Inserting these spherical harmonics leads to the function

$$H_{CF}(O_h) = \sqrt{2\pi} \left[\begin{aligned} & \left(\frac{\sqrt{49}}{\sqrt{18}} \right) \left(\frac{Ze^2 r^4}{a^5} \right) \left[Y_4^0 + \left(\frac{\sqrt{5}}{\sqrt{14}} \right) (Y_4^4 + Y_4^{-4}) \right] \\ & + \left(\frac{\sqrt{9}}{\sqrt{832}} \right) \left(\frac{Ze^2 r^6}{a^7} \right) \left[Y_6^0 - \left(\frac{\sqrt{7}}{\sqrt{2}} \right) (Y_6^4 + Y_6^{-4}) \right] \end{aligned} \right] \tag{A.19}$$

The radial overlap integrals of the various $\langle d_{m_i} | H_{CF}(O_h) | d_{m_i} \rangle$ matrix elements are expressed in terms of two parameters, Dq' and Fr , for f-electron systems. These matrix elements are necessary to determine the secular determinant, which ultimately provides the energy levels.

Table A-1. Real orbitals created from linear combinations of orbitals labeled by their magnetic quantum number.

f-orbitals

$$f_{z^3} = f_0$$

$$f_{xz^2} = \frac{1}{\sqrt{2}}(f_{+3} + f_{-3})$$

$$f_{yz^2} = \frac{-i}{\sqrt{2}}(f_{+3} - f_{-3})$$

$$f_{z(xy)} = \frac{1}{\sqrt{2}}(f_{+2} + f_{-2})$$

$$f_{z(x^2-y^2)} = \frac{-i}{\sqrt{2}}(f_{+2} - f_{-2})$$

$$f_{x(x^2-3y^2)} = \frac{1}{\sqrt{2}}(f_{+1} + f_{-1})$$

$$f_{y(3x^2-y^2)} = \frac{-i}{\sqrt{2}}(f_{+1} - f_{-1})$$

$$Dq' = \left(\frac{2}{165} \right) \frac{er^4}{a^5} \quad (\text{A.20})$$

$$Fr = \sqrt{\frac{5}{572}} \frac{Zer^6}{a^7} \quad (\text{A.21})$$

Solving for the eigenvalues of the matrix for the f-electron systems results in two separate three-fold degenerate states ($6Dq' + 20 Fr$ and $-2Dq' - 36Fr$) and a singly-degenerate state at $-12Dq' + 48Fr$. The a_{2u} orbital is lowest in energy followed by the three-fold degenerate t_{2u} orbitals and the three-fold t_{1u} orbitals at highest energy.

Table A-2. Position and symmetry of f-orbitals in an octahedral crystal field.

Orbitals	Position & Symmetry
f_{xyz}	$-12Dq' + 48 Fr$, a_{2u}
$f_{x(5x^2-r^2)}$, $f_{z(5z^2-r^2)}$, $f_{y(5y^2-r^2)}$	$-2Dq' - 36 Fr$, t_{2u}
$f_{z(x^2-y^2)}$, $f_{x(y^2-z^2)}$, $f_{y(z^2-x^2)}$	$6Dq' + 20 Fr$, t_{1u}

Coupling of the Electronic and Lattice States

The energy levels of a metal ion in a solid can be described using a Hamiltonian that includes contributions from the free ion and crystal field Hamiltonians and potential and kinetic energy contributions from the “lattice”. The free-ion and crystal field contributions have been discussed in the previous two sections. The total Hamiltonian is given by

$$H = H_{FI}(r_i) + H_{CF}(r_i, R_l) + V_l(R_l) + \sum_l \frac{p_l^2}{2m_l} \quad (\text{A.22})$$

where H_{FI} is the free-ion Hamiltonian, H_{CF} is the crystal-field Hamiltonian, $V_l(R_l)$ is the inter-ion potential energy and the last term is the sum of the kinetic energy of the “lattice” ions. R_l is used to denote “lattice” ion coordinates and r_i is used to denote the positions of the metal ion’s electrons. The Hamiltonian is complicated because of the coupling of the electronic and ionic systems that occurs through the crystal field Hamiltonian. The electronic and ionic coordinates are decoupled using the Born-Oppenheimer approximation.^[17, 287]

The electronic contribution of the static lattice to the Hamiltonian is given by

$$H_O = H_{FI}(r_i) + H_{CF}(r_i, R_l) + V_l(R_l) \quad (\text{A.23})$$

where R_l is considered a parameter, not a variable. That is, the static lattice problem can be treated by solving over a desired range of fixed values of R_l . The static Hamiltonian can be further separated into electronic and inter-ionic contributions.

$$H_O = H_e(r_i, R_l) + V_l(R_l) \quad (\text{A.24})$$

The eigenfunctions of H_O are given by $\psi_a(r_i, R_l)$. The subscript, a , is necessary to label the electronic state because the value of R_l depends upon the electronic state of the

system. The eigenvalues of the static Hamiltonian are labeled $E^{(a)}(R_l)$ and for each R_l can be obtained from

$$H_0 \psi_a(r_i, R_l) = E^{(a)}(R_l) \psi_a(r_i, R_l) \quad (\text{A.25})$$

$$\begin{aligned} E^{(a)}(R_l) &= \langle \psi_a | H_e(r_i, R_l) | \psi_a \rangle + \langle \psi_a | V_l(R_l) | \psi_a \rangle \\ &= H_e(R_l) + V_l(R_l) \end{aligned} \quad (\text{A.26})$$

The full Hamiltonian for the dynamic lattice is given by

$$H = H_0 + \sum_l \frac{p_l^2}{2m_l} \quad (\text{A.27})$$

For a “lattice” comprised of a single type of ion with a mass, m_l , the Hamiltonian can be expressed as

$$H = H_0 - \left(\frac{\hbar^2}{2m_l} \right) \sum_l \nabla_l^2 \quad (\text{A.28})$$

The eigenfunctions of the full Hamiltonian are assumed to be of the form

$$\psi = \psi_a(r_i, R_l) \chi_a(R_l) \quad (\text{A.29})$$

These eigenfunctions are known as Born-Oppenheimer functions. Applying the “lattice” kinetic energy operator to wavefunctions of this form yields

$$\frac{-\hbar^2}{2m_l} \nabla_l^2 [\psi_a(r_i, R_l) \chi_a(r_i, R_l)] = -\frac{\hbar^2}{2m_l} [\chi_a \nabla_l^2 \psi_a + 2(\nabla_l \chi_a) \cdot (\nabla_l \psi_a) + \psi_a \nabla_l^2 \chi_a] \quad (\text{A.30})$$

In the Born-Oppenheimer approximation the first two terms are assumed to be negligible compared to the last term. This assumes that the electronic state does not have a strong dependence on the value of R_l . Physically this describes a situation in which the metal ion does not change electronic states due to motion of the lattice atoms. The Schrödinger equation for the metal ion in the “lattice” can be written as

$$[H_0\psi_a(r_i, R_l)]\chi_a(R_l) - \left[\sum_l \frac{\hbar^2}{2m_l} \nabla_l^2 \chi_a(R_l) \right] \psi_a(r_i, R_l) = E\psi_a(r_i, R_l)\chi_a(R_l) \quad (\text{A.31})$$

Simplifying gives

$$E^{(a)}(R_l)\psi_a(r_i, R_l)\chi_a(R_l) - \left[\sum_l \frac{\hbar^2}{2m_l} \nabla_l^2 \chi_a(R_l) \right] \psi_a(r_i, R_l) = E\psi_a(r_i, R_l)\chi_a(R_l) \quad (\text{A.32})$$

$$\left[E^{(a)}(R_l) - \sum_l \frac{\hbar^2}{2m_l} \nabla_l^2 \right] \chi_a(R_l) = E\chi_a(R_l) \quad (\text{A.33})$$

The “lattice” atoms are assumed to oscillate about an equilibrium position so that the position of the “lattice” atoms is given by $R_l = R_l^{(a)}(0) + q_l^{(a)}$ where $R_l^{(a)}(0)$ is the equilibrium coordinate of ion l in the electronic state a and $q_l^{(a)}$ is the displacement of the ion from its equilibrium position. The electronic energy can be expressed in terms of contributions from the static lattice and contributions from the dynamic lattice. The static contribution is $E_0^{(a)}$ where $E_0^{(a)}$ is given by

$$E_0^{(a)} = H_e^{(a)}(R_l^{(a)}(0)) + V_l^{(a)}(R_l^{(a)}(0)) \quad (\text{A.34})$$

The dynamic contribution is $E_D^{(a)}$ which is given by

$$E_D^{(a)} = V_e^{(a)}(q_l^{(a)}) + V_l^{(a)}(q_l^{(a)}) \quad (\text{A.35})$$

$V_e^{(a)}$ is the contribution if the dynamic lattice to the electronic Hamiltonian, $H_e^{(a)}$. The total energy is given by

$$E^{(a)}(R_l) = E_0^{(a)} + V_e^{(a)}(q_l^{(a)}) + V_l^{(a)}(q_l^{(a)}) \quad (\text{A.36})$$

$$E^{(a)}(R_l) = E_0^{(a)} + V^{(a)}(q_l^{(a)}) \quad (\text{A.37})$$

The Schrödinger equation can be rewritten as

$$\left[\sum_l \frac{-\hbar^2}{2m_l} \nabla_l^2 + V^{(a)}(q_l^{(a)}) \right] \chi_a(R_l) = [E - E_0^{(a)}] \chi_a(R_l) \quad (\text{A.38})$$

where $V(\mathbf{a})(\mathbf{q}_l(\mathbf{a}))$ is the potential energy of a 3-dimensional network of coupled oscillators. The standard approach to this problem is to describe the problem in terms of collective motions of the lattice atoms known as normal modes of oscillation.^[288] The normal modes are a function of a new set of coordinates, Q_k , rather than the individual “lattice” atom coordinates, q_l . This is a transformation from the “lattice” coordinates to normal coordinates. If $V(\mathbf{a})(Q_k)$ has a quadratic dependence on Q_k , then Equation A.38 can be solved by analogy to a system of coupled harmonic oscillators. The “lattice” eigenfunctions, $\chi_a(Q(\mathbf{a}))$, can be expressed as the product of linear harmonic oscillator eigenfunctions, $|n_k\rangle$, where k labels the normal modes.

$$\chi^{(a)}(Q^{(a)}) \Rightarrow \prod_k |n_k\rangle = \chi_a \quad (\text{A.39})$$

Equation A.38 becomes

$$\left[\sum_l \frac{-\hbar^2}{2m_l} \nabla_l^2 + V^{(a)}(Q_k) \right] \chi_a = \left[\sum_k \hbar \omega_k^{(a)} \left(n_k + \frac{1}{2} \right) \right] \chi_a \quad (\text{A.40})$$

The energy of the metal ion that is in the electronic state, a , can be written as a summation of contributions from the static and dynamic lattices.

$$E = E_0^{(a)} + \sum_k \hbar \omega_k^{(a)} \left(n_k + \frac{1}{2} \right) \quad (\text{A.41})$$

The “lattice” can support many different normal vibrational modes. In order to simplify the analysis, a single normal mode is assumed to be the dominant lattice contribution to the energy levels of the metal ion. This mode is generally taken to be the totally symmetric breathing mode. In the breathing mode the “lattice” atoms near the metal ion oscillate in phase towards and away from the metal ion. The equilibrium separation between the metal ion and its shell of nearest neighbors represents the

equilibrium position of the normal coordinate, $Q_0^{(a)}$. $Q_0^{(a)}$ is called the configuration coordinate. Recall that the electronic wavefunction, ψ_a , depends upon the lattice coordinates. The electronic wavefunction is calculated using the equilibrium value of Q . The full wavefunction can be written as

$$\psi = \psi_a(r_i, Q_0^{(a)}) \chi_a(n) \quad (\text{A.42})$$

Einstein Model

To understand the electronic properties of a system, it is important to understand the processes involved. In spectroscopic experiments the nature of matter is probed by measuring the absorption or emission of electromagnetic waves. A useful model of the interaction between light and matter was developed by Albert Einstein.^[289-291] The Einstein model assumes that atoms exist in a series of discrete energy levels. Transitions between the various energy levels are accompanied by the emission or absorption of photons. The transition must conserve energy, so the energy of the photon, $\hbar\omega$, must equal the difference in energy between the two levels that participate in the transition. The energy density of a radiation field in thermal equilibrium with a collection of atoms at temperature, T , is given by

$$\rho(\omega) = \frac{\frac{\hbar\omega^3}{\pi^2 c^3}}{\exp\left(\frac{\hbar\omega}{k_b T}\right) - 1} \quad (\text{A.43})$$

where ω is the angular frequency of the electromagnetic radiation, c is the velocity of light, and k_b is the Boltzman constant. Consider the simple case of a radiation field interacting with a collection of two level atoms. There are N_1 atoms in the lower energy level which has energy, E_1 , and a degeneracy of g_1 . Similarly, there are N_2 atoms in the

upper energy level which has energy, E_2 , and a degeneracy of g_2 . Atoms in the upper level can spontaneously transfer to the lower level with the simultaneous emission of a photon. The energy of the photon emitted is given by

$$\hbar\omega = E_2 - E_1 \quad (\text{A.44})$$

The rate at which a single atom spontaneously decays from the upper level is called the Einstein A coefficient. Two other processes can occur if the atoms are placed in a radiation field. These two processes are known as absorption and stimulated emission. Absorption of a photon transfers an atom from the lower level to the upper level. Stimulated emission transfers an atom from the upper level to the lower level with the simultaneous emission of a photon. Stimulated emission is the process involved in the operation of lasers. The rate of absorption is proportional to the Einstein coefficient, B_{12} , and the rate of stimulated emission is proportional to the Einstein coefficient, B_{21} . The rates for all three processes are given below.

$$\text{Spontaneous emission rate} = N_2 A$$

$$\text{Absorption rate} = N_1 B_{12} \rho(\omega)$$

$$\text{Stimulated emission rate} = N_2 B_{21} \rho(\omega)$$

Under steady state conditions, the rate of change in the number of atoms in each level is equal to zero. The rate of change of the number of atoms in the lower level is given by

$$\frac{dN_1}{dt} = -N_1 B_{12} \rho(\omega) + N_2 B_{21} \rho(\omega) + N_2 A \quad (\text{A.45})$$

Setting the rate equal to zero yields the relationship

$$N_1 B_{12} \rho(\omega) = N_2 B_{21} \rho(\omega) + N_2 A \quad (\text{A.46})$$

The relative sizes of the N_1 and N_2 populations are given by

$$\frac{N_2}{N_1} = \frac{g_2}{g_1} \exp\left(\frac{-\hbar\omega}{k_b T}\right) \quad (\text{A.47})$$

if the two energy levels are in thermal equilibrium at temperature, T. Combining equation (A.45) and equation (A.46) and solving for $\rho(\omega)$ yields

$$\rho(\omega) = \frac{\frac{g_2}{g_1} \exp\left(\frac{-\hbar\omega}{k_b T}\right) A}{B_{12} - \frac{g_2}{g_1} \exp\left(\frac{-\hbar\omega}{k_b T}\right) B_{21}} \quad (\text{A.48})$$

The relationships between A, B_{12} , and B_{21} are determined by simultaneously satisfying equation (A.46) and equation (A.48).

$$B_{12} = \frac{g_2}{g_1} B_{21} \quad (\text{A.49})$$

$$A = \frac{\hbar\omega^3 B_{21} g_2}{\pi^2 c^2} \quad (\text{A.50})$$

Another important quantity in spectroscopy is the spontaneous lifetime, τ , of an excited state. The spontaneous lifetime of an excited state is determined by the equation

$$\frac{dN_2}{dt} = -N_2 A \quad (\text{A.51})$$

which when solved yields

$$N_2 = N_2(t=0) \exp(-tA) \quad (\text{A.52})$$

$$N_2 = N_2(t=0) \exp\left(-\frac{t}{\tau}\right) \quad (\text{A.53})$$

where $\tau = \frac{1}{A}$.

The Einstein coefficients are related to many other quantities commonly used in spectroscopic measurements. These relationships are derived in many books on

spectroscopy and thus will not be derived here.^[292] Briefly, the electric dipole strength, S , is defined as the square of the electric dipole transition moment, $\langle \psi_2 | er | \psi_1 \rangle$.

$$S = \left| \langle \psi_2 | er | \psi_1 \rangle \right|^2 \quad (\text{A.54})$$

The absorption coefficient, α , of a homogeneous sample is defined by the following equation.

$$I_\nu(x) = I_\nu(0) \exp(-\alpha_\nu x) \quad (\text{A.55})$$

$I_\nu(0)$ is the intensity of light with frequency, ν , incident upon the sample. $I_\nu(x)$ is the intensity of the light after it has passed a distance x through the sample. Absorption will occur over a range of frequencies determined by the lineshape of the transition. The absorption coefficient integrated over the width of the transition is proportional to the Einstein coefficient, B_{12} .

$$\int_{\nu_0 - \Delta\nu}^{\nu_0 + \Delta\nu} \alpha_\nu d\nu = n_1 B_{12} \frac{h\nu_0}{c} \quad (\text{A.56})$$

where n_1 is the concentration of atoms in the lower level. The absorption coefficient can be converted into absorption per atom if the concentration in the lower level is known.

The absorption per atom is called the radiative atomic cross-section, σ_ν , and it is equal to α_ν divided by the concentration, n_1 .

$$\int_{\nu_0 - \Delta\nu}^{\nu_0 + \Delta\nu} \sigma_\nu d\nu = B_{12} \frac{h\nu_0}{c} \quad (\text{A.57})$$

The relationship between the oscillator strength, f , and the integrated intensity of the absorption band is given by the equation below.

$$\int_{\nu_0 - \Delta\nu}^{\nu_0 + \Delta\nu} \alpha_\nu d\nu = \frac{e^2}{4\epsilon_0 mc} N_1 f \quad (\text{A.58})$$

LIST OF REFERENCES

- [1] G. Blasse, B. C. Grabmaier, *Luminescent Materials*, Springer-Verlag, Berlin, **1994**.
- [2] D. M. Roundhill, *Photochemistry and Photophysics of Metal Complexes*, Plenum Press, New York, **1994**.
- [3] G. F. Strouse, *Inorg. Chem.* **1995**, *34*, 473.
- [4] J. V. Caspar, E. M. Kober, B. P. Sullivan, T. J. Meyer, *J. Am. Chem. Soc.* **1982**, *104*, 630.
- [5] R. Engelman, J. Jortner, *Molecular Physics* **1970**, *18*, 145.
- [6] S. H. Lin, *Journal of Chemical Physics* **1970**, *53*, 3766.
- [7] G. Stein, E. Wurzburg, *Journal of Chemical Physics* **1975**, *62*, 208.
- [8] J. V. Caspar, T. J. Meyer, *Journal of Physical Chemistry* **1983**, *87*, 952.
- [9] J. M. F. Vandijk, M. F. H. Schuurmans, *Journal of Chemical Physics* **1983**, *78*, 5317.
- [10] T. Förster, *Ann. Phys. (Leipzig)* **1948**, *2*, 55.
- [11] M. Pope, C. E. Swenberg, *Electronic Processes in Organic Crystals*, Oxford University Press, Oxford, **1982**.
- [12] D. L. Dexter, *J. Chem. Phys.* **1953**, *21*, 836.
- [13] J. Becquerel, *Phys. Z.* **1908**, *8*, 632.
- [14] S. Shionoya, *Luminescence of Solids*, Plenum Press, New York, **1998**.
- [15] G. H. Dieke, *Spectra and Energy Levels of Rare Earth Ions in Crystals*, Wiley-Interscience, New York, **1968**.
- [16] H. M. Crosswhite, H. W. Moos, *Optical Properties of Ions in Crystals*, Interscience, New York, **1967**.
- [17] B. Henderson, G. F. Imbusch, *Optical Spectroscopy of Inorganic Solids*, Oxford University Press, New York, **1989**.

- [18] B. R. Judd, *Physical Review* **1962**, *127*, 750.
- [19] G. S. Ofelt, *Journal of Chemical Physics* **1962**, *37*, 511.
- [20] W. T. Carnall, Handbook on the Physics and Chemistry of Rare Earths, Vol. 1, North Holland Company, Amsterdam **1979**.
- [21] R. D. Peacock, *Structure and Bonding* **1975**, *22*, 83.
- [22] S. Cotton, *Lanthanides and Actinides*, Oxford University Press, Oxford, **1991**.
- [23] S. I. Weissman, *J. Chem. Phys.* **1942**, *10*, 214.
- [24] K. A. Gschneider, L. R. Eyring, *Handbook on the Physics and Chemistry of Rare Earths*, Vol. 3, North-Holland Company, Amsterdam, **1978**.
- [25] L. Stryer, *Biochemistry*, W.H. Freeman and Company, New York, **1995**.
- [26] H. Scheer, *Chlorophylls*, CRC Press, Boca Raton, **1991**.
- [27] M. O. Senge, *Photochemistry and Photobiology* **1993**, *57*, 189.
- [28] R. E. Dickerson, I. Geis, *Hemoglobin: Structure, Function, Evolution, and Pathology*, Benjamin Cummings, Menlo Park, CA, **1983**.
- [29] A. D. Adler, M. Gouterman, *Opt. Prop. Struct. Tetrapyrroles, Proc. Symp.* **1985**, *3*.
- [30] A. K. Burrell, D. L. Officer, P. G. Plieger, D. C. W. Reid, *Chemical Reviews* **2001**, *101*, 2751.
- [31] J. P. Guo, K. Ye, Y. Wu, Y. Liu, Y. S. Wang, *Synthetic Metals* **2003**, *137*, 1075.
- [32] K. T. Nielsen, H. Spanggaard, F. C. Krebs, *Displays* **2004**, *25*, 231.
- [33] M. Gouterman, *J. Mol. Spectrosc.* **1961**, *6*, 138.
- [34] M. Gouterman, G. H. Wagniere, L. C. Snyder, *J. Mol. Spectrosc.* **1963**, *11*, 108.
- [35] P. J. Spellane, M. Gouterman, A. Antipas, S. Kim, Y. C. Liu, *Inorg. Chem.* **1980**, *19*, 386.
- [36] A. Antipas, M. Gouterman, *J. Am. Chem. Soc.* **1983**, *105*, 4896.
- [37] M. Gouterman, *The Porphyrins*, Vol. 3 (Ed.: D. Dolphin), Academic Press, New York, **1978**
- [38] O. Ohno, Y. Kaizu, H. Kobayashi, *J. Chem. Phys.* **1985**, *82*, 1779.

- [39] R. S. Becker, J. B. J. Allison, *J. Phys. Chem.* **1963**, *67*, 2669.
- [40] D. Eastwood, M. Gouterman, *J. Mol. Spectrosc.* **1979**, *35*, 359.
- [41] J. B. Callis, M. Gouterman, Y. M. Jones, B. H. Henderson, *J. Mol. Spectrosc.* **1971**, *39*, 410.
- [42] G. Knor, A. Vogler, *Inorg. Chem.* **1994**, *33*, 314.
- [43] K. M. Kadish, A. Villard, E. V. Autret, P. Caemelbecke, P. Bianco, A. Antonini, P. Taglietesta, *Inorg. Chem.* **1994**, *33*, 5169.
- [44] R. A. Binstead, M. J. Crossley, N. S. Hush, *Inorg. Chem.* **1991**, *30*, 1259.
- [45] W. D. Horrocks, Jr., C. P. Wong, R. F. Venteicher, E. G. Hove, *Proc. Rare Earth Res. Conf., 12th* **1976**, *1*, 241.
- [46] M. Gouterman, C. D. Schumaker, T. S. Srivastava, T. Yonetani, *Chemical Physics Letters* **1976**, *40*, 456.
- [47] Y. Korovin, N. Rusakova, *Reviews in Inorganic Chemistry* **2001**, *21*, 299.
- [48] V. E. Pyatosin, M. P. Tsvirko, K. N. Solovev, T. F. Kachura, *Optika I Spektroskopiya* **1982**, *52*, 269.
- [49] M. P. Tsvirko, K. N. Solov'ev, G. F. Stel'makh, V. E. Pyatosin, T. F. Kachura, *Optika i Spektroskopiya* **1981**, *50*, 555.
- [50] M. P. Tsvirko, K. N. Soloviev, A. S. Piskarskas, V. E. Piatosin, V. V. Krasauskas, T. F. Kachura, *Doklady Akademii Nauk Sssr* **1984**, *279*, 1118.
- [51] M. P. Tsvirko, G. F. Stelmakh, V. E. Pyatosin, K. N. Solovyov, T. F. Kachura, A. S. Piskarskas, R. A. Gadonas, *Chemical Physics* **1986**, *106*, 467.
- [52] K. N. Solovev, M. P. Tsvirko, V. E. Pyatosin, T. F. Kachura, *Izvestiya Akademii Nauk Sssr Seriya Fizicheskaya* **1982**, *46*, 242.
- [53] K. N. Solovev, M. P. Tsvirko, T. F. Kachura, *Optika I Spektroskopiya* **1976**, *40*, 684.
- [54] P. Bhyrappa, V. Krishnan, *Inorg. Chem.* **1991**, *30*, 239.
- [55] J. H. Furhop, K. M. Kadish, D. G. Davis, *J. Am. Chem. Soc.* **1973**, *95*, 5140.
- [56] K. M. Kadish, M. M. Morrison, *J. Am. Chem. Soc.* **1976**, *98*, 3326.
- [57] K. M. Kadish, X. Q. Lin, J. Q. Jin, Y. T. Wu, C. Araullo, *Inorg. Chem.* **1986**, *25*, 3236.

- [58] A. Girardeau, H. J. Callot, J. Jordan, I. Ezhar, M. Gross, *J. Am. Chem. Soc.* **1979**, *101*, 3785.
- [59] S. Jeon, T. C. Bruice, *Inorg. Chem.* **1991**, *30*, 4311.
- [60] S. Jeon, T. C. Bruice, *Inorg. Chem.* **1992**, *31*, 4843.
- [61] J. S. Lindsey, H. C. Hsu, I. C. Schreiman, *J. Org. Chem.* **1986**, *52*, 827–836.
- [62] J. S. H. Lindsey, I. C. Schreilman, *Tetrahedron Letters* **1986**, *27*, 4969.
- [63] D. M. Li, G. F. Liu, T. S. Shi, M. Lin, Y. W. Liu, M. Z. Zou, X. Z. Cao, X. X. Liu, *Gaodeng Xuexiao Huaxue Xuebao* **1995**, *16*, 1180.
- [64] C. P. Wong, R. F. Venteicher, W. D. Horrocks, *J. Am. Chem. Soc.* **1974**, *96*, 7149.
- [65] G. A. Spyroulias, D. de Montauzon, A. Maisonat, R. Poilblanc, A. G. Coutsolelos, *Inorg. Chem. Acta* **1998**, *276*, 182.
- [66] G. A. Spyroulias, A. G. Coutsolelos, C. P. Raptopoulou, A. Terzis, *Inorg. Chem.* **1995**, *34*, 2476.
- [67] J. Z. Jiang, T. C. W. Mak, D. K. P. Ng, *Chem. Ber.* **1996**, *129*, 933.
- [68] C. J. Schaverien, A. G. Orpen, *Inorganic Chemistry* **1991**, *30*, 4968.
- [69] W. K. Wong, A. X. Hou, J. P. Guo, H. S. He, L. Zhang, W. Y. Wong, K. F. Li, K. W. Cheah, F. Xue, T. C. W. Mak, *Journal of the Chemical Society, Dalton Transactions* **2001**, 3092.
- [70] T. J. Foley, K. A. Abboud, J. M. Boncella, *Inorganic Chemistry* **2002**, *41*, 1704.
- [71] M. M. Pope, P. ; Kallman, H. P., *J. Chem. Phys.* **1963**, *38*, 2042.
- [72] W. Helfrich, W. G. Schneider, *Phys. Rev. Lett.* **1965**, *17*, 229.
- [73] C. W. Tang, S. A. Van Slyke, *Applied Physics Letters* **1987**, *51*, 913.
- [74] J. H. Burroughes, D. D. Bradley, A. R. Brown, R. N. Marks, K. Mackay, R. H. Friend, P. L. Burns, A. B. Holmes, *Nature* **1990**, 347.
- [75] G. Destriau, *J. Chim. Phys.* **1936**, *33*, 587.
- [76] M. Pope, C. E. Swenberg, *Electronic Processes in Organic Crystals and Polymers*, second ed., Oxford University Press, New York, **1999**.
- [77] A. J. Heeger, S. Kivelson, J. R. Schrieffer, W. P. Su, *Rev. Mod. Phys.* **1988**, *60*, 781.

- [78] C. Adachi, M. A. Baldo, S. R. Forrest, M. E. Thompson, *Applied Physics Letters* **2000**, *77*, 904.
- [79] Y. Gao, C. Yu, R. Zhang, R. Menon, A. J. Heeger, *Syn. Met.* **1997**, *87*, 171.
- [80] Z. Peng, J. Zhang, *Chemistry of Materials* **1999**, *11*, 1138.
- [81] Q. Pei, Y. Yang, *Chemistry of Materials* **1995**, *7*, 1568.
- [82] K. Nagai, C. Adachi, H. Sakon, N. Tamoto, (Ricoh Kk, Japan). Application: JP JP, **1995**, p. 13 pp.
- [83] Y. Yang, Q. Pei, *Journal of Applied Physics* **1995**, *77*, 4807.
- [84] T. Mori, M. Suzuki, , S. Tokito, Y. Taga, *Proceedings of SPIE-The International Society for Optical Engineering* **1999**, *3797*, 367.
- [85] S. Lamansky, R. C. Kwong, M. Nugent, P. I. Djurovich, M. E. Thompson, *Organic Electronics* **2001**, *2*, 53.
- [86] H. Xia, C. Zhang, S. Qiu, P. Lu, J. Zhang, Y. Ma, *Applied Physics Letters* **2004**, *84*, 290.
- [87] K. C. Kao, W. Hwang, *Electrical Transport in Solids*, Pergammon Press, Oxford, **1981**.
- [88] M. Stolka, J. F. Janus, D. M. Pai, *J. Phys. Chem.* **1984**, *88*, 4707.
- [89] E. W. Forsythe, D. C. Morton, Q. T. Le, L. Yan, F. Nuesch, C. W. Tang, Y. Gao, *Proceedings of SPIE-The International Society for Optical Engineering* **1998**, *3623(Organic Photonic Materials and Devices)*, 13.
- [90] B. Chen, S. Liu, *Syn. Met.* **1997**, *91*, 169.
- [91] W. D. Gill, *J. Appl. Phys.* **1972**, *43*, 5033.
- [92] M. A. Lampert, P. Mark, *Current Injection in Solids*, Academic Press, New York, **1970**.
- [93] J. S. Kim, P. K. H. Ho, N. C. Greenham, R. H. Friend, *J. Appl. Phys.* **2000**, *88*, 1073.
- [94] Z. Shuai, D. Beljonne, R. J. Silbery, J. L. Bredas, *Phys. Rev. Lett.* **2000**, *84*, 131.
- [95] M. Wohlgenant, T. K., S. Mazumdar, S. Ramasesha, Z. V. Vardeny, *Nature* **2001**, *409*, 494.
- [96] M. A. Baldo, M. E. Thompson, S. R. Forrest, *Pure and Applied Chemistry* **1999**, *71*, 2095.

- [97] M. A. Baldo, S. R. Forrest, *Physical Review B: Condensed Matter and Materials Physics* **2000**, *62*, 10958.
- [98] M. A. Baldo, C. Adachi, S. R. Forrest, *Physical Review B: Condensed Matter and Materials Physics* **2000**, *62*, 10967.
- [99] C. H. Chen, C. W. Tang, J. Shi, K. P. Klubek, *Macromolecular Symposia* **1998**, *125*, 49.
- [100] C. H. Chen, C. W. Tang, *Applied Physics Letters* **2001**, *79*, 3711.
- [101] M. T. Lee, C. K. Yen, W. P. Yang, H. H. Chen, C. H. Liao, C. H. Tsai, C. H. Chen, *Organic Letters* **2004**, *6*, 1241.
- [102] C. H. Lee, S. H. Ryu, H. D. Jang, S. Y. Oh, *Materials Science & Engineering C-Biomimetic and Supramolecular Systems* **2004**, *24*, 87.
- [103] C. Q. Ma, X. S. Wang, B. W. Zhang, Y. Cao, *Progress in Chemistry* **2004**, *16*, 463.
- [104] H. Y. Kang, C. H. Lee, *Journal of the Korean Physical Society* **2004**, *45*, 756.
- [105] Y. Sato, S. Ichinosawa, H. Kanai, *IEEE Journal of Selected Topics in Quantum Electronics* **1998**, *4*, 40.
- [106] J. McElvain, H. Antoniadis, M. R. Hueschen, J. N. Miller, D. M. Roitman, J. R. Sheats, R. L. Moon, *J. Appl. Phys.* **1996**, *80*, 6002.
- [107] B. H. Cumpston, K. F. Jensen, *Applied Physics Letters* **1996**, *69*, 3941.
- [108] B. H. Cumpston, K. F. Jensen, *Syn. Met.* **1995**, *73*, 195.
- [109] B. H. Cumpston, I. D. Parker, K. F. Jensen, *J. Appl. Phys.* **1997**, *81*, 3716.
- [110] L. E. Tannas, *Flat Panel Displays and CRTs*, Van Nostrand, Reinhold, NY, **1984**.
- [111] L. Robinson, The Dow Chemical Company, Midland, MI, **2003**.
- [112] B. P. Sullivan, in *ElectronicsTalk*, **2004**.
- [113] D. R. Baigent, P. J. Hamer, R. H. Friend, S. C. Moratti, A. B. Holmes, *Synthetic Metals* **1995**, *71*, 2175.
- [114] A. Fujii, Y. Ohmori, K. Yoshino, *IEEE Transactions on Electron Devices* **1997**, *44*, 1204.
- [115] H. Suzuki, *Applied Physics Letters* **2000**, *76*, 1543.

- [116] E. I. Maltsev, D. A. Lypenko, V. V. Bobinkin, A. R. Tameev, S. V. Kirillov, B. I. Shapiro, H. F. M. Schoo, A. V. Vannikov, *Applied Physics Letters* **2002**, *81*, 3088.
- [117] J. C. Ostrowski, K. Susumu, M. R. Robinson, M. J. Therien, G. C. Bazan, *Advanced Materials (Weinheim, Germany)* **2003**, *15*, 1296.
- [118] H. Suzuki, *Journal of Photochemistry and Photobiology a-Chemistry* **2004**, *166*, 155.
- [119] R. Q. Yang, R. Y. Tian, J. G. Yan, Y. Zhang, J. Yang, Q. Hou, W. Yang, C. Zhang, Y. Cao, *Macromolecules* **2005**, *38*, 244.
- [120] B. C. Thompson, L. G. Madrigal, M. R. Pinto, T. S. Kang, K. S. Schanze, J. R. Reynolds, *Journal of Polymer Science Part a-Polymer Chemistry* **2005**, *43*, 1417.
- [121] J. S. Steckel, S. Coe-sullivan, V. Bulovic, M. G. Bawendi, *Advanced Materials (Weinheim, Germany)* **2003**, *15*, 1862.
- [122] L. Bakueva, G. Konstantatos, L. Levina, S. Musikhin, E. H. Sargent, *Applied Physics Letters* **2004**, *84*, 3459.
- [123] E. H. Sargent, *Advanced Materials* **2005**, *17*, 515.
- [124] D. S. Koktysh, N. Gaponik, M. Reufer, J. Crewett, U. Scherf, A. Eychmueller, J. M. Lupton, A. L. Rogach, J. Feldmann, *ChemPhysChem* **2004**, *5*, 1435.
- [125] G. A. Crosby, M. Kasha, *Spectrochimica Acta* **1958**, *10*, 377.
- [126] G. A. Crosby, R. E. Whan, *Naturwissenschaften* **1960**, *47*, 276.
- [127] G. A. Crosby, R. E. Whan, *Journal of Chemical Physics* **1960**, *32*, 614.
- [128] G. A. Crosby, R. E. Whan, R. M. Alire, *Journal of Chemical Physics* **1961**, *34*, 743.
- [129] G. A. Crosby, R. E. Whan, J. J. Freeman, *Journal of Physical Chemistry* **1962**, *66*, 2493.
- [130] G. A. Crosby, R. E. Whan, *Journal of Chemical Physics* **1962**, *36*, 863.
- [131] G. A. Crosby, *Molecular Crystals* **1966**, *1*, 37.
- [132] W. G. Perkins, G. A. Crosby, *Journal of Chemical Physics* **1965**, *42*, 407.
- [133] W. G. Perkins, G. A. Crosby, *Journal of Chemical Physics* **1965**, *42*, 2621.
- [134] R. W. Harrigan, G. A. Crosby, *Journal of Chemical Physics* **1970**, *52*, 4912.

- [135] R. E. Whan, G. A. Crosby, *Journal of Molecular Spectroscopy* **1962**, 8, 315.
- [136] J. J. Freeman, G. A. Crosby, *Journal of Physical Chemistry* **1963**, 67, 2717.
- [137] T. F. Kachura, Sevchenk.An.; K. N. Solovev, M. P. Tsvirko, *Doklady Akademii Nauk Sssr* **1974**, 217, 1121.
- [138] W. D. Horrocks, R. F. Venteicher, C. A. Spilburg, B. L. Vallee, *Biochemical and Biophysical Research Communications* **1975**, 64, 317.
- [139] K. N. Solov'ev, M. P. Tsvirko, T. F. Kachura, *Tezisy Dokl. - Vses. Soveshch. Lyumin.*, 22nd **1975**, 82.
- [140] M. P. Tsvirko, T. F. Kachura, *Zhurnal Prikladnoi Spektroskopii* **1975**, 23, 907.
- [141] E. G. Hove, Ph.D. Thesis, Penn State University, **1978**.
- [142] T. S. Srivastava, *Bioinorganic Chemistry* **1978**, 8, 61.
- [143] K. Tatsumi, M. Tsutsui, *Journal of the American Chemical Society* **1980**, 102, 882.
- [144] K. N. Solov'ev, G. F. Stel'makh, V. E. Pyatosin, K. N. Solovyov, T. F. Kachura, *Chemical Physics Letters* **1980**, 73, 80.
- [145] P. Sayer, M. Gouterman, C. R. Connell, *Accounts of Chemical Research* **1982**, 15, 73.
- [146] G. Liu, *Fenzi Kexue Yu Huaxue Yanjiu* **1985**, 5, 131.
- [147] S. F. Mason, *Journal of the Indian Chemical Society* **1986**, 63, 73.
- [148] Y. Yang, W. Wang, B. Yu, Z. Guan, *Guangpuxue Yu Guangpu Fenxi* **1986**, 6, 5.
- [149] W. Strek, J. Sztucki, *Chemical Physics Letters* **1989**, 158, 301.
- [150] M. I. Gaiduk, V. V. Grigor'yants, A. F. Mironov, V. D. Rumyantseva, *Eesti Teaduste Akadeemia Toimetised, Fuusika, Matemaatika* **1991**, 40, 198.
- [151] V. E. Pyatosin, M. P. Tsvirko, *Optika i Spektroskopiya* **1991**, 70, 379.
- [152] T. A. Shakhverdov, R. Ergashev, V. N. Kalinin, *Optika i Spektroskopiya* **1991**, 70, 1163.
- [153] Q. Zhuang, X. C. Gao, *Fushun Shiyou Xueyuan Xuebao* **1996**, 16, 64.
- [154] M. Latva, H. Takalo, V. M. Mukkala, C. Matachescu, J. C. Rodriguez-Ubis, J. Kankare, *Journal of Luminescence* **1997**, 75, 149.

- [155] R. J. Curry, W. P. Gillin, *Applied Physics Letters* **1999**, *75*, 1380.
- [156] R. J. Curry, W. P. Gillin, *Synthetic Metals* **2000**, *111-112*, 35.
- [157] R. J. Curry, W. P. Gillin, *Current Opinion in Solid State & Materials Science* **2001**, *5*, 481.
- [158] R. I. R. Blyth, J. Thompson, V. Arima, Y. Zou, R. Fink, E. Umbach, G. Gigli, R. Cingolani, *Synthetic Metals* **2004**, *142*, 293.
- [159] J. Thompson, R. I. R. Blyth, G. Gigli, R. Cingolani, *Advanced Functional Materials* **2004**, *14*, 979.
- [160] Y. Kawamura, Y. Wada, M. Iwamuro, T. Kitamura, S. Yanagida, *Chemistry Letters* **2000**, 280.
- [161] O. M. Khreis, W. P. Gillin, M. Somerton, R. J. Curry, *Organic Electronics* **2001**, *2*, 45.
- [162] O. M. Khreis, R. J. Curry, M. Somerton, W. P. Gillin, *Journal of Applied Physics* **2000**, *88*, 777.
- [163] Y. Kawamura, Y. Wada, S. Yanagida, *Japanese Journal of Applied Physics, Part I: Regular Papers, Short Notes & Review Papers* **2001**, *40*, 350.
- [164] J. Thompson, R. I. R. Blyth, V. Arima, Y. Zou, R. Fink, E. Umbach, G. Gigli, R. Cingolani, *Materials Science & Engineering, B: Solid-State Materials for Advanced Technology* **2003**, *B105*, 41.
- [165] R. Van Deun, P. Fias, P. Nockemann, A. Schepers, T. N. Parac-Vogt, K. Van Hecke, L. Van Meervelt, K. Binnemans, *Inorganic Chemistry* **2004**, *43*, 8461.
- [166] F. Artizzu, P. Deplano, L. Marchio, M. L. Mercuri, L. Pilia, A. Serpe, F. Quochi, R. Orru, F. Cordella, F. Meinardi, R. Tubino, A. Mura, G. Bongiovanni, *Inorganic Chemistry* **2005**, *44*, 840.
- [167] Z. R. Hong, C. J. Liang, R. G. Li, F. X. Zang, D. Fan, W. L. Li, L. S. Hung, S. T. Lee, *Applied Physics Letters* **2001**, *79*, 1942.
- [168] Z. R. Hong, C. J. Liang, R. G. Li, D. Zhao, D. Fan, W. L. Li, *Thin Solid Films* **2001**, *391*, 122.
- [169] B. Harrison, Ph.D. thesis, University of Florida (Gainesville), **2003**.
- [170] F. X. Zang, Z. R. Hong, W. L. Li, M. T. Li, X. Y. Sun, *Applied Physics Letters* **2004**, *84*, 2679.
- [171] F. X. Zang, W. L. Li, Z. R. Hong, H. Z. Wei, M. T. Li, X. Y. Sun, C. S. Lee, *Applied Physics Letters* **2004**, *84*, 5115.

- [172] L. H. Slooff, A. Polman, F. Cacialli, R. H. Friend, G. A. Hebbink, F. C. J. M. van Veggel, D. N. Reinhoudt, *Applied Physics Letters* **2001**, 78, 2122.
- [173] B. S. Harrison, T. J. Foley, M. Bouguettaya, J. M. Boncella, J. R. Reynolds, K. S. Schanze, J. Shim, P. H. Holloway, G. Padmanaban, S. Ramakrishnan, *Applied Physics Letters* **2001**, 79, 3770.
- [174] J. M. Boncella, T. J. Foley, B. Harrison, K. S. Schanze, J. R. Reynolds, M. Bouguettaya, J. Shim, P. H. Holloway, S. Ramakrishnan, *Polymeric Materials Science and Engineering* **2002**, 86, 72.
- [175] T. J. Foley, B. S. Harrison, A. S. Knefely, K. A. Abboud, J. R. Reynolds, K. S. Schanze, J. M. Boncella, *Inorganic Chemistry* **2003**, 42, 5023.
- [176] T. S. Kang, B. S. Harrison, T. J. Foley, A. S. Knefely, J. M. Boncella, J. R. Reynolds, K. S. Schanze, *Advanced Materials* **2003**, 15, 1093.
- [177] B. S. Harrison, T. J. Foley, A. S. Knefely, J. K. Mwaura, G. B. Cunningham, T. S. Kang, M. Bouguettaya, J. M. Boncella, J. R. Reynolds, K. S. Schanze, *Chemistry of Materials* **2004**, 16, 2938.
- [178] J. B. Oh, Y. H. Kim, M. K. Nah, H. K. Kim, *Journal of Luminescence* **2005**, 111, 255.
- [179] D. J. Quimby, F. R. Longo, *Journal of the American Chemical Society* **1975**, 97, 5111.
- [180] W. K. Wong, L. L. Zhang, W. T. Wong, F. Xue, T. C. W. Mak, *Journal of the Chemical Society-Dalton Transactions* **1999**, 615.
- [181] M. Asano-Someda, Y. Kaizu, *Journal of Photochemistry and Photobiology, A: Chemistry* **2001**, 139, 161.
- [182] W. Siebrand, *Journal of Chemical Physics* **1967**, 46, 440.
- [183] T. S. Kang, B. S. Harrison, T. J. Foley, A. S. Knefely, J. M. Boncella, J. R. Reynolds, K. S. Schanze, *Advanced Materials* **2003**, 15, 1093.
- [184] C. J. Liang, T. C. Wong, L. S. Hung, S. T. Lee, Z. R. Hong, W. L. Li, *Journal of Physics D: Applied Physics* **2001**, 34, L61.
- [185] J. M. Zhang, T. Abe, M. Kaneko, *Journal of Porphyrins and Phthalocyanines* **1998**, 2, 93.
- [186] J. L. Bredas, R. Silbey, D. S. Boudreaux, R. R. Chance, *J. Am. Chem. Soc.* **1983**, 105, 6555.
- [187] K. M. Kadish, E. V. Caemelbecke, *J. Solid. State Electrochem.* **2003**, 7, 254.

- [188] N. E. Murr, A. Chaloyard, W. Klauwi, *Inorg. Chem.* **1979**, *18*, 2629
- [189] H. Shirakawa, E. J. Louis, A. G. MacDiarmid, C. K. Chiang, J. Heeger, *J. Chem. Soc., Chem. Commun.* **1977**, 1977, 578.
- [190] T. Masuda, *The Chemistry of Triple-Bonded Functional Groups*, Wiley, New York, **1994**.
- [191] Y. Abe, H. Kouzai, T. Mizumoto, T. Masuda, T. Higashimura, *Polymer Journal* **1994**, *26*, 207.
- [192] H. Balcar, P. Kubat, M. Pacovska, V. Blechta, *Polymer Journal* **2000**, *32*, 370.
- [193] M. Belletete, E. Rivera, R. Giasson, X. X. Zhu, G. Durocher, *Synthetic Metals* **2004**, *143*, 37.
- [194] F. Cataldo, *Polymer* **1994**, *35*, 5235.
- [195] M. Fahlman, J. Birgersson, K. Kaeriyama, W. R. Salaneck, *Synthetic Metals* **1995**, *75*, 223.
- [196] Y. S. Gal, S. H. Jin, H. J. Lee, K. T. Lim, S. Y. Kim, *Molecular Crystals and Liquid Crystals* **2004**, *425*, 509.
- [197] I. I. Gontia, Z. V. Vardeny, T. Masuda, K. Yoshino, *Physical Review B* **2002**, *66*.
- [198] R. Hidayat, M. Hirohata, K. Tada, M. Teraguchi, T. Masuda, K. Yoshino, *Japanese Journal of Applied Physics Part 1-Regular Papers Short Notes & Review Papers* **1997**, *36*, 3740.
- [199] R. Hidayat, M. Hirohata, K. Tada, M. Teraguchi, T. Masuda, K. Yoshino, *Japanese Journal of Applied Physics Part 2-Letters* **1998**, *37*, L180.
- [200] R. Hidayat, M. Hirohata, S. Tatsuhara, M. Ozaki, M. Teraguchi, T. Masuda, K. Yoshino, *Synthetic Metals* **1999**, *101*, 210.
- [201] R. Hidayat, S. Tatsuhara, D. W. Kim, M. Ozaki, K. Yoshino, M. Teraguchi, T. Masuda, *Physical Review B* **2000**, *61*, 10167.
- [202] Y. M. Huang, J. W. Y. Lam, K. K. L. Cheuk, W. K. Ge, B. Z. Tang, *Thin Solid Films* **2000**, *363*, 146.
- [203] S. M. A. Karim, K. Musikabhumma, R. Nomura, T. Masuda, *Proceedings of the Japan Academy Series B-Physical and Biological Sciences* **1999**, *75*, 97.
- [204] S. M. A. Karim, R. Nomura, H. Kajii, R. Hidayat, K. Yoshino, T. Masuda, *Journal of Polymer Science Part a-Polymer Chemistry* **2000**, *38*, 4717.

- [205] S. M. A. Karim, R. Nomura, F. Sanda, S. Seki, M. Watanabe, T. Masuda, *Macromolecules* **2003**, *36*, 4786.
- [206] J. W. Y. Lam, J. D. Luo, H. Peng, Z. L. Xie, K. T. Xue, Y. P. Dong, L. Cheng, C. F. Qiu, H. S. Kwok, B. Z. Tang, *Chinese Journal of Polymer Science* **2001**, *19*, 585.
- [207] C. C. W. Law, J. W. Chen, J. W. Y. Lam, H. Peng, B. Z. Tang, *Journal of Inorganic and Organometallic Polymers* **2004**, *14*, 39.
- [208] M. Teraguchi, T. Masuda, *Journal of Polymer Science Part a-Polymer Chemistry* **1999**, *37*, 4546.
- [209] Z. L. Xie, J. W. Y. Lam, Y. P. Dong, C. F. Qiu, H. S. Kwok, B. Z. Tang, *Optical Materials* **2003**, *21*, 231.
- [210] T. Yoshida, Y. Abe, T. Masuda, T. Higashimura, *Journal of Polymer Science Part a-Polymer Chemistry* **1996**, *34*, 2229.
- [211] E. M. Conwell, *Microelectronic Engineering* **1999**, *47*, 43.
- [212] S. V. Frolov, A. Fujii, D. Chinn, M. Hirohata, R. Hidayat, M. Taraguchi, T. Masuda, K. Yoshino, Z. V. Vardeny, *Advanced Materials* **1998**, *10*, 869.
- [213] A. Fujii, R. Ootake, T. Fujisawa, M. Ozaki, Y. Ohmori, T. Laga, K. Yoshino, H. F. Lu, H. S. O. Chan, S. C. Ng, *Applied Physics Letters* **2000**, *77*, 660.
- [214] R. Hidayat, M. Hirohata, A. Fujii, M. Teraguchi, T. Masuda, K. Yoshino, *Japanese Journal of Applied Physics Part 1-Regular Papers Short Notes & Review Papers* **1999**, *38*, 931.
- [215] M. Hirohata, K. Tada, R. Hidayat, T. Masuda, K. Yoshino, *Japanese Journal of Applied Physics Part 2-Letters* **1997**, *36*, L302.
- [216] C. W. Lee, K. S. Wong, W. Y. Lam, B. Z. Tang, *Chemical Physics Letters* **1999**, *307*, 67.
- [217] L. M. Leung, K. H. Tan, *Macromolecules* **1993**, *26*, 4426.
- [218] F. S. Lu, S. Q. Xiao, Y. L. Li, H. B. Liu, H. M. Li, J. P. Zhuang, Y. Liu, N. Wang, X. R. He, X. F. Li, L. B. Gan, D. B. Zhu, *Macromolecules* **2004**, *37*, 7444.
- [219] T. Masuda, B. Z. Tang, T. Higashimura, *Polymer Journal* **1986**, *18*, 565.
- [220] T. Masuda, Y. Iguchi, B. Z. Tang, T. Higashimura, *Polymer* **1988**, *29*, 2041.
- [221] A. Moliton, R. C. Hiorns, *Polymer International* **2004**, *53*, 1397.

- [222] K. Nagai, L. G. Toy, B. D. Freeman, M. Teraguchi, T. Masuda, I. Pinnau, *Journal of Polymer Science Part B-Polymer Physics* **2000**, *38*, 1474.
- [223] S. Nespurek, V. Cimrova, J. Pflieger, *Colloid and Polymer Science* **1991**, *269*, 556.
- [224] L. Rodriguez-Monge, *Journal of Physical Chemistry B* **1998**, *102*, 4466.
- [225] A. Shukla, *Physical Review B* **2004**, *69*.
- [226] A. Shukla, *Chemical Physics* **2004**, *300*, 177.
- [227] H. Spanggaard, F. C. Krebs, *Solar Energy Materials and Solar Cells* **2004**, *83*, 125.
- [228] R. G. Sun, T. Masuda, T. Kobayashi, *Japanese Journal of Applied Physics Part 2-Letters* **1996**, *35*, L1673.
- [229] R. G. Sun, T. Masuda, T. Kobayashi, *Japanese Journal of Applied Physics Part 2-Letters* **1996**, *35*, L1434.
- [230] R. G. Sun, T. Masuda, T. Kobayashi, *Synthetic Metals* **1997**, *91*, 301.
- [231] R. G. Sun, Q. B. Zheng, X. M. Zhang, T. Masuda, T. Kobayashi, *Japanese Journal of Applied Physics Part 1-Regular Papers Short Notes & Review Papers* **1999**, *38*, 2017.
- [232] R. G. Sun, Y. Z. Wang, D. K. Wang, Q. B. Zheng, A. J. Epstein, *Synthetic Metals* **2000**, *111*, 403.
- [233] K. Tada, R. Hidayat, M. Hirohata, M. Teraguchi, T. Masuda, K. Yoshino, *Japanese Journal of Applied Physics Part 2-Letters* **1996**, *35*, L1138.
- [234] C. H. Ting, C. S. Hsu, *Japanese Journal of Applied Physics Part 1-Regular Papers Short Notes & Review Papers* **2001**, *40*, 5342.
- [235] T. Umeda, T. Tamura, Y. Nishihara, T. Shirakawa, A. Funi, T. Masuda, K. Yoshino, *Japanese Journal of Applied Physics Part 2-Letters* **2002**, *41*, L1499.
- [236] Y. Z. Wang, R. G. Sun, D. K. Wang, T. M. Swager, A. J. Epstein, *Applied Physics Letters* **1999**, *74*, 2593.
- [237] H. Y. Xu, B. Z. Tang, *Journal of Macromolecular Science-Pure and Applied Chemistry* **1999**, *36*, 1197.
- [238] H. Y. Xu, S. Y. Guang, B. Z. Tang, *Chinese Chemical Letters* **2000**, *11*, 21.
- [239] Y. Yoshida, Y. Nishihara, R. Ootake, A. Fujii, M. Ozaki, K. Yoshino, H. K. Kim, N. S. Baek, S. K. Choi, *Journal of Applied Physics* **2001**, *90*, 6061.

- [240] K. Yoshino, T. Akashi, K. Yoshimoto, M. Yoshida, S. Morita, A. A. Zakhidov, *Molecular Crystals and Liquid Crystals Science and Technology Section a- Molecular Crystals and Liquid Crystals* **1994**, 256, 343.
- [241] K. Yoshino, M. Hirohata, R. Hidayat, D. W. Kim, K. Tada, M. Ozaki, M. Teraguchi, T. Masuda, *Synthetic Metals* **1999**, 102, 1159.
- [242] K. Aramata, A. Kajiwara, M. Kamachi, *Macromolecules* **1995**, 28, 4774
- [243] J. W. Youngblood, D. T. Gryko, R. K. Lammi, D. F. Bocian, D. Holten, L. J.S., *J. Org. Chem.* **2002**, 67, 2111.
- [244] S.-C. Chang, G. He, F.-C. Chen, T.-F. Guo, Y. Yang, *Applied Physics Letters* **2001**, 79, 2088.
- [245] S. W. Cha, S.-H. Choi, K. Kim, J.-I. Jin, *Journal of Materials Chemistry* **2003**, 13, 1900
- [246] M. Tabata, W. Yang, K. Yokota, *Polym. J.* **1990**, 22, 1105.
- [247] W. Yang, M. Tabata, S. Kobayashi, K. Yokota, S. Shimizu, *Polym. J.* **1991**, 23, 1135.
- [248] C. G. Densmore, P. G. Rasmussen, *Abstracts of Papers of the American Chemical Society* **2004**, 228, U343.
- [249] R. Nomura, J. Tabei, K. Yamada, T. Masuda, *Kobunshi Ronbunshu* **2002**, 59, 190.
- [250] T. Sone, R. Asako, T. Masuda, M. Tabata, T. Wada, H. Sasabe, *Macromolecules* **2001**, 34, 1586.
- [251] B. Z. Tang, W. H. Poon, S. M. Leung, W. H. Leung, H. Peng, *Macromolecules* **1997**, 30, 2209.
- [252] H. Kaneshiro, S. Hayano, T. Masuda, *Macromolecular Chemistry and Physics* **1999**, 200, 113.
- [253] C. G. Densmore, P. G. Rasmussen, *Macromolecules* **2004**, 37, 5900.
- [254] M. Gouterman, D. Holten, D. Libermann, *Chem. Phys.* **1977**, 25, 139.
- [255] T. Masuda, T. Higashimura, *Adv. Polym. Sci.* **1987**, 81, 121.
- [256] F. Sondheimer, D. A. Ben-Efraim, R. J. Wolovsky, *J. Am. Chem. Soc.* **1961**, 83, 1675.
- [257] S. Janietz, B. Schulz, *European Polymer Journal* **1996**, 32, 465.

- [258] L. M. Dai, *Macromolecular Chemistry and Physics* **1997**, *198*, 1723.
- [259] F. Ishii, S. Matsunami, M. Shibata, T. Kakuchi, *Polymer Journal* **1999**, *31*, 84.
- [260] F. Ishii, S. Matsunami, M. Shibata, T. Kakuchi, *Journal of Polymer Science Part B-Polymer Physics* **1999**, *37*, 1657.
- [261] T. Kakuchi, S. Matsunami, K. Tsuda, F. Ishii, *Polymer Bulletin* **1998**, *40*, 533.
- [262] S. Matsunami, T. Watanabe, H. Kamimura, T. Kakuchi, F. Ishii, K. Tsuda, *Polymer* **1996**, *37*, 4853.
- [263] S. Matsunami, T. Kakuchi, F. Ishii, *Abstracts of Papers of the American Chemical Society* **1997**, *213*, 430.
- [264] M. Tabata, T. Fukushima, Y. Sadahiro, *Macromolecules* **2004**, *37*, 4342.
- [265] X. H. Zhang, Z. Y. Xie, F. P. Wu, L. L. Zhou, O. Y. Wong, C. S. Lee, H. L. Kwong, S. T. Lee, S. K. Wu, *Chemical Physics Letters* **2003**, *382*, 561.
- [266] Y. Sakakibara, *Kino Zairyo* **2001**, *21*, 40.
- [267] R. C. Kwong, S. Sibley, T. Dubovoy, M. Baldo, S. R. Forrest, M. E. Thompson, *Chemistry of Materials* **1999**, *11*, 3709.
- [268] V. Cleave, N. Tessler, G. Yahiolglu, P. Le Barny, H. Facchetti, N. Boucton, R. H. Friend, *Synthetic Metals* **1999**, *102*, 939.
- [269] D. Gryko, J. Li, J. R. Diers, K. M. Roth, D. F. Bocian, W. G. Kuhr, J. S. Lindsey, *J. Mater. Chem.* **2001**, *11*, 1162.
- [270] W. Siebrand, *J. Chem. Phys.* **1967**, *46*, 440.
- [271] E. G. Azenha, A. C. Serra, M. Pineiro, M. M. Pereira, J. S. de Melo, L. G. Arnaut, S. J. Formosinho, A. M. D. R. Gonsalves, *Chemical Physics* **2002**, *280*, 177.
- [272] V. V. Smirnov, E. K. Woller, D. Tatman, S. G. DiMugno, *Inorganic Chemistry* **2001**, *40*, 2614.
- [273] G. A. Spyroulias, A. P. Despotopoulos, C. P. Raptopoulou, A. Terzis, D. de Montauzon, R. Poilblanc, A. G. Coutsolelos, *Inorganic Chemistry* **2002**, *41*, 2648.
- [274] H. J. Callot, A. Giraudeau, M. Gross, *Journal of the Chemical Society, Perkin Transactions 2: Physical Organic Chemistry* **1975**, *12*, 1321.
- [275] D. A. Hartree, *Proc. Camb. Phil. Soc* **1928**, *24*.
- [276] G. Racah, *Phys. Rev.* **1942**, *62*, 438.

- [277] G. Racah, *Phys. Rev.* **1943**, *63*, 387.
- [278] P. O. Löwdin, *Tech. Note 12, Uppsala* **1958**.
- [279] M. Tinkham, *Group Theory and Quantum Mechanics*, McGraw-Hill, New York, **1964**.
- [280] J. S. Griffith, *Theory of Transition Metal Ions*, Cambridge University Press, New York, **1961**.
- [281] M. E. Rose, *Angular Momentum*, John Wiley and Sons, Inc., New York, **1957**.
- [282] I. B. Bersüker, *Electronic Structure and Properties of Transition Metal Compounds*, John Wiley and Sons, Inc., New York, **1996**.
- [283] R. L. Liboff, *Quantum Mechanics*, 3rd. Edition ed., Addison Wesley, New York, **1998**.
- [284] B. N. Figgis, M. A. Hitchman, *Ligand Field Theory and Its Applications*, Wiley-VCH, New York, **2000**.
- [285] Y. Miao, Y. Lian-xiang, J. Wen-ping, Y. Wen-sheng, L. Guo-fa, *Chemical Research in Chinese Universities* **2004**, *20*, 807.
- [286] F. A. Cotton, *Chemical Applications of Group Theory*, 2nd. ed., Wiley-Interscience, 1971, **1971**.
- [287] M. Born, J. R. Oppenheimer, *Ann. Phys.* **1927**, *84*, 457.
- [288] R. J. Borg, G. J. Dienes, *Physical Chemistry of Solids*, Academic Press, New York, **1992**.
- [289] A. Einstein, *Ann. Phys.* **1905**, *17*, 132.
- [290] A. Einstein, *Ann. Phys.* **1906**, *20*, 199.
- [291] A. Einstein, *Physikalische Zeitschrift* **1917**, *18*, 121.
- [292] A. P. Thorne, *Spectrophysics*, Chapman and Hall, New York, **1988**.

BIOGRAPHICAL SKETCH

Garry Brian Cunningham was born December 20, 1972, in New Castle, Pennsylvania. After graduation from high school, he underwent a four year stint in the U.S. Army as a fire direction control specialist. He then attended Lock Haven University, where he planned on getting a degree in pharmacy. It was then, during all of the prerequisite science classes, that he decided pharmacy was not for him. He realized his passion was in chemistry and subsequently changed his major. He graduated in 1999, with his B.S. in chemistry. After receiving his bachelor's degree, Garry continued his studies at Washington State University (WSU). After some unforeseen and unfortunate events, he decided to leave WSU with his M.S. degree in physical inorganic chemistry. He then moved on to the University of Florida, where he pursued a Ph.D. degree in inorganic chemistry in 2002. Upon graduation, Garry will be moving to North Carolina to work at International Technology Center (ITC), where he will be a research associate. Beyond then, the future has not been written.